Title
Experiments to Improve Nuclear Data for High Energy Density Environments

Author
Champine, Brian Champine

Publication Date
2016

Peer reviewed|Thesis/dissertation

Experiments to Improve Nuclear Data for High Energy Density Environments

By

Brian Champine

A dissertation submitted in partial satisfaction of the

requirements for the degree of

Doctor of Philosophy

in

Engineering - Nuclear Engineering

in the

Graduate Division

of the

University of California, Berkeley

Committee in charge:

Professor Eric B. Norman, Chair
Doctor Nicholas D. Scielzo
Professor Kai Vetter
Professor Paul Renne

Spring 2016

Experiments to Improve Nuclear Data for High Energy Density Environments

Abstract

Experiments to Improve Nuclear Data for High Energy Density Environments

by

Brian Champine

Doctor of Philosophy in Engineering - Nuclear Engineering

University of California, Berkeley

Professor Eric B. Norman, Chair

The work presented in this dissertation used a variety of facilities and methods to make precise measurements of neutron reaction cross sections and γ-ray branching ratios important for the study of high energy density environments. While measurements related to thulium used commercially available detectors, others required the development of a new detection system. A 4π gas proportional beta counter was designed and characterized specifically for the measurement of fission product branching ratios. Measurements of increasing precision were performed for ^{147}Nd and ^{95}Zr. The instrumentation and techniques developed in this dissertation have set the path for an ongoing series of fission product branching ratio measurements. With work towards refinements mentioned here, precision will continue to improve in the measurements and results of future studies with these devices.

To my father, who has always believed in me more than I believed in myself.

Contents

List of Figures

List of Tables

Acknowledgments

My wife, Bernadette, stood by me and supported me through my academic struggles and personal crises. I can not thank her enough for her understanding and patience with me, but now I have an excuse when I can't find my keys! My children, Sasha and Max, have been an inspiration to me and give me great joy.

Kai Vetter for brought me into the department, mentored me while I was in his research group, and continued to do so chairing my qualifying exam and as a member of my dissertation committee. I thank Rick Norman for taking me on as a student and providing a great deal of wisdom along my journey. He is one of the best teachers I've ever had. Keenan Thomas taught me many practical aspects of data analysis and was frequently available for many enjoyable discussions, both on- and off-topic. Thanks also go to Paul Renne for serving on my qualifying exam and dissertation committees.

A number of scientists at Lawrence Livermore National Laboratory were essential to the completion of this work. Nick Scielzo has been an incredible mentor and role model. Anton Tonchev worked closely with me, and I could count on him to point out details that I would have otherwise overlooked. Kay Kolos was a great ally, friend, and coach. Jason Burke provided unsolicited advice that was always on point. Collectively, they have given me tremendous insight in how science is correctly done.

I am grateful to the U.S. Army for providing me time and financial support to complete my studies under the Long Term Health Education and Training (LTHET) program. Portions of this work were performed under the auspices of the US Department of Energy by Lawrence Berkeley National Laboratory under Contract No. DE-AC02- 05CH11231, Lawrence Livermore National Laboratory under Contract No. DE-AC52-07NA27344, with funding support from the Laboratory Directed Research and Development Program under project 15-ERD-015, and the University of California under Contract No. DE-AC0376SF0098. I also thank the US Department of Energy's NNSA, Office of Nonproliferation Research and Development (NA-22), for financial support. This material is based upon work supported by the Department of Energy National Nuclear Security Administration under Grant No. DE-NA-0000979 through the Nuclear Science and Security Consortium. Finally, this work was supported by the US Department of Energy, Grant No. DE-FG-97ER40133, and by the National Nuclear Security Administration under Grant No. DA-NA-0001839, both to Duke University.

Chapter 1

Introduction

Under certain conditions of extreme temperature and pressure, nuclear reactions can occur at very high rates, releasing large amounts of energy. In these high energy density environments, the study of the physical conditions and dynamics presents special challenges. The time scales are often very short and severe conditions can be damaging to instruments, making direct measurements impossible. Collected material that was formed in these high energy density environments can be studied in more stable laboratory conditions. This may include radioactive products of the fission or fusion reactions or tracer material that is intentionally placed in or near the environment. These isotopes can be quantified by measuring the radiation that they emit when they decay. These measurements rely on knowledge of the probabilities of interactions during formation and the decay characteristics of the radioisotopes. The work presented here was conducted to address the nuclear data needs of neutron induced reaction cross sections and γ-ray branching ratios of specific isotopes used to study these high energy density environments.

1.1 Fission and Fusion

Nuclear energy is released when the binding energy per nucleon of the products is greater than that of the reactants. Fission is a process in which a heavy nucleus separates into two or more nuclei, often accompanied by several neutrons. Because the product nuclei are shifted significantly to the left on the curve shown in Fig. 1.1, a large amount of energy is released as compared to radioactive decay such as α, β, or electron capture (ε). This process occurs spontaneously in select isotopes, such as ^{250}Cm and ^{252}Cf, with half-lives on the order of years. Other isotopes, such as ^{235}U and ^{239}Pu, exhibit very little spontaneous fission, but the introduction of a neutron into these nuclei can induce fission with a cross-section on the order of barns. Because the fission process creates additional neutrons capable of inducing further fissions, chain reactions of neutron-induced fission occur when the fissile material is sufficiently concentrated. In nuclear reactors used for energy or research, the core is composed of fissile fuel in combination with other material that slows down and absorbs neutrons which is arranged in such a way that the rate can be controlled and maintained for

extended periods of time. With higher fuel density, as in a nuclear device, neutrons from one fission can induce multiple fissions in surrounding material with an average time between generations of neutrons on the order of 10 ns. This causes a rapid increase in fission rate, and a nuclear device can create an environment with a power density on the order of 10^{22} $\frac{W}{m^3}$ in less than a microsecond [12].

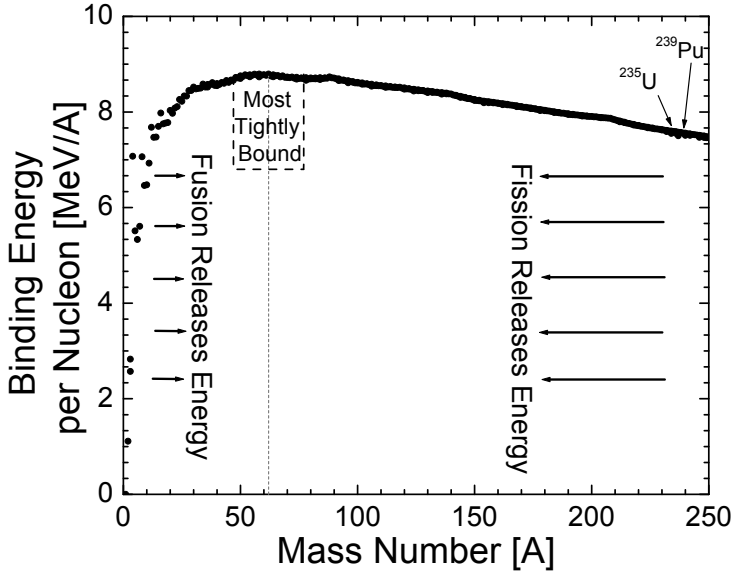

Figure 1.1: Binding energy per nucleon for stable nuclei up to A=209 and long-lived nuclei from A=210-250. [1].

Fusion is a process in which light nuclei combine into one nucleus. Because the binding energy per nucleon of the lightest nuclei, such as ^{1}H, ^{2}H, and ^{3}H, is so much smaller than heavier nuclei, as shown on the curve shown in Fig. 1.1, large amounts of energy are released with each fusion reaction. In order for fusion to occur, the two light nuclei must overcome the Coulomb barrier created by the mutual repulsion due to the positive charge of their protons. The sun is composed primarily of hydrogen and helium at high temperature and pressure, sufficient for fusion to take place. The core of the sun is at a temperature of about 15×10^6 K, and a density of 125 $\frac{g}{cm^3}$. Given a reaction rate of 10^{38} $\frac{fusion}{s}$, the energy density at the center of the sun is estimated to be 275 $\frac{W}{m^3}$.

One method to create the plasma conditions necessary for a fusion reaction uses the energy from a fission trigger. Fission neutrons interact with solid ^{6}Li^{2}H fuel by the reaction ^{6}Li(n,n+^{3}H)^{4}He, providing tritium to fuse with deuterium. The fusion of compressed D-T fuel has an energy production rate comparable to fission weapons, 10^{22} $\frac{W}{m^3}$, and can last for a few microseconds [12]. In the laboratory, two main approaches have been employed for controlled fusion reactors. One approach relies on strong magnetic fields to cause charged

particles in the high temperature plasma to spiral and perpetuate contained steady state fusion. Research has been underway since the 1950's, but maintaining sufficient ion density and containment time has proved to be a formidable challenge. The most prominent experimental magnetic fusion power reactor, ITER, is under construction with a goal of achieving the first plasma in 2025 [13]. The second approach uses inertial confinement. Small capsules are heated with intense laser pulses, causing them to implode. As the capsule implodes, deuterium and tritium fuel is compressed to create density and temperature conditions sufficient for fusion. The National Ignition Facility (NIF) at Lawrence Livermore National Laboratory (LLNL) focuses 192 lasers with a total power of up to 5 x 10^{14} W onto a hohlraum which converts light into x-rays that strike the fuel capsule. NIF performed its first integrated ignition experiments in 2010, and has steadily increased fusion yields. Recent experiments reached temperatures of 40×10^6 K and densities of 500 $\frac{g}{cm^3}$ in a volume of 10^{-7} cm^3 [14, 15]. A single shot yields up to 10^{15} fusion reactions over a time period of 100 ps [16]. This results in an energy density of 10^{14} $\frac{W}{m^3}$.

1.2 Nuclear Data Needs for Fusion Study at the National Ignition Facility

NIF is used to advance the scientific study of high energy density environments needed to create fusion. The NIF project began with the Laser Inertial Fusion Energy (LIFE) program, with a focus towards developing viable nuclear energy production [17]. Although achieving a fusion output power greater than the laser energy input is still a goal, the program was ended and objectives were realigned to better understanding the inertial confinement process and supporting basic and applied science research. In compliance with the Comprehensive Nuclear-Test-Ban Treaty, the United States has not conducted a nuclear device test since 1992 [18]. With a goal of stockpile stewardship, research at NIF continues to study the phenomena that occur in fusion environments containing plutonium without detonating a nuclear device. In the field of astrophysics, projects are underway to investigate processes such as turbulence in supernova explosions by Raleigh-Taylor instability [19] and to study mineral behavior of so-called "super-Earth" planets with similar volume, but up to 10 times greater in mass. Use of shock waves from NIF capsule implosions to gain understanding of mineral behavior at very high temperatures and pressures which are not possible with other experimental techniques can feed data into models that are essential to the understanding of the planets' thermal behavior, long term evolution, and interior structure [20].

1.2.1 NIF Diagnostics

A large number of diagnostics are used to interpret the complex dynamics for each NIF shot. A Diagnostic Instrument Manipulator (DIM) holding four metal foils placed near the NIF capsule for purposes of neutron activation analysis is shown in Fig. 1.2. During the shot, a suite of x-ray instruments and laser measurement devices are used to characterize the

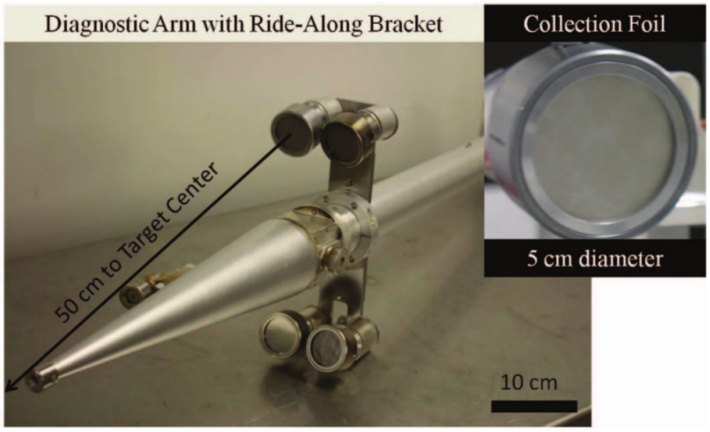

Figure 1.2: Diagnostic Instrument Manipulator (DIM) used to hold metal foils near the NIF capsule. The material is later analyzed offline using neutron activation analysis .[2]

uniformity and time synchronization of the hohlram heating [21, 22], and neutron imaging is used to determine the spot size and distribution of primary and secondary neutrons [23]. Several hours after the completion of the shot, gases and solid debris remnants from the hohlram are collected and examined using γ-spectroscopy and scanning electron microscopy.

1.2.2 Reaction in Flight Neutron Measurements

Some of the work performed in this dissertation was motivated by the nuclear data needs associated with the study of Reaction-in-Flight (RIF) neutrons [24]. As a result of D-T fusion, neutrons are produced via the ^{3}H(d,n)^{4}He reaction with energies E$_n$=14.1 MeV. Higher-energy neutrons can be created when a deuterium or tritium ion brings kinetic energy gained from elastic scattering with a fusion product in the plasma to the D-T reaction, as illustrated in Fig. 1.3. This multi-step process produces so-called RIF neutrons with energies up to 30 MeV. These up-scattered deuterium and tritium ions, known as knock-on ions, lose energy as they trasverse the plasma before initiating a tertiary fusion reactions. The energy loss during this transit directly affects the quantity and energy spectrum of the RIF neutrons.

Although the RIF neutrons represent less than 0.3% of the total neutron fluence, their spectrum carries important information about the fusion burn and charged-particle stopping powers in a warm, dense plasma [25, 26, 27]. The facilities at NIF have enabled experiments to explore the stopping power of the plasma conditions in a region that no other facility has been able to provide.

A simulated NIF neutron-energy spectrum [27] from D-T fusion is shown in Fig. 1.4. Because the pulse of neutrons is very intense, neutron time-of-flight measurements can be used to measure the energy spectrum of the primary 14-MeV peak, but background obscures the lower-intensity RIF neutrons [28, 29]. A neutron activation technique was selected to quantify the ratio between the 14-MeV neutrons formed by the primary D-T reaction and

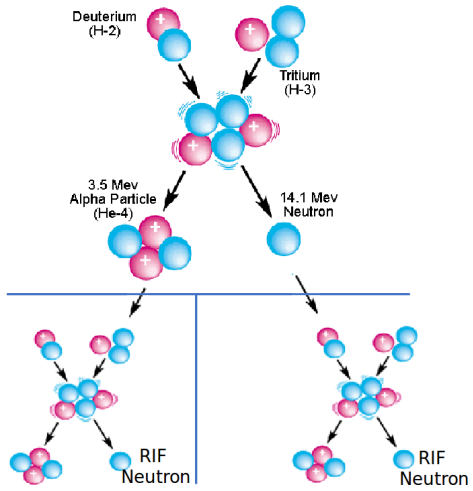

Figure 1.3: Reaction-in-Flight production mechanisms. Starting at the top, D-T fusion creates an α particle and an energetic neutron. The bottom left represents the transfer of energy from the α particle to a ^{3}H ion, which then carries more energy into a subsequent D-T reaction. The bottom right represents another possible process in which the neutron transfers energy to a ^{2}H ion. In either case, the ^{2}H or ^{3}H brings kinetic energy into the fusion reaction and can give rise to neutrons with energies up to 30 MeV.

the higher-energy RIF neutrons. The 15-MeV threshold for the ^{169}Tm(n,3n)^{167}Tm reaction makes thulium a useful diagnostic for measurement of the RIF neutrons in the presence of copious 14-MeV neutrons. ^{167}Tm also has convenient production and decay characteristics: a large (n,3n) cross section, a convenient half-life ($t_{1/2}$ = 9.2 days), and an intense γ-ray transition (with energy E_γ = 207.8 keV and γ-ray emission branching ratio I_γ = 42$\pm$8%) allow for the sample to be counted offline after the material has been retrieved following the shot. Since ^{168}Tm is also produced from stable ^{169}Tm through the (n,2n) reaction by 14.1-MeV neutrons, the ratio of ^{167}Tm to ^{168}Tm produced in a thulium monitor foil can provide a measure of the RIF neutron yield. The activation of foils at NIF and the subsequent offline counting using a Compton-suppressed high-purity germanium (HPGe) clover system to suppress backgrounds from the decay of ^{168}Tm has been successfully used to measure ^{167}Tm production and therefore determine the yield of RIF neutrons [27]. There are several stopping power models for plasmas which agree with each other at low density but begin to diverge when applied to higher density plasmas produced by NIF. The results of these tests were able to rule out the applicability of some of these models, but so far have not been sufficient to differentiate others, in part due to the uncertainties in the ^{169}Tm(n,3n)^{167}Tm cross section and the γ-ray branching ratio following electron capture decay of ^{167}Tm [27]. The following two chapters describe my work to improve the precision of the nuclear data available for thulium.

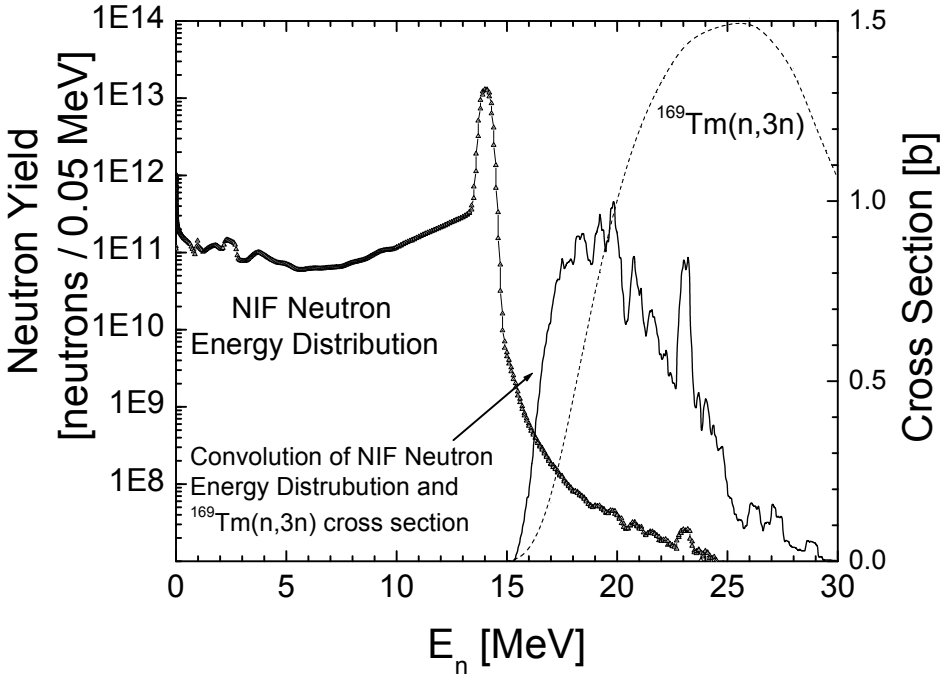

Figure 1.4: Overlay of simulated NIF neutron energy distribution (log scale y-axis on left side) and ^{169}Tm(n,3n)^{167}Tm cross section (linear scale y-axis on right side). Note the apparent structure above 15 MeV is due to statistics. Only reaction-in-flight neutrons have enough energy to produce ^{167}Tm.

1.3 Nuclear Data Needs for Fission Product Yields

As a nucleus splits during the fission process, two lighter nuclei are formed. Spontaneous and thermal neutron induced fission typically produces one heavier and one lighter fission product, with an asymmetrical mass distribution as shown in Fig. 1.5. This asymmetry is due to nuclear shell closures at Z=50 and N=82 near the heavy mass fragment peak. In the study of nuclear devices, the total number of fissions that occur during an explosion can be inferred by measuring the quantity of fission products. Fission products are most commonly neutron rich because the smaller nuclei require fewer neutrons to produce short-range strong force to overcome the electrostatic repulsion of the protons. These neutron-rich nuclei decay through β emission often accompanied by γ-rays. Samples of debris can be collected for γ-ray spectroscopy to quantify the radioisotopes present.

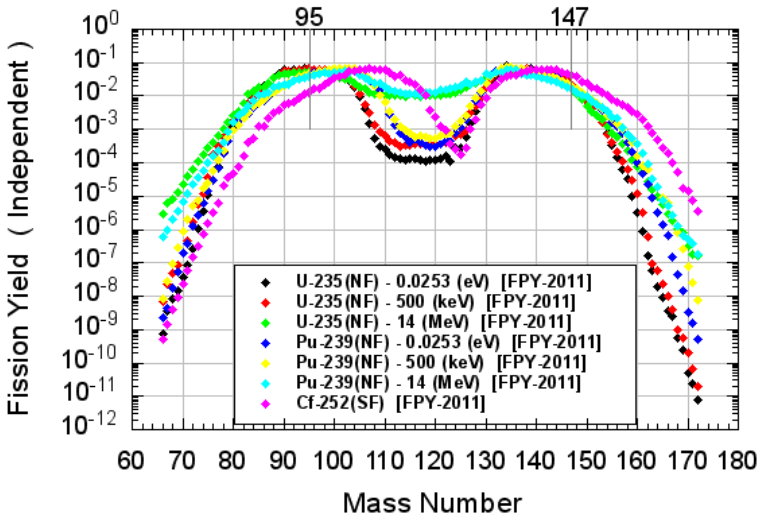

Figure 1.5: Independent yields for neutron induced fission of ^{235}U and ^{239}Pu and spontaneous fission of ^{252}Cf [3].

The shape of the fission product yield curve is dependent on the initial energy of the system, with the asymmetry decreasing as energy increases. During a nuclear detonation, fissions are induced by a distribution of neutron energies that may not be well characterized, so it is desirable to select a product whose yield is relatively independent from the energy of the neutron which induced the fission. One isotope that has been extensively used for yield determinations is ^{147}Nd [30]. ^{147}Nd has a half-life of 10.9 days and is easily characterized through measurement of the 531-keV γ-ray emitted following β emission. Nuclear data sheets reports the branching ratio for this line to be 0.1337(11) [9]. This 8% relative uncertainty limits the precision that yields can be determined for the A=147 mass chain. Chapter

4 describes the development of a 4π β proportional counter developed for measurements of fission product branching ratios. Chapter 5 describes measurements of ^{95}Zr, whose branching ratio is well known, in order to validate the techniques used. It continues with measurements of ^{147}Nd to improve the precision of the branching ratio data and sets the stage for future measurements of other fission product isotopes.

Chapter 2

^{167}Tm Branching Ratio Measurement

The level scheme for ^{167}Er was determined by Funke *et al.* [31] in 1968 using γ-γ coincidence techniques with sodium iodide scintillator and lithium drifted germanium detectors following electron capture (EC) decay of ^{167}Tm and β decay of ^{167}Ho. This work has remained as the sole reference for the relative intensities in the Nuclear Data Sheets (NDS) [4] at the time of the present work. Since the transition directly to the ground state is 2^{nd} forbidden, unique and other transitions are 1^{st} forbidden, non-unique, the NDS evaluator assumed that transitions directly to ground could be neglected and calculated the absolute branching ratio using the published relative intensities of γ-ray lines and internal conversion coefficients. Based on these works, the branching ratio was widely reported as 42$\pm$8% [5], a relative uncertainty of 19%.

This chapter describes an experiment that was designed to measure the branching ratio to greater precision [24]. First, a relatively pure source of ^{167}Tm was created. A 32-μm-thick ^{165}Ho foil was irradiated using an α-particle beam at the 88-Inch Cyclotron at LBNL to induce the ^{165}Ho(α,2n)^{167}Tm reaction. Then, the sample was measured using HPGe detectors. Total activity was determined by measuring x-rays following EC decay, and the γ rays of interest were measured directly.

2.1 Experiment

2.1.1 Preparation of the Sample

A thin foil was desired for this experiment. First, the α particles would lose energy as they pass through the foil, resulting in differing levels of isotope production with depth. Use of a sufficiently thin foil allows for approximating the isotope distribution as uniform. Second, the offline measurement requires corrections for self attenuation of x rays and γ rays produced within the foil. Thinner foil reduces the size of the corrections and therefore the uncertainty introduced in the results due to these factors. Holmium foil with a purity of 99.9% was purchased with a nominal thickness of 25 μm. Foil thickness was determined using three methods: direct measurement by calipers, calculation from the area and mass,

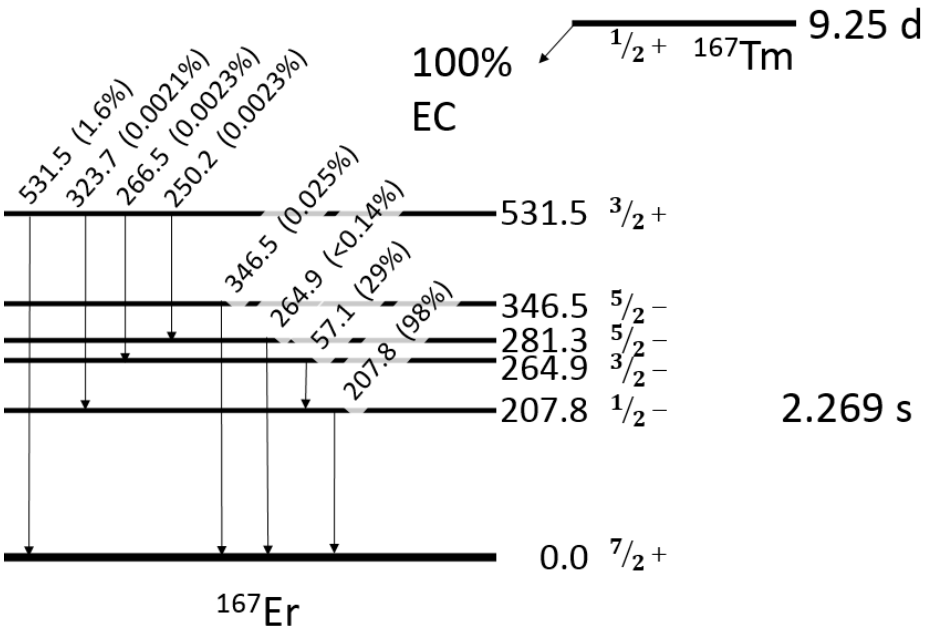

Figure 2.1: Relevant decay scheme properties for the electron-capture decay of ^{167}Tm. All energies are given in keV [4].

and attenuation measurements using the 59-keV γ rays from an ^{241}Am source.

The experimental database for measurements of ^{165}Ho(α,Xn) cross sections was referenced to determine the optimal α-particle beam energy for the production of ^{167}Tm (Fig. 2.2). In addition to ^{167}Tm ($t_{1/2}$=9.25 d), ^{168}Tm ($t_{1/2}$=93.1 d) and ^{166}Tm ($t_{1/2}$=7.70 h) isotopes were produced by the ^{165}Ho(α,n) and ^{165}Ho(α,3n) reactions, respectively. Use of an α-particle beam with energy at the peak cross section would result in a non-trivial amount of ^{168}Tm. With its shorter half life, the ^{166}Tm produced by higher-energy beams could be allowed to decay to stable ^{166}Er prior to measurement. Therefore, the optimal energy for ^{167}Tm production was a trade-off between efficiency and source purity. An α-beam energy of 29 MeV was selected so that the ^{168}Tm production would be manageable and the ^{167}Tm cross section was near its peak value. This resulted in an induced activity of ^{168}Tm that was initially less than 0.5% of that of the desired ^{167}Tm.

2.1.2 Measurements with High Purity Germanium Detectors

Both a coaxial and planar germanium detectors were used in this experiment to measure the foil. Efficiencies for each detector were determined using ^{57}Co, ^{133}Ba, ^{137}Cs, ^{152}Eu, and ^{241}Am calibration sources measured at a distance of 25 cm to minimize geometry uncertainties and avoid true-coincidence summing. The γ-ray lines used in these calculations are

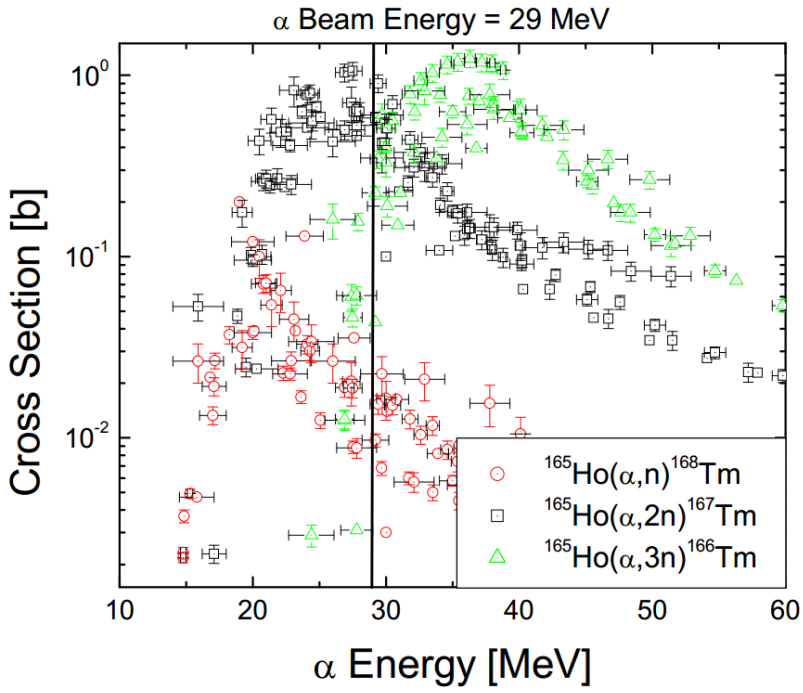

Figure 2.2: Holmium (α,Xn) cross sections from EXFOR database [5]. At the beam energy of 29 MeV, the (α,2n) cross section was $\sim$0.5 b, while the (α,3n) cross section was $\sim$0.02 b.

summarized in Table 2.1. The photopeak detection efficiency was calculated by using

$$\varepsilon_\gamma = \frac{C_\gamma}{A_0 e^{-\lambda t_1} I_\gamma t_2} \,, \tag{2.1}$$

where C_γ is the net counts in the γ peak, A_o is the activity of the calibration source at the time of its original calibration, λ is the radioactive decay constant, t_1 is the time elapsed between the source calibration date and the measurement, I_γ is the branching ratio for the peak of interest, and t_2 is the length of measurement.

In order to fit the efficiency data obtained from measuring the calibration sources, the functional form [32]

$$\epsilon_i = \sum_{j=1}^{6} a_j (\ln E_i)^{j-1} \,, \tag{2.2}$$

was used, where ϵ_i is the photopeak efficiency, a_j are the fitting parameters, and E_i is the energy of γ-ray line. The measured efficiencies and the best fit curves for each detector are plotted in 2.3.

The x rays and γ rays from the activated foil were counted using both coaxial and planar HPGe detectors. The foil counting was performed at the distance where the efficiency calibrations were performed, 25 cm from the face of the detectors. The finer resolution of the planar HPGe detector in the lower-energy region was preferable for measuring the x rays. A sample spectrum measured with the planar HPGe detector is shown in Fig. 2.4. Self attenuation of the emitted x rays and γ rays in the foil was calculated using the foil thickness and photon cross sections [33] according to the equation [34],

$$a = \frac{\left(1 - e^{-\mu X}\right)}{\mu X} \,, \tag{2.3}$$

where a is the self-attenuation correction factor, μ is the attenuation coefficient, and X is the foil thickness. These corrections were less than 6% for the x rays, and were much smaller for the higher-energy γ rays.

2.1.3 Data Analysis

The 49.128-keV $K_{\alpha 1}$ x ray emitted from ^{167}Er following ^{167}Tm EC was used to determine the activity of ^{167}Tm in the sample. The γ-ray branching ratios, I_γ, were then determined from

$$I_\gamma = \frac{\epsilon_x a_x}{\epsilon_\gamma a_\gamma} \frac{N_\gamma P_{K_{\alpha 1}}}{N_x} \,, \tag{2.4}$$

where ϵ is the photopeak efficiency, a is the self-attenuation factor, and N is the number of counts in the peak of interest for the measured x rays and γ rays denoted by the subscripts x and γ, respectively, after correcting for x-ray contributions from the decay of ^{168}Tm as

Table 2.1: Gamma lines used in HPGe photopeak efficiency determination [5]. All sources were Eckert and Ziegler Type M standards removed from their aluminum holders.

Nuclide	E_γ [keV]	I_γ
^{241}Am	26.34	0.024(2)
^{133}Ba	30.85	0.994(26)
^{137}Cs	32.06	0.0580(13)
^{152}Eu	39.52	0.210(5)
^{152}Eu	40.11	0.377(8)
^{133}Ba	53.16	0.02199(22)
^{241}Am	59.54	0.359(4)
^{207}Bi	72.80	0.213(6)
^{207}Bi	74.95	0.358(10)
^{207}Bi	84.77	0.1245(33)
^{57}Co	122.06	0.8560(17)
^{57}Co	136.47	0.1068(8)
^{133}Ba	160.61	0.006380(5)
^{133}Ba	223.23	0.00453(3)
^{152}Eu	244.69	0.0755(4)
^{133}Ba	276.39	0.07164(22)
^{133}Ba	302.85	0.1833(6)
^{152}Eu	344.27	0.2659(20)
^{133}Ba	356.01	0.6205(19)
^{152}Eu	367.78	0.00859(6)
^{133}Ba	383.85	0.0894(3)
^{152}Eu	411.11	0.02237(13)
^{152}Eu	443.96	0.03170(25)
^{207}Bi	569.70	0.9774(3)
^{137}Cs	661.65	0.851(2)

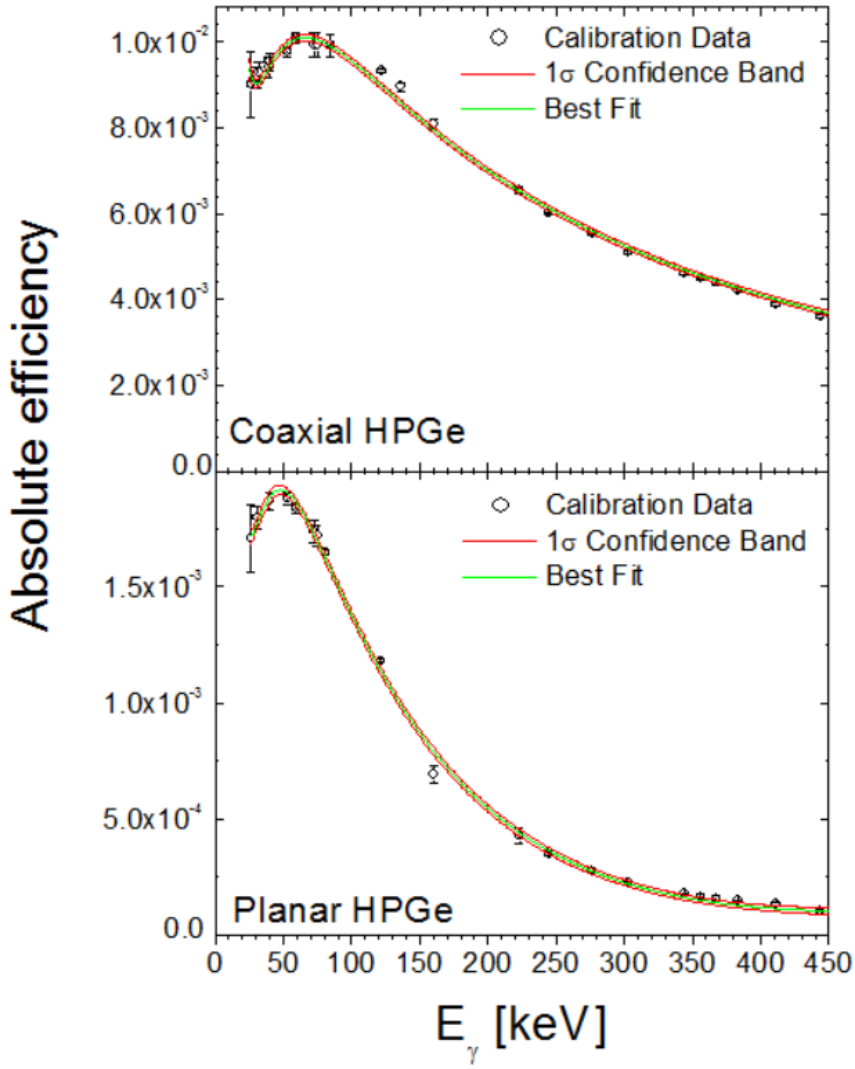

Figure 2.3: Comparison of detection efficiency for the coaxial and planar germanium detectors used in the branching ratio experiment.

Table 2.2: Probability of K-shell electron capture for EC decay of ^{167}Tm.

E(level) [keV]	I_{EC}[4]	$P_{k_{EC}}$[35]
531.5	1.64(23)	0.7664(21)
346.5	0.025(5)	0.8015(18)
264.9	29(7)	0.8080(17)
207.8	69(18)	0.8113(17)
Weighted Average		0.8096(31)

described below. $P_{K_{\alpha 1}}$ is the probability of $K_{\alpha 1}$ x-ray emission following the EC decay. The K_β x rays were not used here due to the interference with the 57.1-keV γ ray following ^{167}Tm decay.

The value of $P_{K_{\alpha 1}}$ was calculated from the product of the total number of K-shell vacancies per decay and the probability of that vacancy resulting in the emission of a $K_{\alpha 1}$ x ray. The K-shell vacancies may be caused by the EC transition as well as any subsequent internally-converted transitions as ^{167}Er de-excites to the ground state.

During EC decay, an inner orbital atomic electron interacts with a proton in the nucleus, forming a neutron and ejecting a neutrino. The most likely electrons to participate in this process are those from the K-shell, but the probability is dependent on the atomic number of the parent nucleus, Z, the energy of the decay, Q_{EC}, the level energy of the excited daughter nucleus, E(level), and spin and parity of the initial and final states. The interactive program called EC-CAPTURE, as described in Ref. [35], was used to calculate the probability and associated uncertainty of K-shell electron capture for each of the energy levels shown in Table 2.2.

To obtain the overall probability of K-shell electron capture, $P_{K_{EC}}$, in this decay, a weighted average was calculated using

$$P_{K_{EC}} = \frac{\sum_i I_{EC_i} P_{K_{EC_i}}}{\sum_i I_{EC_i}} \,, \tag{2.5}$$

where I_{EC_i} is the intensity of the EC decay to each E(level) per 100 decays and $P_{K_{EC_i}}$ is the probability of K-shell electron capture associated with that level. This resulted in $P_{K_{EC}}$=0.8096 $\pm$ 0.0031.

Following EC decay to excited states of ^{167}Er, the nucleus may de-excite by either γ-ray emission or internal conversion, a process in which nuclear energy is transferred to an atomic electron. In the internal conversion process, this causes the electron to be ejected from the atom, leaving a vacancy. In order to determine the probability of K-shell vacancies from this, data for internal conversion coefficients, α, and the following relationships were used

[36]:

$$\lambda_t = \lambda_\gamma + \lambda_e \ , \tag{2.6}$$

$$\alpha = \frac{\lambda_e}{\lambda_\gamma} \ , and \tag{2.7}$$

$$\alpha = \alpha_K + \alpha_L + \alpha_M + \cdots \ , \tag{2.8}$$

where λ_t is the decay probability for a particular nuclear level, λ_e is the decay probability for internal conversion, λ_γ is the decay probability for γ-ray emission, and α_X, are the partial internal coefficients corresponding to electrons ejected from a particular shell.

For each excited state of the ^{167}Er nucleus, the probability of forming a K-shell vacancy is then given by

$$P_K = \left(\frac{\alpha_K}{\alpha}\right) \frac{\alpha}{\alpha+1} = \frac{\alpha_K}{\alpha+1} \ . \tag{2.9}$$

Calculating the effect of internal conversion also requires some knowledge of the branching ratio for each excited state transition, but the uncertainty in the existing branching ratios have only a small effect on this calculations. For excited states transitioning directly to ground, the number of K-shell vacancies can be determined by multiplying the γ-ray branching ratio by α_K. Specifically for the 208-keV state, the large uncertainty in the branching ratio can be minimized with the understanding that all transitions to ground go through this state, with the exception of transitions directly to ground as mentioned previously. The 57-keV transition between the 265-keV level and the 208-keV level is below the threshold for K-shell conversion in Er (the K-shell binding energy is 57.5 keV), and therefore can not create K-shell vacancies. Other transitions to levels other than the ground state are less than one part in ten thousand per decay based on existing decay scheme information. Only the 265-, 346-, and 531-keV transitions bypass the 208-keV state. The probability of K-shell vacancy due to internal conversion was then calculated using

$$\begin{aligned} P_{K_{IC}} = \frac{\alpha_{K_{208}}}{1+\alpha_{208}} \left[1 - I_{\gamma_{531}}(1+\alpha_{531}) - I_{\gamma_{346}}(1+\alpha_{346}) - I_{\gamma_{265}}(1+\alpha_{265})\right] \\ + I_{\gamma_{531}}\alpha_{K_{531}} + I_{\gamma_{346}}\alpha_{K_{346}} + I_{\gamma_{265}}\alpha_{K_{265}} \ , \end{aligned} \tag{2.10}$$

resulting in a value of $P_{K_{IC}}$=0.1970 $\pm$ 0.0034.

This probability of creating a K-shell vacancy was then multiplied by the probability of $K_{\alpha 1}$ x-ray emission, which is 47.5(10) per 100 K-shell vacancies from Table 7A of Ref. [38]. A value of $P_{K_{\alpha 1}}$=0.478(10) was obtained, with an uncertainty dominated by the uncertainty in the $K_{\alpha 1}$ x-ray intensity per K-shell vacancy.

The correction for the number of x rays emitted from the EC decay of the longer-lived ^{168}Tm was calculated in a similar manner, with the activity determined from the measured 184-keV and 198-keV γ-ray peaks associated with this decay, as the γ-ray branching ratios

Table 2.3: Internal conversion coefficients for Er.

E(level) [keV]	α[37]	α_K[37]
531.5	0.01407(20)	0.0128(2)
346.5	0.01304(19)	0.01102(16)
264.9	0.833(20)	0.664(10)
207.8	1.38(2)	0.476(7)

are precisely known. This correction was only 0.4% (with negligible uncertainty) because of the small amount of ^{168}Tm activity in the sample.

2.2 Results and Discussion

The results and uncertainties are summarized in Table 2.4. The 207.8-keV and 531.5-keV γ-ray branching ratios were measured to be 0.419(16) and 0.0173(7), respectively. The branching ratios were determined with a relative uncertainty of about 3.8%, which is a factor of five better than the previous measurement [4], and the first time that the γ-ray branching ratios were directly measured for ^{167}Tm decay.

As noted in Refs. [4] and [39], the branching ratio of the 207.8-keV transition can also be calculated by decay-scheme normalization, if it is assumed that the second-forbidden EC transition to the ground state is negligible. In this case, after correcting for the internal-conversion contribution to each observed γ ray, the sum of the intensities of all the transitions to the ground state must equal 100%. This calculation produces a branching ratio of 0.416(7) [4], which agrees well with our experimental determination of the branching ratio.

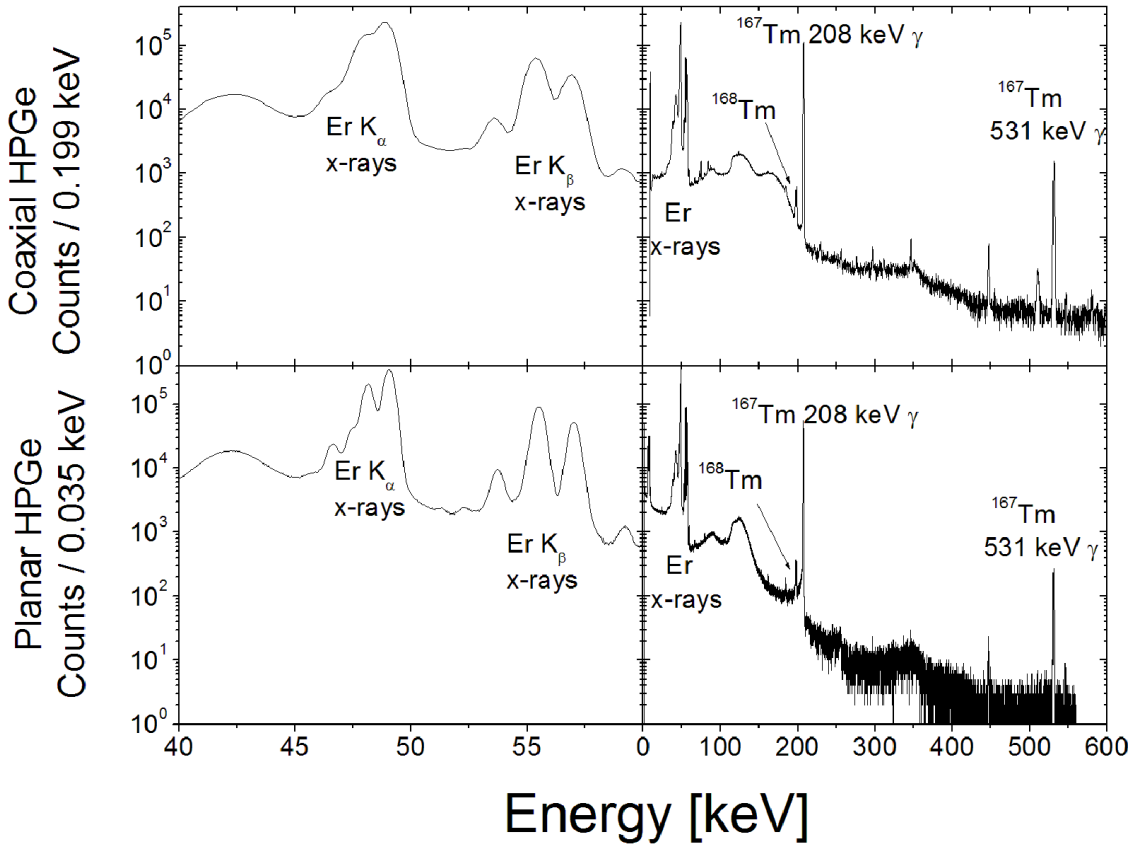

Figure 2.4: Energy spectrum of the irradiated holmium foil measured using planar and coaxial HPGe detectors. Plots on left side show enhanced view of the low energy region, which highlights the superior resolution of the planar detector in the low energy region.

Table 2.4: Branching-ratio results for ^{167}Tm. The measured branching ratios for the 207.8-keV and 531.5-keV γ rays are provided in the last row, with their absolute uncertainties given in parentheses. The primary contributors to these uncertainties are listed at the top of the table, given in relative %.

Primary sources of uncertainty			
	$K_{\alpha 1}$ x ray	207.8 keV	531.5 keV
Counting statistics	0.5%	0.7%	0.4%
Self attenuation in foils	1.1%	0.04%	0.01%
HPGe detector efficiency	2.1%	2.1%	1.8%
$P_{K_{\alpha 1}}$ x ray	2.1%		
Measured absolute BR for ^{167}Tm per 100 EC decays			
		41.9(16)	1.73(7)

Chapter 3

^{169}Tm (n,3n) Cross-Section Measurement

The ^{169}Tm(n,3n)^{167}Tm cross section was determined by exposing thin metal foils to a beam of neutrons of specific energy and then performing offline γ-spectroscopy measurements to determine the quantity of ^{167}Tm that was produced. Quasi-monoenergetic neutrons were produced by the ^{2}H(d,n)^{3}He reaction by bombarding a deuterium gas cell with deuterons accelerated by the High-Voltage FN Tandem Van de Graaff accelerator at TUNL. A stack of 0.9525-cm-diameter foil discs of ^{169}Tm, ^{nat}Ni, and ^{nat}Zr with properties listed in Table 3.1 was placed 0.9 cm from the end of the gas cell. Over five experimental runs, deuterons with energies E_D of 15.0 to 19.2 MeV were used to produce mono-energetic neutrons with energies of 17.5 to 21.5 MeV along the beam axis. Each energy was run for between 6 and 24 hours. Foils were then removed for measurement in a low-background γ-counting facility.

3.1 Previous Measurements

Three previous experiments to measure the ^{169}Tm(n,3n)^{167}Tm reaction cross section have been reported in the literature, each using different techniques. Veeser *et al.* performed measurements of (n,xn) reactions on 10 isotopes, including thulium, using a scintillator-tank method [40]. A pulsed deuteron beam induced the ^{3}H(d,n)^{4}He reaction to produce neutrons which passed through a 75 cm collimator into a large gadolinium-doped liquid scintillator tank. The neutron fluence was determined from measurements with a liquid scintillation detector placed a few meters behind the sample with a high threshold to avoid counting lower-energy breakup and room background neutrons. The thulium target was placed in the center of the tank, and the deuteron beam was pulsed with a duration of 1 μs. Events in the time period from 0.5 to 23.5 μs after the pulse which contained two distinct scintillation events were classified as (n,2n) reactions, and those with three distinct scintillation events were classified as (n,3n).

Bayhurst *et al.* conducted an experimental campaign that measured 236 (n,xn) reactions using radiochemical techniques [41]. The data that overlaps the region studied in this work used ^{3}H(d,n)^{4}He or ^{2}H(t,n)^{4}He for the neutron source, with samples placed 10-15 mm from

a 3.0 cm gas target. Thulium targets were 9.5 mm discs punched from 0.5 mm sheets of polyethylene mixed with Thulium oxide in a 1:1 ratio. Neutron fluence was determined using the ^{27}Al(n,α)^{24}Na reaction as a monitor. Above 20 MeV, where the cross section for many reactions were not well known, a proton-recoil telescope [42] was also used. In this proton-recoil telescope, neutrons interact with a CH_2 radiator, releasing recoil protons. The energy of these recoil protons was then measured with a thin surface barrier transmission detector in coincidence with a large NaI scintillator. Prior to counting, the thulium samples were ignited to remove the polyethylene binder. Samples were then measured in a NaI well counter. Counts due to ^{167}Tm were distinguished from ^{168}Tm using a subtractive technique, where the ^{168}Tm activity was first determined by integrating counts in a high energy region. Contribution of the ^{168}Tm activity to the low energy region was subtracted using a known ratio, and the remaining counts were assumed to be due to ^{167}Tm alone.

Han-lin *et al* also used radiochemical techniques using an accelerator produced ^{3}H(d,n)^{4}He neutron source [43]. The targets were produced from pressed Tm_2O_3 powder and placed at distances between 3 and 10 cm from the source. Neutron fluence was determined using the ^{27}Al(n,α)^{24}Na reaction as a monitor. Counting was performed directly on the face of NaI and Ge(Li) detectors, requiring large corrections for the complicated ^{168}Tm γ-ray cascade. Their study extends only to 18.21 MeV. This work extends the data up to 21.31 MeV and seeks to resolve discrepancy between data of Bayhurst and Veeser in this energy region [24].

3.2 Experiment

3.2.1 Neutron Activation

Neutron activation analysis is a technique in which a sample is exposed to a neutron fluence, and radioactive isotopes created by neutron interactions with nuclei in the sample are measured. This is a non-destructive technique used for trace element analysis for which the neutron cross-sections are well known and it is desired to quantify the presence of isotopes in the sample. In this study, the same technique is applied, but the target composition is well known and the cross-section can be determined. In either case, desirable attributes for isotopes studied are large cross sections for the reaction of interest relative to other reactions that may cause interference, strong γ-ray transitions that can be measured, and a moderate half-life. Half-lives on the order of days are often convenient to work with. If the half-life is very short, it may be difficult to measure the sample before it decays. If the half-life is very long, the activity will be low for a given quantity of atoms, requiring long counting times and making it more challenging to distinguish from background.

Metal foils were used as targets for the study. The use of foils with a small diameter allows for good symmetry when counting with coaxial HPGe detectors. Thin foils were desired to minimize the geometry concerns and limit the corrections required due to self-attenuation of gamma rays emitted by the source distributed throughout the sample volume. Expected activities were estimated based on known cross sections, and foil thicknesses were selected

in order to ensure sufficient activity for measurements following the neutron activation. Because thulium is monoisotopic, there was less possibility for alternate reactions leading to ^{167}Tm. For the thulium foil, a relatively low mass target could be used because it has a 100% abundance of ^{169}Tm and an (n,3n) cross section on the order of barns. In order to determine the neutron fluence that the thulium foils were exposed to, other metal foils were selected to be placed next to the target. The ^{90}Zr(n,2n)^{89}Zr reaction is commonly used as a neutron fluence monitor. ^{90}Zr has a natural isotopic abundance of 51.45%. The possible reaction pathways for the other isotopes of zirconium were scrutinized for interference, either by alternate methods of production of ^{89}Zr or for alternate activation products which would interfere with the 909-keV γ-ray line. It was determined that an isotopically enriched target was not required, and less expensive and more readily available high-purity natural foil was procured. To improve confidence in the fluence measurement, it was desired to use a second method of fluence measurement. Because nuclear data are sparse above 20 MeV relative to lower-energy regions and the limitations previously mentioned for good candidates, options were limited. The ^{58}Ni(n,2n)^{57}Ni reaction was identified as a secondary fluence monitor based on energy threshold, half-life, γ-decay characteristics and evaluated cross section data. During the analysis, it was determined that this was not useful as a monitor. Fig. 3.8c, shows a large amount of scatter in previous experimental data and a literature review offered no explanation for the discrepancies. Therefore, the ^{90}Zr(n,2n) reaction was the only fluence monitor, and experimental results for the ^{58}Ni(n,2n) reaction were evaluated to better determine this cross section.

Thulium, zirconium, and nickel targets were prepared by punching $\frac{3}{8}$ inch diameter discs from larger foil samples, which were then cleaned, inspected, and weighed. Foil thicknesses were determined as described in Chapter 2, Section 2.1.1. A few of the thulium foils were observed to have small chips after being punched, and the more uniform samples were selected for the experiment. Each foil was engraved with the element and a serial number to preclude misidentification of the samples following activation. Foils were stacked with the zirconium closest to the gas cell, followed by thulium, and finally nickel. Because the foils were thin and closely stacked together, and the neutron interaction rates were low, it was estimated that both geometry and neutron shielding concerns were negligible such that the neutron fluence was considered to be identical for the three foils. Foils were mounted to the center of a large diameter aluminum ring with a sheet of cellulose acetate and scotch tape to minimize scattering of neutrons onto the targets. The hoop was mounted 0.9-1.0 cm from the end of the gas cell in order to maximize the neutron fluence. A telescope mounted several meters away was used to visually align the foils with the center of the gas cell and beam path.

An ion source provides ionized deuterium for acceleration. The terminal voltage is selected to produce ions of the desired energy, which are then bent through an analyzing magnet with a magnetic field tuned to pass deuterons with the expected momentum, providing some confirmation of the beam energy. Although focus is applied at multiple points throughout the beamline, the charged particles will naturally repel each other, causing some divergence. The tantalum collimator ensures that the deuteron beam is no more than about 5 mm in diameter. Inevitably, some deuterons that have diverged will strike the collimator.

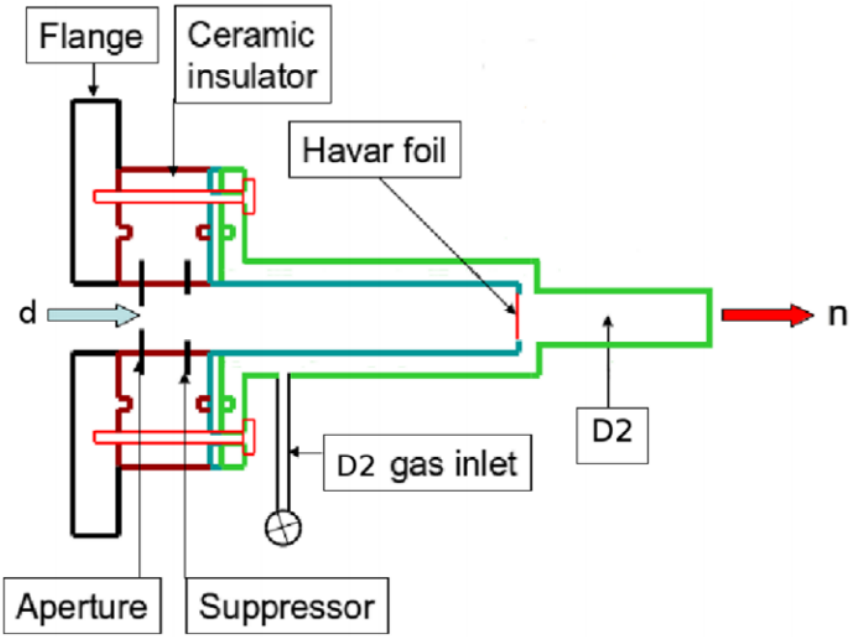

Figure 3.1: Deuterium gas cell used at the end of the accelerator beamline to produce neutron fluence for activation analysis [6].

Table 3.1: Activation samples for branching-ratio and cross-section measurements.

Target	Purity [%]	Thickness [μm]
^{169}Tm*	99.9	261(4)
^{nat}Ni	99.994	514(8)
^{nat}Zr (2.02% Hf)	97.91	241(4)

* Monoisotopic

The remaining beam continues in vacuum until it reaches the 6.5-μm-thick Havar entrance window, which is designed to separate the vacuum line from the deuterium gas, held at a pressure of 5 atm. Deuterons travel through the 3.0-cm-long gas cell pictured in Fig. 3.1, interacting with ^{2}H gas along its path. Those deuterons that do not interact are completely stopped at the end of the gas cell by the tantalum beamstop. The heat generated by these energetic particles is removed by compressed air flow directed at the stainless steel housing of the gas cell.

3.2.2 Neutron Time-of-Flight Measurement

During the experiment, neutrons were produced with a distribution of energies. In addition to the monoenergetic neutrons of interest, deuteron breakup contributes neutrons with

Table 3.2: Deuteron energies (E_D) for the five experimental runs at TUNL and the corresponding neutron energies (E_n). The E_n on axis and the average value of E_n are listed. The energy spread of the neutrons striking the foils is due primarily to the energy spread of the reacting deuterons and the angular dependence of the neutron energy distribution in the ^{2}H(d,n)^{3}He reaction.

E_D [MeV]	On axis E_n [MeV][a]	Average E_n [MeV][b]	Energy Spread FWHM [MeV]
15.02	17.5	17.35	0.18
16.06	18.5	18.34	0.18
17.12	19.5	19.33	0.19
18.12	20.5	20.32	0.19
19.22	21.5	21.31	0.20

[a] Neutron energy calculated for reactions at the center of the gas cell based on the magnet settings

[b] Average energy of neutrons striking the activation foils

lower energies from reactions in the deuterium gas cell, entrance collimator, Havar entrance foil, and tantalum beam stop. The neutron-energy distribution was measured at each energy setting so that the activation by lower-energy neutrons could be corrected. After the activation foils were removed, the neutron beam was pulsed and the neutron time-of-flight (NTOF) was measured with a 3.81-cm-diameter × 3.81-cm-long cylindrical liquid scintillation (BC501A) neutron detector placed along the beam axis at a distance of 287.5 cm from the end of the gas cell. A time-to-digital converter (TDC) was used to measure the time between the deuteron pulse and the detected scintillation light. This produced the data shown in Fig. 3.2.

In order to calibrate the TDC, a timing test was performed by measuring the spectrum while introducing fixed delays using an Ortec 425 delay module. As the inserted delay was varied, the TDC channel locations of the peaks were observed to move. The most easily measured feature is the large peak labeled "3" in Fig. 3.2. The deuterons that strike the beamstop produce high-intensity bremsstrahlung which can be detected with the neutron detector. Using delays between 16 and 35 ns, the TDC calibration constant was measured to be t_{TDC}=199.4 ± 0.2 ps/channel.

In the NTOF spectrum shown in Fig. 3.2, the first notable feature is the peak labeled "1", which occurs when bremsstrahlung generated by deuterons striking the collimator reach the neutron monitor. The detector signal drops for approximately 8 ns while the deuteron beam pulse travels from the collimator to the Havar entrance foil, where the small γ-ray flash labeled "2" is observed, followed by the large peak labeled "3" caused by deuterons striking the beam stop. The γ-rays travel to the detector at the speed of light and are used to determine the time that the deuteron beam pulse arrives at the gas cell. The neutrons

produced in the gas cell travel more slowly, with the highest-energy neutrons arriving before those with lower energy. The peak labeled "4" represents the quasi-monoenergetic peak of the neutrons desired for this study. The broad peak labeled "5" is due to neutrons due to deuteron breakup reactions ^{2}H(d,np)^{2}H and ^{2}H(d,np)np.

The measured NTOF distributions were converted to neutron energy spectra using relativistic kinematics. The time delay relative to the γ-ray flash for neutrons to arrive at the detector was used to calculate the neutron energy using the relationship,

$$E_n = m_n c^2 \left(1 - \frac{1}{\sqrt{1 - \left(\frac{d}{\Delta t \times c}\right)}} \right) , \qquad \Delta t = \Delta t_{0\gamma} + \Delta t_{\gamma n} , \tag{3.1}$$

where E_n is the neutron energy, m_n is the neutron rest mass, d is the distance between the gas cell and the scintillator, Δt is the time between deuteron striking the gas and neutrons being detected, and c is the speed of light. Δt was determined by adding the time it takes for γ rays to travel from the gas cell to the scintillator ($\Delta t_{0\gamma}$) and difference between the measured γ-ray flash and the neutron event ($\Delta t_{\gamma n}$).

The observed neutron distribution then needed to be corrected for the scintillator detection efficiency. Neutron detection efficiency was dependent on the detector threshold. γ-ray sources were used to experimentally determine the threshold. Full absorption of the γ-ray energy within the detector volume is unlikely, but a distinct feature can be observed at the Compton edge, where a photon scatters at an angle of 180^o, transferring the largest amount of energy in a single scatter to an atomic electron within the scintillator. The Compton edge can be calculated by the formula [8]

$$E_e = \frac{2E_\gamma^2}{m_e c^2 + 2E_\gamma} , \tag{3.2}$$

where E_c is the energy of the recoil electron, E_γ is the energy of the incoming photon, and $m_e c^2$ is the rest mass energy of an electron. The optimum location to select for consistent identification of the Compton edge was determined in the work of Ref. [44] to be 0.89 times the maximum height observed. The locations of these Compton edges in the BC501 scintilator were measured relative to the threshold, or "pedestal", of the detector response. For this measurement, the detector threshold was very close to the Compton edge of 0.898-MeV γ ray from ^{88}Y at 0.699 MeV, such that it was not possible to determine the location of this point. The lack of sufficient data to determine the threshold from initial source measurements required the collection of source data at a later date. The detector threshold was set to a lower value, and the γ-ray spectra shown in Fig. 3.3 were used to determine the threshold. The points at higher energies were confirmed to correlate to the original source measurements, and the Δ(ADC Channel) were adjusted to the original pedestal value. The data used for calibration is summarized in Table 3.3.

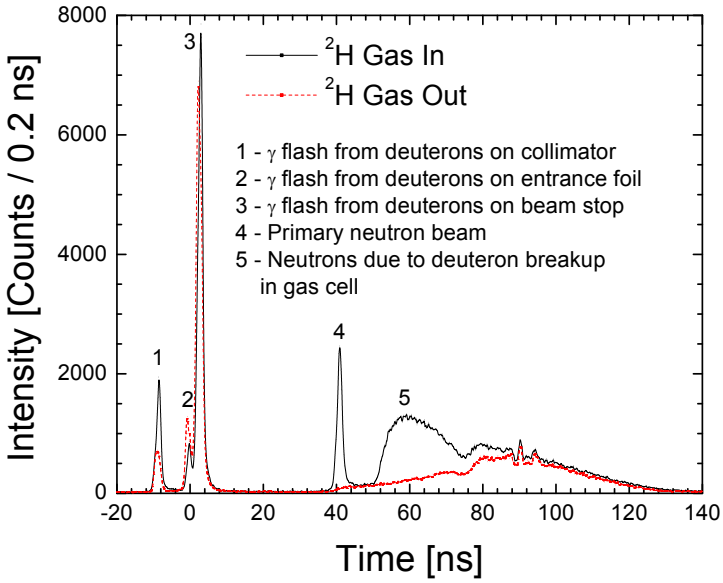

Figure 3.2: Time-of-flight spectrum for the settings used to produce 20.5-MeV neutrons. Additional measurements were performed with ^{2}H removed from gas cell to help identify features noted in the plot.

Table 3.3: Calibration Data for Neutron Detector Threshold Determination.

Source	E_γ [MeV]	E_c [MeV]	Pedestal	E_c [channel]	Δ(ADC Channel)
^{22}Na	1.275	1.062	253.6	298.9	45.3
^{88}Y	0.898	0.699	253.6	254.4	0.8
^{88}Y	1.836	1.611	253.6	358.1	104.5
AmBe	4.439	4.197	253.6	674.0	420.4

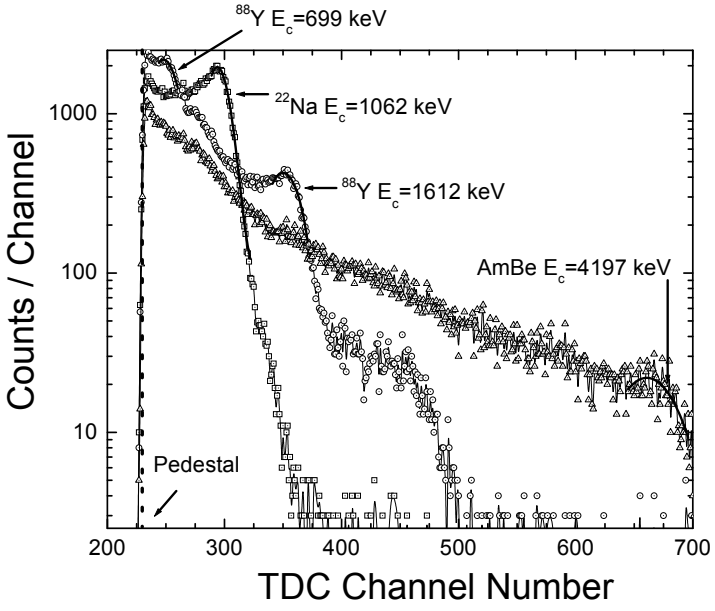

Figure 3.3: Energy spectrum measuring ^{22}Na, ^{88}Y, and AmBe sources for threshold determination of the BC501 neutron scintillator. Features relevant for this analysis are labeled. Note that the detector threshold was lowered for these measurements as described in the text.

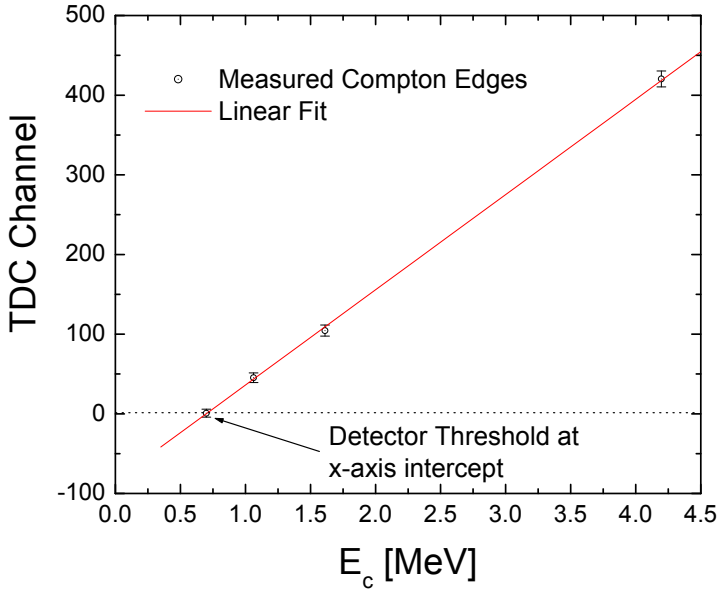

Figure 3.4: γ-ray source calibration of BC501 neutron scintillator threshold.

These data are plotted in Fig. 3.4. The X-intercept of 0.660 MeV represents the energy threshold for detection of Compton events. Detection threshold for neutron scintillators is typically quantified relative to the 0.478 MeV Compton edge due to ^{137}Cs γ rays. For this experiment, the threshold was determined to be 1.38×Cs.

Neutron detection efficiency curves for 1×Cs and 2×Cs for a NE-213 scintillator were obtained from Ref. [7]. It was assumed that the differences in energy response between the NE-213 and BC501A scintillator materials were negligible and an interpolation was performed to get results for 1.38×Cs. Results are shown in Fig. 3.5. It is important to note that the absolute efficiency was not needed for this experiment. Total neutron fluence was determined by offline measurements of the activated Zr monitor foils. The relative efficiency, as interpreted by the shape of the curve, was used for convolution with the various excitation functions described later in this chapter.

The finite time resolution of the pulsing system, as determined by the width of the γ-ray flash from deuterons on the collimator, dominates the observed width of the quasi-monoenergetic peak. The energy of the quasi-monoenergetic neutron peaks measured in this way were consistent with the estimates based on the Tandem settings. Sensitivity calculations were performed, and the impact of this broadening on the calculation of cross sections was determined to be negligible.

The energy distribution of the neutrons impinging on the foil is broadened by two effects. First, the reacting deuterons have an energy spread caused by energy-loss effects in the 6.5-μm Havar entrance foil and across the gas cell. These effects were determined by a Monte

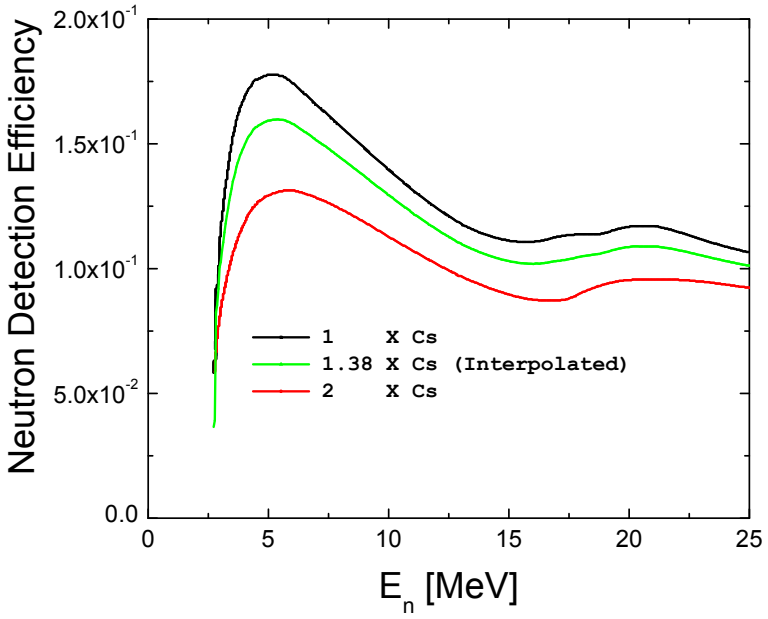

Figure 3.5: Neutron detection efficiency for BC501A liquid scintillator used for NTOF measurements [7].

Carlo method using the Stopping Range in Matter (SRIM) program [45]. Second, with such a small distance between the gas cell and the activation foils, neutrons emitted off the beam axis can strike the foil. Because of the kinematics, the off-axis neutrons have a lower energy than the neutrons emitted parallel to the deuteron beam. Although it represents a small population of the neutrons, angles up to 39° were possible, whereas the distance between the liquid scintillator detector and the gas cell ensured that only the on-axis neutrons were detected. This kinematic effect was taken into account using the differential cross section of the ^{2}H(d,n)^{3}He reaction [7] and assuming uniform production along the length of the gas cell. Using this data, numerical methods were used to integrate the source term along the 3-cm length of the gas cell with a beam diameter of 5 mm for neutrons reaching the 0.9525 cm foil located 0.9 cm from the end of the beam stop. As an example, for the settings that produced 21.5-MeV neutrons at the center of the gas cell, the energy distribution of the neutrons hitting the foils is shown in Figure 3.6. The spread in neutron energies at other settings is similar in shape. A summary of the average energies of the neutrons in the mono-energetic peak and their energy spread is presented in Table 3.2.

The same methods were applied for each of the energy runs, with the results shown in Fig 3.7. Note that the quantity of lower-energy neutrons increases as beam energy increases and the energy of the breakup neutrons increase as well. Because the NTOF data was obtained with equal time bin widths, the bin widths are non-uniform after performing the conversion to energy, with the lower energy bin widths being more closely spaced. To make

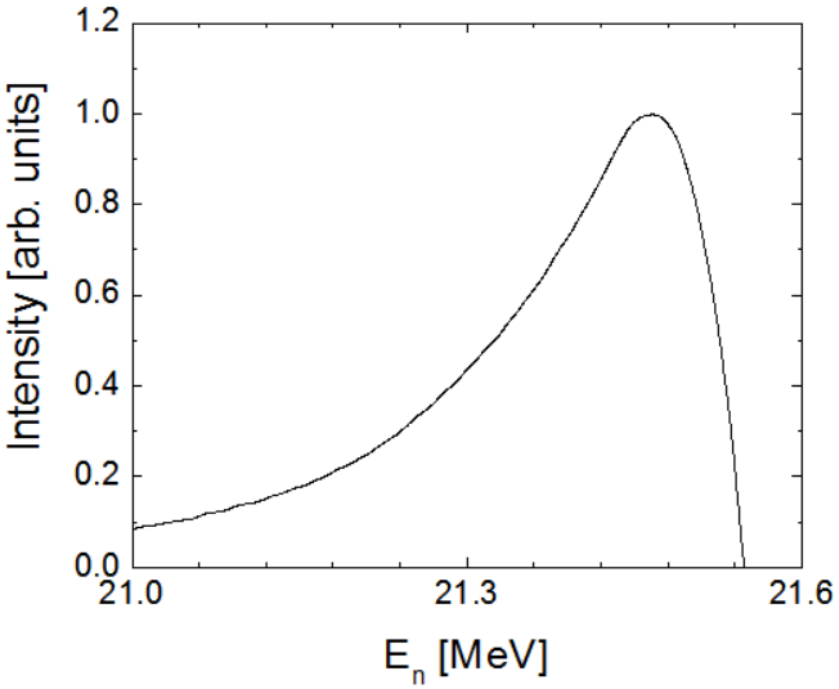

Figure 3.6: Calculated energy distribution of neutrons striking the foil at the 21.5-MeV settings. The spread in neutron energies is primarily caused by kinematic effects due to the extended geometry of the foil.

this plot more intuitive, the counts in each bin were divided by the bin width. Since the number neutrons in each bin in the unadjusted data is correct, this final modification was not used for the numerical convolution described later in this chapter which was performed bin by bin in preference to fitting a function to the distribution.

3.2.3 Corrections for Time

Neutron activation occurred over the course of several hours for each energy studied. The radioisotopes had half-lives on the order of hours or days.

During the activation period, the accelerator was operated in direct current (non-pulsed) mode. Minor fluctuations occurred during the production phase, and at some times the beam current dropped to zero due to tank sparks, particularly at the highest energies. Time variations in neutron fluence during activation were inferred from variations in deuteron beam current. The data acquisition system recorded a beam current integrator (BCI) at intervals of eight seconds. Correction factors were calculated for each isotope studied based on the minor variations in beam current during activation for each run according to the

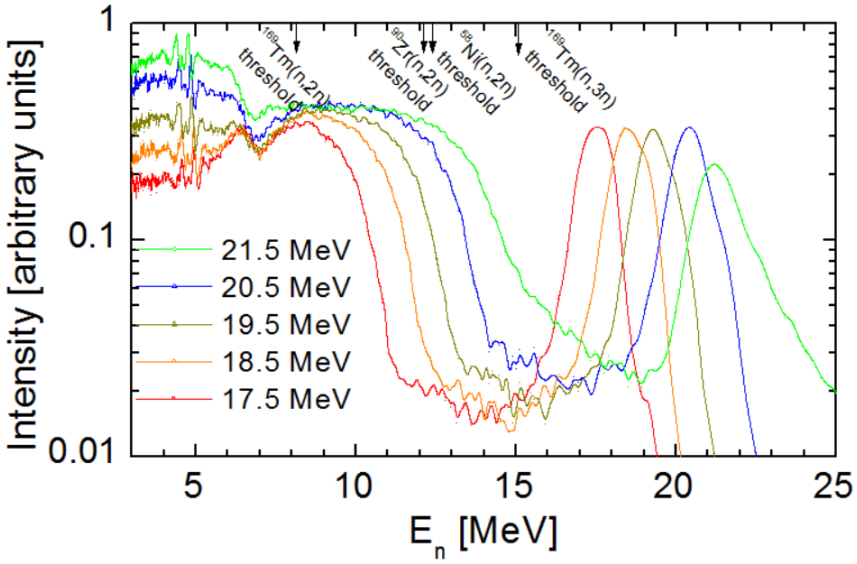

Figure 3.7: Neutron-energy spectra determined from time-of-flight measurements. The spectra are normalized by area in the quasi-monoenergetic peak and are shown with equal energy bin widths. The time-of-flight measurement at the 21.5-MeV settings was performed under timing conditions that resulted in greater broadening of the highest-energy neutrons.

equation [46]

$$c_{fluence} = \frac{\bar{\Phi}\left(1 - e^{-\lambda t_i}\right)}{\sum_{i=1}^{n} \Phi_i \left(1 - e^{-\lambda \Delta t}\right) e^{-\lambda (n-i)\Delta t}} \,, \tag{3.3}$$

where $c_{fluence}$ is the correction factor for fluence variations during the activation period, $\bar{\Phi}$ is the average fluence over the entire activation period, λ is the decay constant for the isotope of interest, t_i is the BCI time interval, n is the total number of intervals recorded during the activation period, $\bar{\Phi}_i$ is the fluence during the BCI interval i, and Δt is the time interval between i and n. $c_{fluence}$ was calculated for each isotope of interest for each run. Because the beam current time variations were small, the activation periods were on the order of hours, and the half-lives of the isotopes studied were on the order of days, this correction was less than 0.3% in all cases.

More significant correction factors were applied to account for radioactive decay of the sample between production and measurement as well as decay during measurement. The activity, corrected to the time at the end of the activation is given by

$$A_o = \frac{\lambda C e^{\lambda t_d} t_r}{I_\gamma \epsilon_\gamma c_{fluence} \left(1 - e^{-\lambda t_r}\right) a_f t_\ell} \,. \tag{3.4}$$

In Eq. 3.4, A_o is the activity at the end of the activation, λ is the decay constant for the isotope of interest, C is the number of net peak counts, t_d is the time elapsed between the

end of the activation and the beginning of the counting period, t_r is the real time of the measurement, I_γ is the γ-ray branching ratio, ϵ_γ is the photopeak efficiency, $c_{fluence}$ is the fluence fluctuation correction factor given by Eq. 3.3, a_f is the self attenuation correction factor, and t_ℓ is the live time of the measurement.

3.2.4 Corrections for Neutron Energy Distribution

In addition to the activation caused by the monoenergetic neutrons produced by the ^{2}H(d,n)^{3}He reaction, the lower-energy neutrons from deuteron breakup can also induce activity in the foils if their energy is above the threshold for the reaction of interest. In order to correct for activation due to lower-energy neutrons, Eq. 3.5 was used to determine the fractional contribution (FC) of the activity induced due to the breakup neutrons relative to the total activity induced [47],

$$FC = \frac{\int_0^{E_c} \phi(E)\sigma(E)dE}{\int_0^{E_c} \phi(E)\sigma(E)dE + \phi_x\sigma_x} \ . \tag{3.5}$$

In Eq. 3.5, ϕ(E) is the neutron energy distribution determined by the NTOF measurements, σ(E) is the cross section for the reaction of interest, E$_c$ is the cut-off energy taken as the minimum point in the valley between the neutron peak and the deuteron breakup, ϕ_x is the integration of the neutron peak, and σ_x is the cross section at the peak energy. This factor was determined for each reaction of interest using excitation functions from nuclear data evaluations. The activity due to the quasi-monoenergetic neutrons, A_{ϕ_x}, could then be calculated as

$$A_{\phi_x} = A_o(1 - FC) \ , \tag{3.6}$$

where A_o is the total activity at the end of the activation, and FC is the fluence correction.

In all cases, only the shape of the cross section impacted the correction. The calculated FC values were more sensitive to uncertainties in the neutron-energy distribution than to differences between evaluated cross sections. For Tm(n,Xn) reactions, the ENDF/B-VII.1 evaluation was used. For the reactions that do not have ENDF evaluations above 20 MeV, other sources were used. Data for the ^{90}Zr(n,2n) reaction was taken from the International Nuclear Data Committee evaluation [48], while for the ^{94}Zr(n,α) reaction, the JEFF-3.2 evaluation [5] was used and for the ^{58}Ni(n,2n) reaction, the IRDFF-1.05 evaluation [5] was used. Uncertainty in FC includes the uncertainty from the excitation curve and the measured NTOF distribution propagated through Eq. 3.5. The calculated fluence corrections for each energy and isotope are shown in Table 3.4.

3.2.5 Measurement of Activated Foils

Following each activation, the foils were removed and γ-ray counting began in less than an hour at the TUNL low background counting facility. Two detectors at TUNL were used for

Table 3.4: fluence correction (FC) factors calculated by Eq. 3.5 to account for activation by lower-energy neutrons produced from deuteron breakup.

Reaction Energy [MeV]	^{90}Zr(n,2n) FC	^{169}Tm(n,2n) FC	^{169}Tm(n,3n) FC	^{58}Ni(n,2n) FC	^{94}Zr(n,α) FC
17.35(10)	0.0523(26)	0.394(20)	0.00593(30)	0.0422(21)	0.118(6)
18.34(10)	0.0735(37)	0.609(30)	0.0108(5)	0.0590(3)	0.189(9)
19.33(10)	0.122(6)	0.765(38)	0.0224(11)	0.0950(5)	0.301(15)
20.32(10)	0.210(11)	0.856(21)	0.0424(21)	0.149(7)	0.438(22)
21.31(10)	0.440(22)	0.924(46)	0.117(6)	0.331(16)	0.645(32)

Table 3.5: Decay data for nuclear reactions used in this work [5].

Reaction	Q-value [MeV]	Product half-life	E_γ [keV]	I_γ
^{90}Zr(n,2n)^{89}Zr	−11.7	78.41(12)h	909.15(15)	0.9904(3)
^{169}Tm(n,2n)^{168}Tm	−8.03	93.1(2)d	198.251(2)	0.5449(16)
			815.989(5)	0.5095(16)
^{169}Tm(n,3n)^{167}Tm	−14.9	9.25(2)d	207.801(5)	0.419(16)
^{58}Ni(n,2n)^{57}Ni	−12.2	35.60(6)h	1377.63(3)	0.817(24)
^{94}Zr(n,α)^{91}Sr	+2.03	9.63(5)h	1024.3(1)	0.335(11)

the first several days, so that all three foils from each activation energy were counted at least twice to confirm appropriate levels of activity were obtained and to screen for anomalies. The foils were then shipped to UC Berkeley, where counting was continued by rotating samples on a single detector. Calibration of all three HPGe detectors were performed as described in Section 2.1.2, although with different calibration sources at each location. The decay corrected activities of the foils used in the experiment were used as a cross check for consistency of calibration between the detectors. In both locations, the foils were counted at a distance of approximately 10 cm. The primary γ-ray lines used for identifying isotopes are listed in Table 3.5.

3.3 Results and Discussion

The neutron fluence was determined from the ^{90}Zr(n,2n)^{89}Zr monitor reaction using the cross section from Ref. [48], which had uncertainties which varied between 1.44% to 3.46% in the energy range studied.

Cross sections were measured for the reactions listed in Table 3.6. For the ^{169}Tm(n,2n) and ^{94}Zr(n,α) reactions, for which the mono-energetic neutron peak was much higher in energy than the reaction threshold, the fluence correction (Table 3.4) was the largest con-

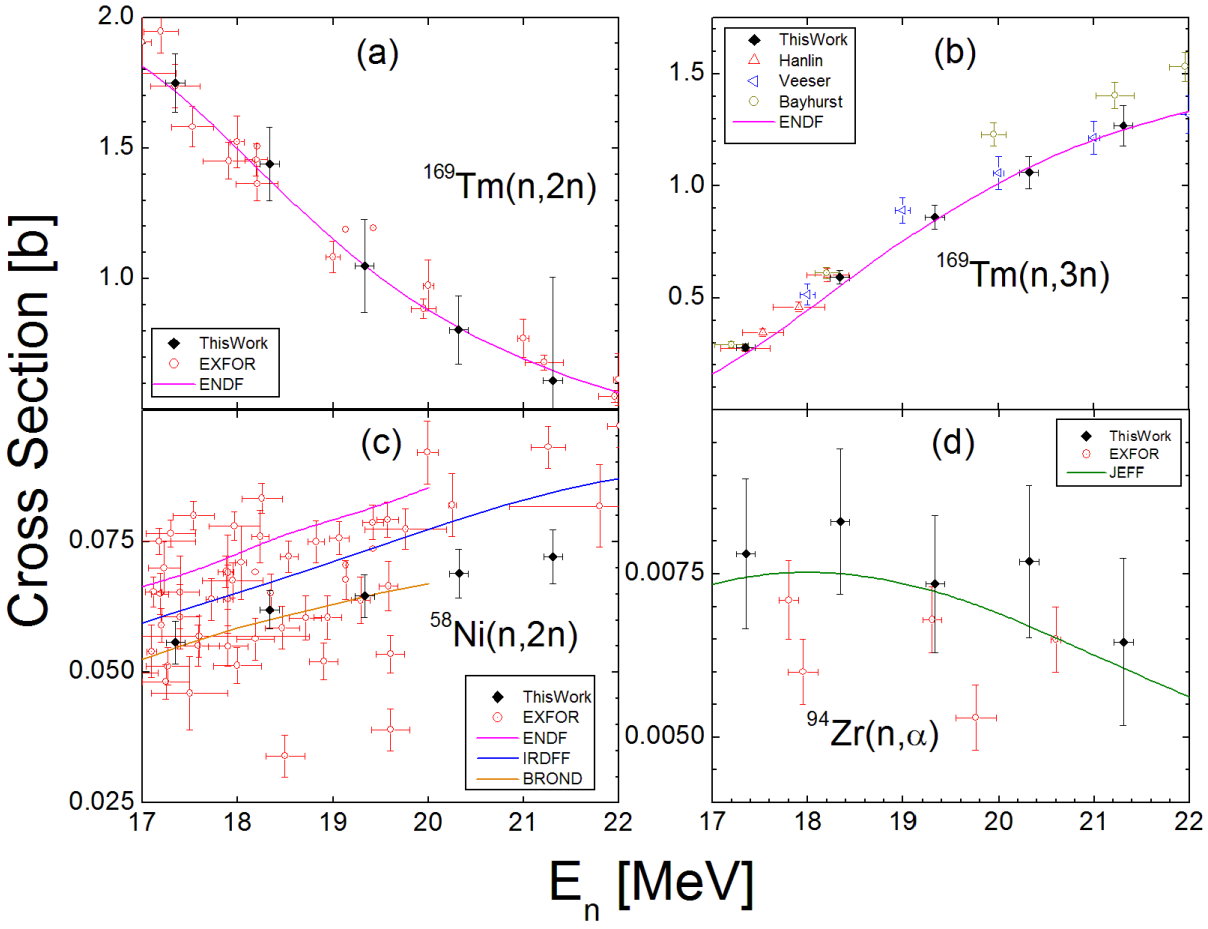

Figure 3.8: Experimental results from this work compared with the previous data summarized in EXFOR and evaluations [5].

Table 3.6: Measured cross sections.

Reaction Energy [MeV]	^{169}Tm(n,2n)^{168}Tm σ [b]	^{169}Tm(n,3n)^{167}Tm σ [b]	^{58}Ni(n,2n)^{57}Ni σ [b]	^{94}Zr(n,α)^{91}Sr σ [b]
17.35(10)	1.75(12)	0.279(15)	0.056(4)	0.0078(12)
18.34(10)	1.44(14)	0.593(31)	0.062(4)	0.0083(12)
19.33(10)	1.05(19)	0.861(54)	0.065(5)	0.0074(11)
20.32(10)	0.804(134)	1.06(7)	0.069(5)	0.0077(12)
21.31(10)	0.611(369)	1.27(10)	0.072(5)	0.0065(13)

tributor to uncertainty. The agreement of the present ^{169}Tm(n,2n) cross-section results with previous experimental data [5] demonstrates that the NTOF measurements and lower-energy-neutron correction techniques are reliable. This provides confidence in the smaller corrections applied for other reactions. Other significant sources of uncertainty were HPGe γ-ray detection efficiency (2–3%), and in some cases, the γ-ray branching ratios. Other factors in the calculation contribute uncertainties of less than 1%.

Existing experimental cross-section data for the ^{58}Ni(n,2n)^{57}Ni reaction is discrepant [5]. As shown in Fig. 3.8c, the uncertainty of the individual measurements is of the order of 10%, however, the literature values for this cross section span nearly a factor of two in the energy range 17–22 MeV. The present data agrees with the evaluation by Brond [5].

Results for ^{94}Zr(n,α)^{91}Sr are also reported for which only two other measurements have been made in this energy region [49, 50]. Although the (n,α) cross section is much smaller than the (n,2n) and (n,3n) cross sections for ^{94}Zr, it carries important additional information that constrains nuclear models used to determine optical model and energy level density parameters. Our ^{94}Zr(n,α) cross-section results support the JEFF 3.2 evaluation.

The detection of the 207.8-keV γ ray simplifies the measurement of ^{167}Tm production and minimizes the assumptions required to interpret the data. This work confirms the ^{169}Tm(n,3n)^{167}Tm cross section ENDF evaluation and the Veeser *et al.* [40] results as can be seen in Fig. 3.8b, and provides strong evidence that the experimental results of Bayhurst *et al.* [41] are 15–20% too large. These cross-section results along with the improved branching ratio determined in Chapter 2 provide reliable nuclear data which reduce the overall uncertainties on the measured reaction-in-flight yield at NIF to about 5–8% in an important energy region between 17 and 22 MeV.

Chapter 4

4π Beta Proportional Counters for Absolute Activity Measurement

4π proportional counters were first used in 1949 by the National Bureau of Standards to measure disintegration rates and were widely used through the 1960's for activity standardization of alpha and beta emitting sources as well as low energy x-ray measurements. With the advent of semiconductor detector technologies, these detectors are much less commonly used [51]. Today, this detector type is used as a high-efficiency counter in special applications of high-precision β measurements, most notably in the work of Hardy *et al* [52].

The fission product branching ratio measurements performed as part of this dissertation require a detector with a very low threshold and nearly 100% efficiency. A 4π beta proportional counter is ideally suited for this task. In this chapter, I describe the characteristics of 4π beta proportional counters, and the adaptations incorporated into the design of a new detector to meet these requirements.

4.1 Theory of Operation

When charged particles pass through gas, they transfer energy primarily through ionization and excitation. When a sufficient potential difference is applied across the gas volume, the ion pairs can be collected before recombination. As the potential is increased, electrons created due to ionization of the gas are accelerated to sufficient energy to cause further ionizations. The region in which the charge collected is proportional to the energy deposited in the gas is known as the Proportional region. Beyond the Proportional region, non-linearities are introduced resulting in Limited Proportionality. In the highest region, each ion experiences sufficient multiplication to induce space-charge effects that prevent further charge multiplication. This is known as the Geiger-Mueller region, in which each pulse is of the same magnitude. The regions are plotted depicting two different amounts of energy deposited in the gas in Fig. 4.1.

Gas multiplication has a threshold on the order of 10^6 V/m. In order to achieve such

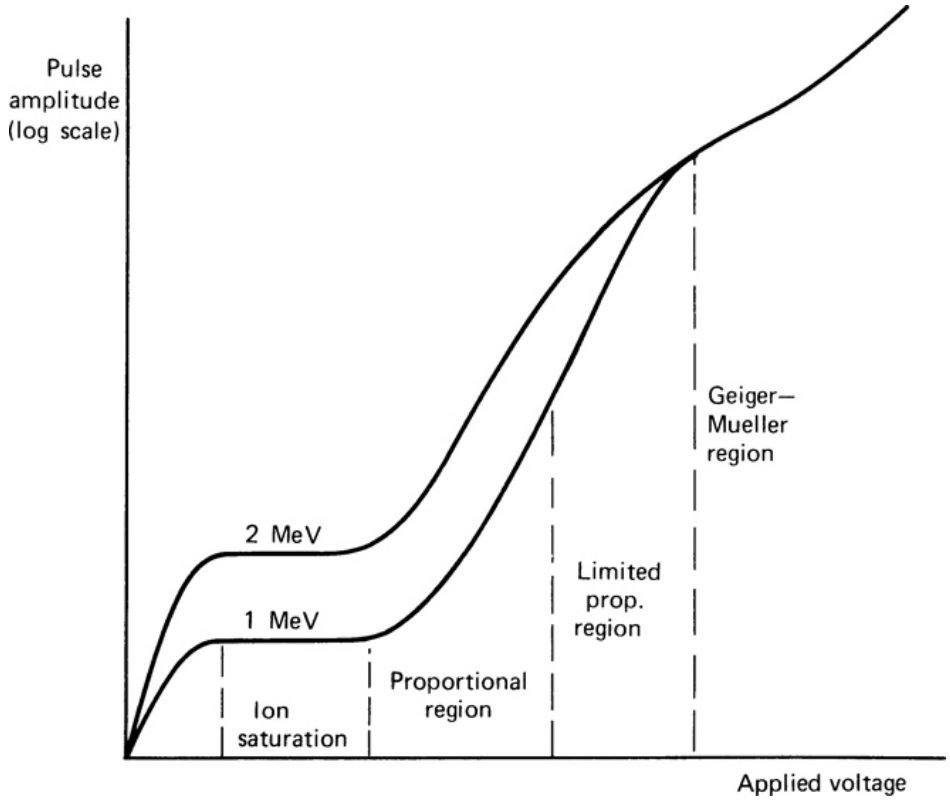

Figure 4.1: Regions of operation of gas-filled detectors [8].

large electric fields, cylindrical geometry is commonly used, with a very thin anode wire. Since electric potential varies with 1/r, ion pairs created in the detector volume drift, and multiplication only occurs very close to the anode wire, where the potential is very large. Air has a very low gas multiplication rate compared to other gases, so detectors are filled with a gas selected for its higher multiplication factor. The detector may be sealed to prevent air exchange, or it may be operated with gas flowing through the volume. High voltage is applied across the detector, and then the small fluctuations in potential caused by the charge collection are interpreted as ionization events within the gas.

4.2 Detector Construction

4.2.1 Design

The design of this chamber was largely borrowed from that of Koslowsky *et al* [53], with modifications to allow for a lower beta energy threshold to be achieved. In order to count with a 4π geometry, the source must be in the center of the detector such that radiation emitted in any direction will enter the gas. An aluminum frame with a 1.0 cm aperture allows thin carbon foils to be mounted, surrounded by several holes to equalize gas pressure

Figure 4.2: Aluminum frame with 40 μg/cm^2 carbon foil mounted. This frame inserts into the center of the copper detector body.

to prevent damage to the delicate foil, as shown in Fig. 4.2.

The detector body was machined out of oxygen-free copper with a cylindrical cavity as shown in Fig. 4.3. In the center of each cavity is a 12.7-μm diameter gold-plated tungsten anode wire. Teflon insulators seal the penetrations through which the anode wire passes. Rubber o-rings seal the surfaces between the detector body and the aluminum frame which holds the carbon foil. Gas inlet and outlet on each side are tapped for pipe threads to connect to the gas handling system. The outlet is 0.125 inches in diameter, but the inlet is reduced to 0.016 inches to restrict gas flow and prevent damage to the detector in the case of an accidental overpressure from the gas system. Two exterior faces of the chamber are fitted with aluminum window frames that are covered with 50-μm-thick aluminized Mylar sealed with silver epoxy. The Mylar windows allow for γ rays to escape the detector with minimal attenuation. These windows may be unscrewed from the copper housing for ease of access during detector assembly and maintenance, and seal with rubber o-rings during normal operation.

The original prototype for our detector required the detector body to be unbolted and the two halves completely separated in order to insert or remove a source from the center of the gas volume. In doing so, the gas volume is completely exchanged with air. Because low gas flow rates are desired to minimize the potential for damage to the fragile carbon foils, it would take many hours for the oxygen to be displaced after the detector is resealed. Additionally, every time the detector is opened, the fragile anode wires are exposed. This opens up the possibility for the wires to get broken, which would require at least a day to repair and several more days to retest and recalibrate. Any opening can also allow dust to enter into the system, which may attach to the anode wire once HV is applied to the detector, potentially affecting

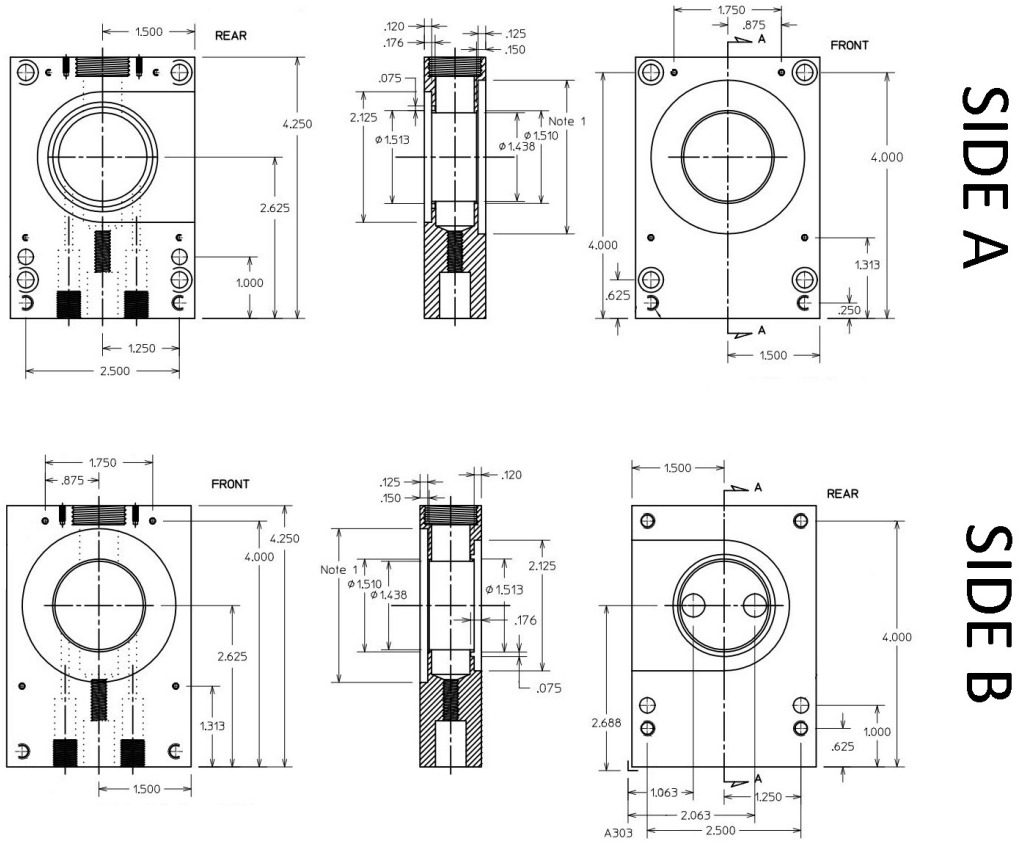

Figure 4.3: Schematic drawing of beta detector housing. All dimensions shown are in inches.

the detector performance. For these reasons, design modifications inspired by Ref. [51] were implemented, in which the aluminum holder can slide in from the side, as shown in Fig. 4.4. In this way, the source can be changed in a few seconds, with a minimal amount of air exchanged. Because the tolerances are small, attempting to slide the aluminum holder in or out can either shear or dislodge an o-ring. Displacement of the o-ring would, at a minimum, require the detector to be completely opened to replace the o-ring. Worse still, the dislodged o-ring could damage the source or one of the anode wires. To minimize these risks, the bolts holding the housing together can be loosed by half of a turn during sample change, and then re-tightened.

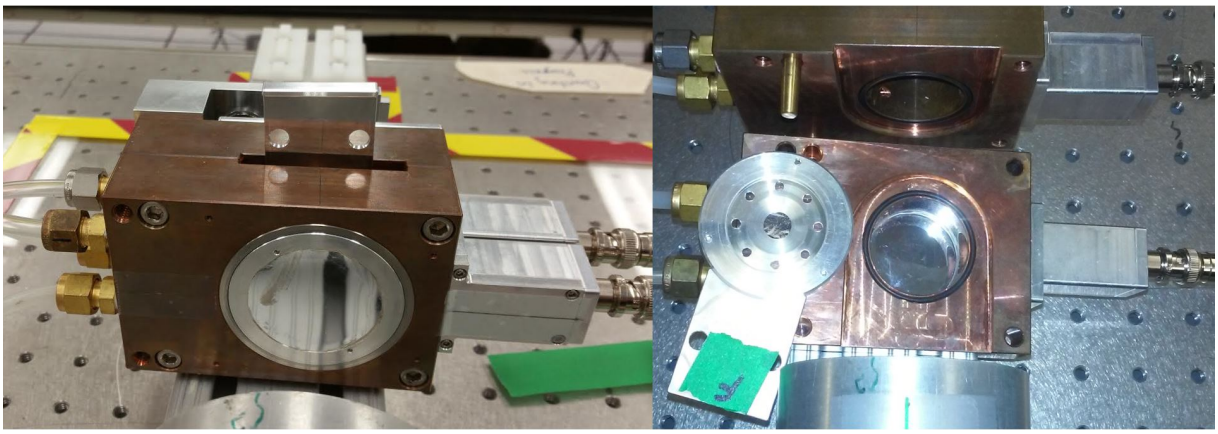

Figure 4.4: 4π beta proportional counter designed for use in this study.

4.2.2 Anode Wire Assembly

After the detector has been machined, the most challenging task in assembling the detector is the stringing of the anode wire. To ensure desirable operating characteristics, each wire must be mounted under tension in order to minimize the sag due to electrostatic force when the high voltage is applied. The small dimensions of the wire make it difficult to see and manipulate, and the wire can be stretched or broken with excess tension. One end of the wire was attached with epoxy to a small piece of plastic which could fit inside the lower Teflon insulator, but not pass through the opening into the detector. A thicker wire, approximately 0.1 mm in diameter, was soldered to the other side of the wire at 3.25 inches beyond the anchor point. This thicker wire had sufficient stiffness to be threaded through the lower Teflon insulator, carrying the anode wire along with it. This was then passed through the upper Teflon insulator so that only the anode wire is exposed inside the chamber, and the thicker wire can be used for the electrical connection. To maintain tension, a 10 g weight was attached to the wire as shown in Fig. 4.5. While the wire remained under tension, conducting silver epoxy was applied to ensure good electrical connection. The silver epoxy is rather soft and not sufficiently strong to hold the wire in place, so it was allowed to cure, and then a traditional epoxy was applied on top of this. The exposed end of the wire was

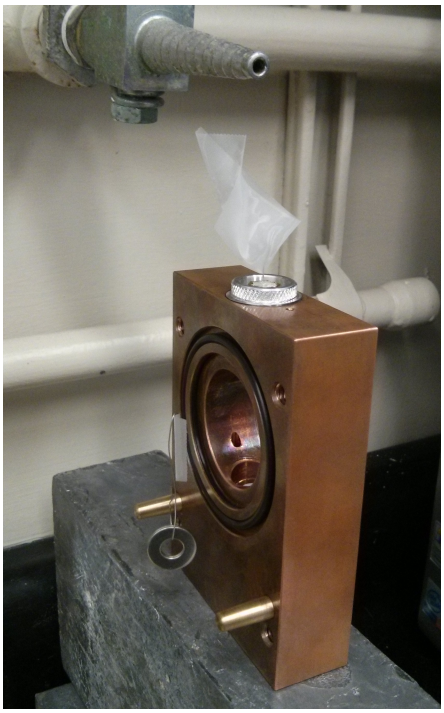

Figure 4.5: Anode wire placement: a small weight is used to apply tension on the wire while epoxy is applied and allowed to cure.

soldered to an SHV bulkhead connector mounted with an aluminum housing bolted to the copper block.

4.2.3 Gas Handling

Methane was found to be preferable to an Argon-Methane mixture such as P-10 gas that is used as a proportional gas in many other applications [8]. Because methane has a much lower effective atomic number, the probability of x-ray or γ-ray interactions in the gas is greatly reduced [54]. Although many aspects of the design were incorporated to maintain the detector sealed from outside air, it is not completely air-tight. To maintain the methane atmosphere in the active detector volume, gas is introduced at a rate of 1 cm^3/min. A two-stage regulator is used to reduce the methane cylinder pressure to 5 psi leading to a needle valve to precisely control the gas flow. Swagelok fittings and $\frac{1}{8}$ inch vinyl tubing were used for connections for the remainder of the system. A high precision microtube flow meter allowed for monitoring the flow of gas into the detector. The gas outlets were connected to several meters of tubing vented to the atmosphere. This provided a small positive pressure inside the detector and created a very long pathway that obstructed gaseous diffusion of oxygen through the exhaust lines.

4.2.4 Electronics

Beta Counter Analog Electronics

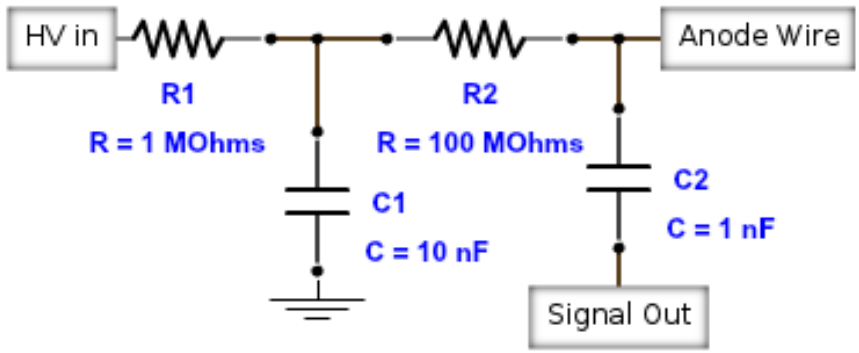

Figure 4.6: Circuit used to connect HVPS to anode wire and extract the β signal.

The detector was biased using a DC 5 kV high voltage power supply (HVPS). Both anode wires were connected to a common output of the HVPS to prevent any imbalance in the bias applied. Initially, much of the detector electronics were duplicated from the system at Texas A&M, which has been extensively tested in used in a series of very high precision half-life measurements [55]. In order to connect the DC high voltage and extract the small AC signal, an RC circuit was built with BNC and SHV connections as shown in Fig. 4.6. The output signal was connected to a Phillips Scientific model 6950 bipolar amplifier with input impedance modified from 50 Ωs to 1000 Ω.

At this point in the signal chain, a significant amount of difficulty was encountered. Although the systems were very similar, and the amplifier purchased was an identical model, the output of the amplifier produced very large, high-frequency oscillations that were several orders of magnitude greater than the input signal. After discussion with vendor technical representatives and remote troubleshooting provided by Victor Iacob of Texas A&M, he allowed us to send one of our Model 6950s to connect to his own system. The conclusion was that the unit's performance made it unusable, but the root cause could not be determined. The most likely explanation was that some "equivalent" components were substituted by the manufacturer over the course of the 20 years that passed between Texas A&M's purchase and our own, which had no detrimental effect for the majority of their customers, but in our application with the modified input impedance, an instability was introduced. Because the oscillations were of a much higher frequency than the signal, much of it could be smoothed by integration through use of a spectroscopy amplifier or other electronics. These solutions had several disadvantages. First, any additional components in the signal processing introduced more pathways for noise to enter, thus increasing the electronic noise threshold. Additionally, increased integrating time could also could also smooth out some of the smallest β signals, which is a significant problem for studying a β decay which includes a

large component of low-energy β particles which need to be counted in order to approach the desired 100% efficiency goal. Finally, shaping times of these amplifiers were on the order of μs, increasing the effective dead time of the detector significantly. A number of pre-amplifers were tested to substitute for the 6950. The Ortec 142IH, had an even longer characteristic decay time and a gain so high that it often saturated on the signals, resulting in poor linearity. The Ortec 113, when connected between the signal separator and the 6950 did remove the severe oscillations, but also provided no amplifier gain. The output of the detector was also connected without a preamp directly to either a spectroscopy amplifier or a fast timing filter amplifier. These solutions overall provided some signal amplification, but still retained undesirable noise characteristics. No completely satisfactory solution was found for analog electronics signal processing of the β signals.

HPGe Analog and Coincidence Electronics

The HPGe signal was measured using a standard configuration with an Ortec 672 spectroscopy amplifier and either an Ortec Aspec 927 two channel 16k MCA or an 8k Easy MCA, and spectra were recorded using Maestro software. For some measurements, the outputs from the spectroscopy amplifier were split, and it was desired that each provide identical output. In order to evaluate this, spectra were measured and compared, first using two identical Easy MCAs, and later using the two channels from the Aspec 927. Net peak counts measured in the spectra recorded with the two Easy MCAs differed by greater than 1% although they both had the same settings and input. Tests with the Aspec 927 proved to be more consistent, with net peak counts in the spectra recorded being within 0.1%, so this became the preferred hardware for such measurements.

List mode data collection was not possible with the equipment on hand. In order to collect a γ-ray spectrum coincident with β counts, the output of the spectroscopy amplifier connected to the HPGe was split and connected to two identical ADCs. One ADC collected ungated event mode data. The output of the β counter was amplified and then sent through a leading edge discriminator, producing a logic pulse. The logic signal was passed to a gate and delay generator and the delay was adjusted to match the fast signal of the β counter with the slower signal of the HPGe, and then connected to the gate input on the second ADC. A schematic is shown in Fig. 4.7.

In order to collect a β spectrum coincident with a specific γ-ray photopeak, the output of the spectroscopy amplifier was sent to a single channel analyzer (SCA). While observing the recorded γ-ray spectrum gated on the SCA, the upper level (ULD) and lower level discriminators (LLD) were adjusted until only the γ-ray photopeak was observed. Once adjusted, the logic pulse output of the SCA was delayed with a delay amplifier such that the slow γ-ray signal coincided with the faster β signal. The β signal was processed with a spectroscopy amplifier and connected to the input of the ADC, while the delayed γ logic pulse was used as a gate. In this way, a β spectrum could be collected which correlated to a specific γ-ray photopeak. To account for background events under the photopeak, the ULD and LLD were adjusted to similarly sized regions above and below the photopeak, and the

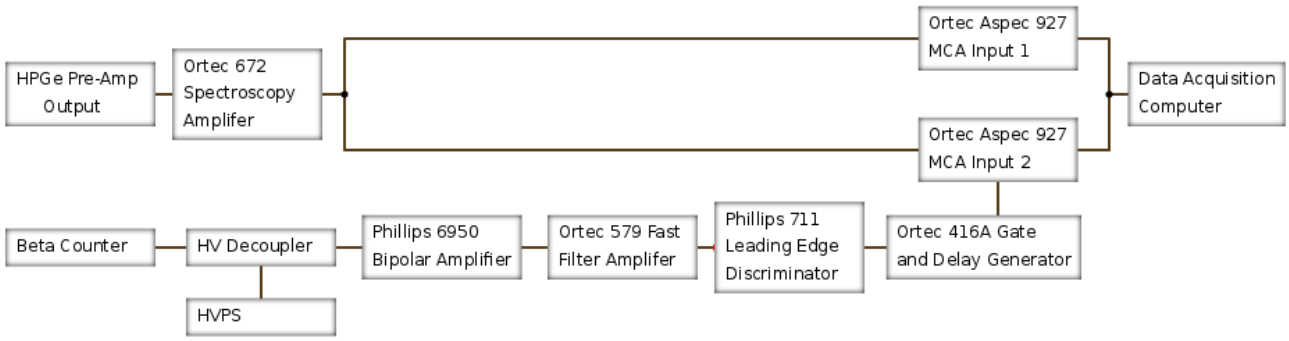

Figure 4.7: Modules used to simultaneously collect spectra for γ-ray singles and γ-rays gated on β counts.

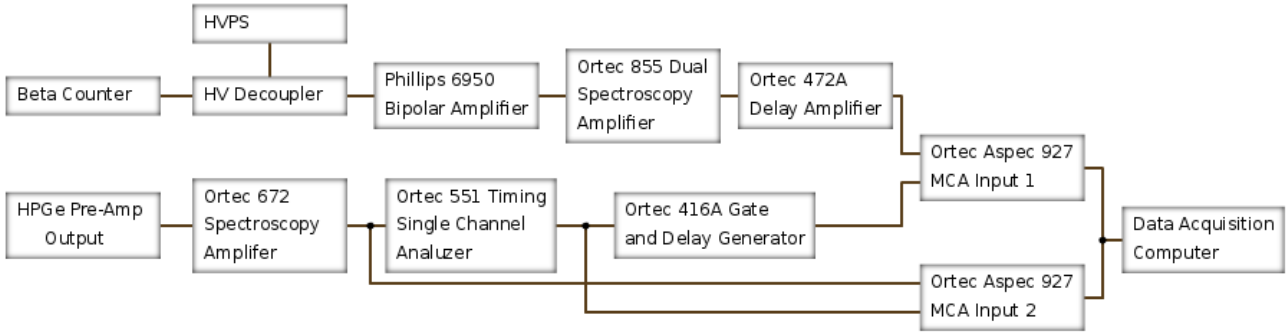

Figure 4.8: Modules used to collect β spectra gated on specific γ-ray photopeaks.

β spectra were recorded for subtraction. A schematic is shown in Fig. 4.8.

Digital Multichannel Analyzer System

Another option that emerged during this work was the use of a CAEN DT-5781 digital multichannel analyzer (MCA), which was sensitive enough to accept low amplitude input directly from the β counter. The unit applied a digital trapezoidal filter, as described in Ref. [56], which can decrease dead time, reduce the amount of pule-pileup, and overall decrease the number of components and therefore points of signal loss and noise generation. It also added in the capability of recording data in list mode with a common time stamp across 4 channels. Using this system, the γ-ray spectra were recorded with one channel, and each half of the β counter were recorded on their own channels. A schematic is shown in Fig. 4.9.

Although the system has built-in coincidence capability with adjustable time windows and logic, this mode of operation records only coincident events and discards the rest of the data. For greater flexibility, all events were recorded, and analysis was performed off-line to sort coincidences between the various channels. Because the digital MCA was obtained in

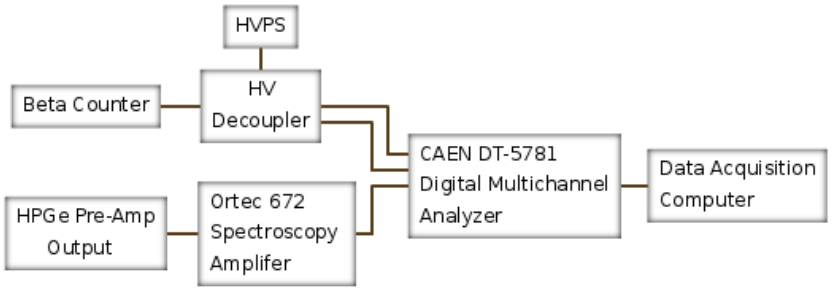

Figure 4.9: Modules used to collect list mode data using CAEN DT-5781 digital MCA.

the middle of the project, only a portion of the data acquisition and analysis were performed with this system.

4.3 Characterization

4.3.1 Operating Potential

When operating a gas detector in the Proportional region, the counting rate should remain constant with minor changes in applied potential. Historically, the optimum settings for applied voltage and discriminator settings for a system such as shown in Fig. 4.7 have either set a constant applied voltage and varied the discriminator threshold in steps, or set a constant discriminator level and varied applied voltage in steps while measuring a long-lived source [57]. Both of these tests were performed using the analog system. At lower potentials, the field strength is insufficient to separate all of the ion pairs formed, and some beta events are not counted due to recombination. Additionally, small signals generated by low energy beta particles that produce fewer ion pairs may not exceed the discrimination threshold due to insufficient charge multiplication. With increased potential, all electrons that enter the gas are collected, no additional counts are recorded with increasing potential, resulting in a plateau. As potential is further increased, additional counts are recorded due to spurious pulses and multiple pulsing - a phenomenon in which the positive ions created during the initial event gain sufficient kinetic energy to liberate electrons when striking the cathode surface [8]. As can be seen in Fig. 4.10, a lower fixed threshold produces a counting curve with a more broad plateau, but sufficient applied potential causes enough charge multiplication, resulting in very nearly the same count rate.

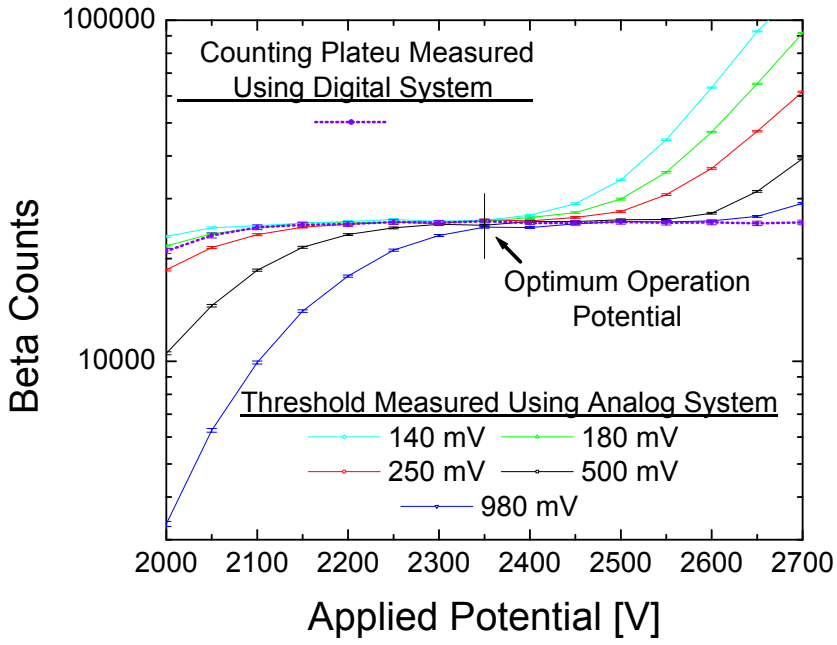

Figure 4.10: Counting plateau measured for varying applied voltage using different discrimination threshold values with analog system and measured using the digital system to integrate the β spectrum above the noise level.

This approach is still being used today [58] for measurements in which β spectral data is neither required, nor collected. Although 4π proportional counters are also used for low energy x-ray spectroscopy, the detectors used are operated under different conditions, using high-pressure P-10 gas, and the process of selecting the detector bias is not as critical for those measurements [59]. Varying applied potential in steps, the number of counts in β spectra above noise can be integrated. This improves the ability to distinguish between an increase in events due to collection of additional true β particles and the inclusion of noise. Although there is no reason that precludes applying this method with analog electronics, it was not conceived until after the digital system was in place. Measured β spectra for two different anode potentials are shown in Fig. 4.11 to illustrate the process. As applied potential is raised, the gas multiplication in the counter increases dramatically. The distinction between noise or spurious pulses and true β counts is defined by the channel minimum occurs in the spectrum for each case. Although the applied potential differs by 300V for these two spectra, the integration above the noise agree to within the uncertainty based on counting statistics of 0.5%. The counting plateau derived using this method is also plotted in Fig. 4.10. Below 2150 V applied potential, some low-energy β particles are not counted, but above that level, the detector response is extremely consistent until the applied potential is well above 3000 V where significant amounts of spurious pulses are generated.

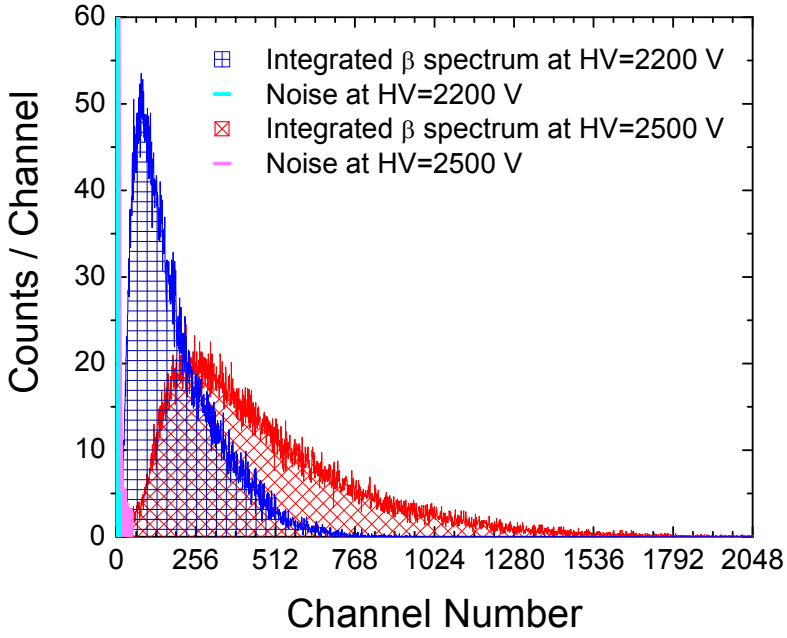

Figure 4.11: Comparison of measured β spectra of a ^{95}Zr metal foil with different potentials applied to the β counter. The solid regions on the left represent noise or spurious pulses. The pattern filled areas for the two curves, representing true β counts agree to within the uncertainty based on counting statistics.

Based on the data shown, a potential of 2350 V was selected in order to operate near the center of the plateau which provides stability against any drift in the output of the high voltage power supply and maximizes the beta counting efficiency.

4.3.2 Energy Calibration

Beta counters of this design are often assumed to be 100% efficient for detection of particles that enter the gas [54, 57] because the energy spectra of many isotopes contain very few low-energy particles. For the isotopes in this study, however, it is critical to understand the threshold to make corrections for the low-energy region of the spectrum.

To perform an energy calibration, ^{55}Fe was used, which decays by electron capture. Sealed sources of ^{55}Fe will emit x rays shown in Table 4.1. Even sources with very thin mylar windows would stop the Auger electrons, so a bare source was desired that would allow these electrons to enter into the detector gas and be measured. A small copper slide was prepared with a recessed well as shown in Fig. 4.12. A solution of ^{55}Fe in 1M HCl was deposited onto the slide and then baked to evaporate the liquid. The slide was placed on top of the aluminum source holder and inserted into the beta counter. Counting was performed

using both digital and analog electronics, with the resulting spectra shown in Fig. 4.13. The shape of the electron energy spectrum was nearly identical for each signal processing pathway, but the electronic noise from in the analog system obscured the L-shell Auger electrons. With the digital signal processing, the L-shell electrons were clearly observed, allowing for a two point energy calibration, and determination of an energy threshold of 0.35 keV.

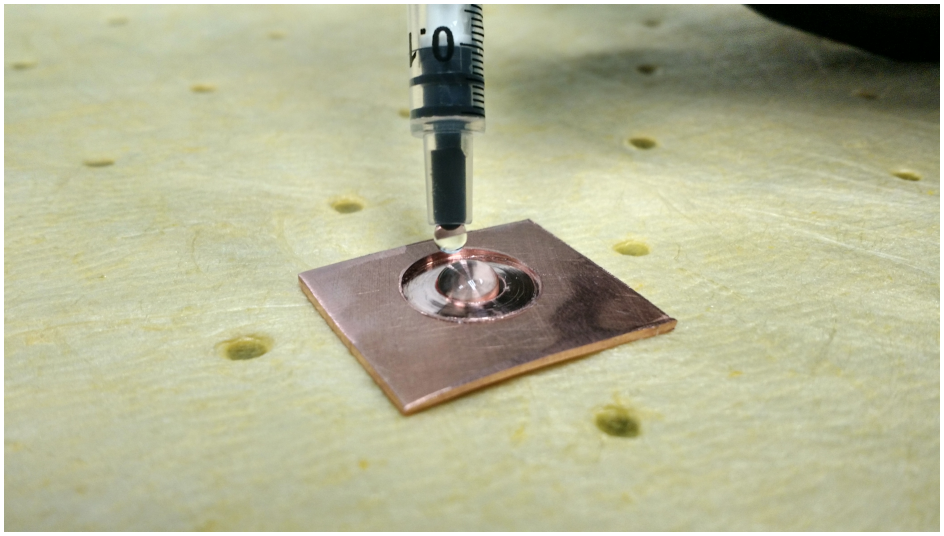

Figure 4.12: Deposition of ^{55}Fe solution onto copper slide.

Table 4.1: Decay data for ^{55}Fe [5]

Radiation	Energy [keV]	Intensity [%]
Auger e^- L	0.61	139.9
Auger e^- K	5.19	60.1
X-ray L	0.64	0.66
X-ray Kα2	5.888	8.2
X-ray Kα1	5.899	16.2
X-ray Kβ2	6.49	1.89
X-ray Kβ3	6.49	0.96
γ-ray	126.0	1.28E-007

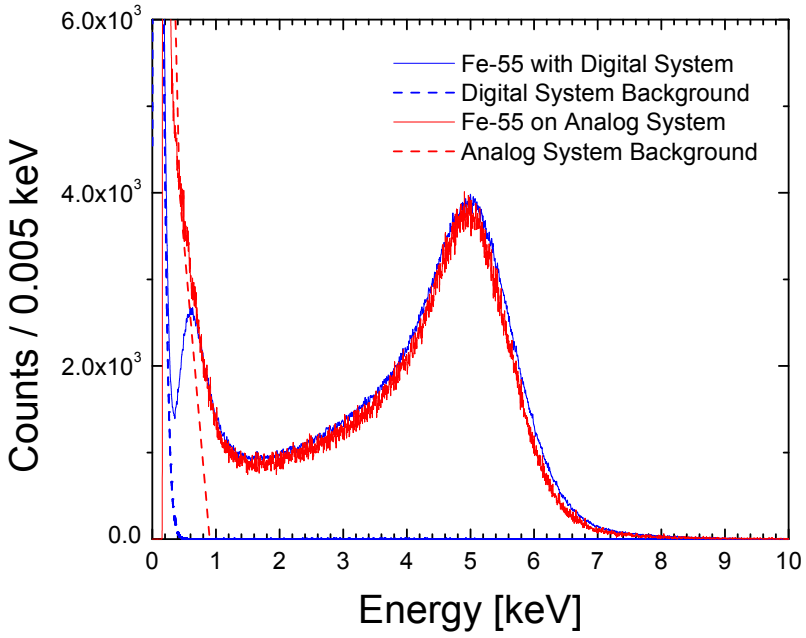

Figure 4.13: Beta spectra of ^{55}Fe source for energy calibration obtained using analog and digital systems.

4.3.3 Air Exchange During Sample Insertion

Gas multiplication within the β counter is greatly affected by the presence of oxygen, which can bind with ions, effectively reducing the gain. When a sample is changed, one aluminum holder is removed and another one is inserted, allowing some methane to escape

and air to enter the gas chamber volume. Since the detector is under continuous methane flow, the oxygen will gradually be expelled and the gas gain will recover. A test was conducted to measure the time response of this process. Fig. 4.14 shows the results of this test. After 10 minutes, the integrated count rate above the noise level stops increasing and exhibits only statistical fluctuations. The gas gain is essentially recovered 15 minutes after the source insertion.

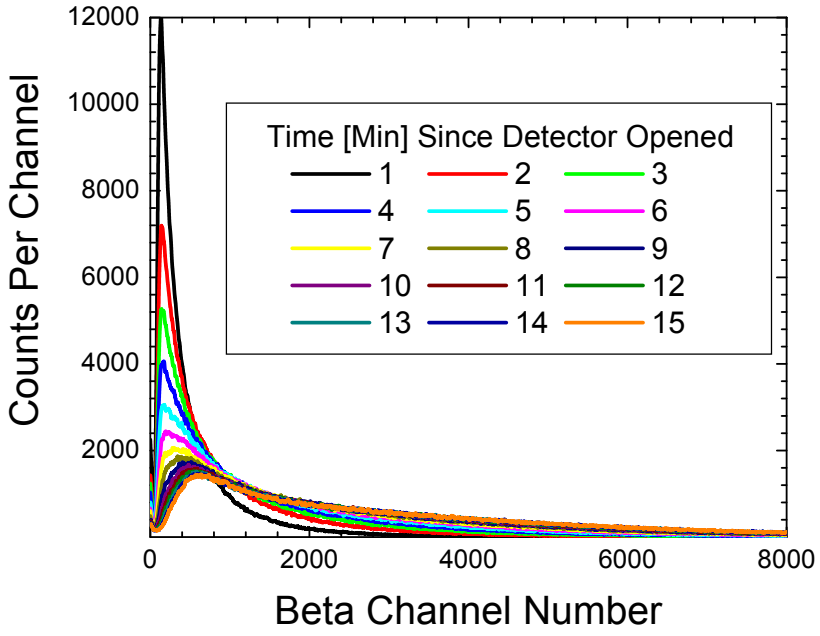

Figure 4.14: Beta spectra recorded in 1 minute intervals following a ^{147}Nd sample change in which the detector was unsealed for one minute.

4.3.4 Coincidence Between Beta Counter and HPGe Detectors

Coincidence measurements were performed using both analog and digital systems described in Section 4.2.4. In addition to true coincidences between the two detectors, any measurement will include accidental coincidences that must be subtracted. More sophisticated analysis is possible with list mode data provided by the digital system. Signals typically form more quickly in the β counter than in the HPGe. Fig. 4.15 shows the difference in time between the two signals recorded for a neodymium foil sample with a β count rate of 17 kHz. Accidental β-γ coincidence is subtracted from true coincidence by subtracting the γ spectrum associated with the area highlighted in red from the γ spectrum associated with the area in black.

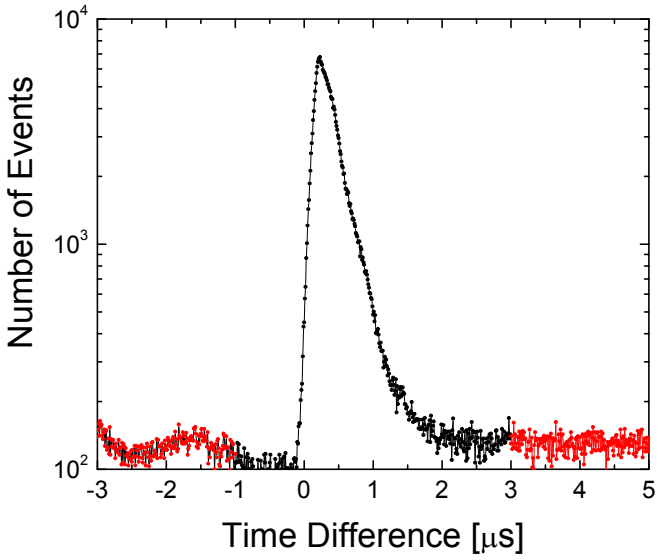

Figure 4.15: Time difference recorded between β and γ signals for neodymium metal foil sample. Positive time difference indicates the β signal arrived first. Points in red indicate the baseline accidental coincidence rate that is used for subtraction.

4.3.5 Background

Detector background measurements were performed using an aluminum holder with no sample as a blank over a period of 60 hours. The β-γ coincidence, shown in Fig. 4.16a, reveals low rates of coincidence, with 120 counts in the 511-keV annihilation peak and 20 counts in the 1460-keV peak of ^{40}K over the counting period of 60 hours. The background for the β counter, shown in Fig. 4.16b, has a rate of 0.8 $\frac{counts}{sec}$ integrated above the electronic noise threshold.

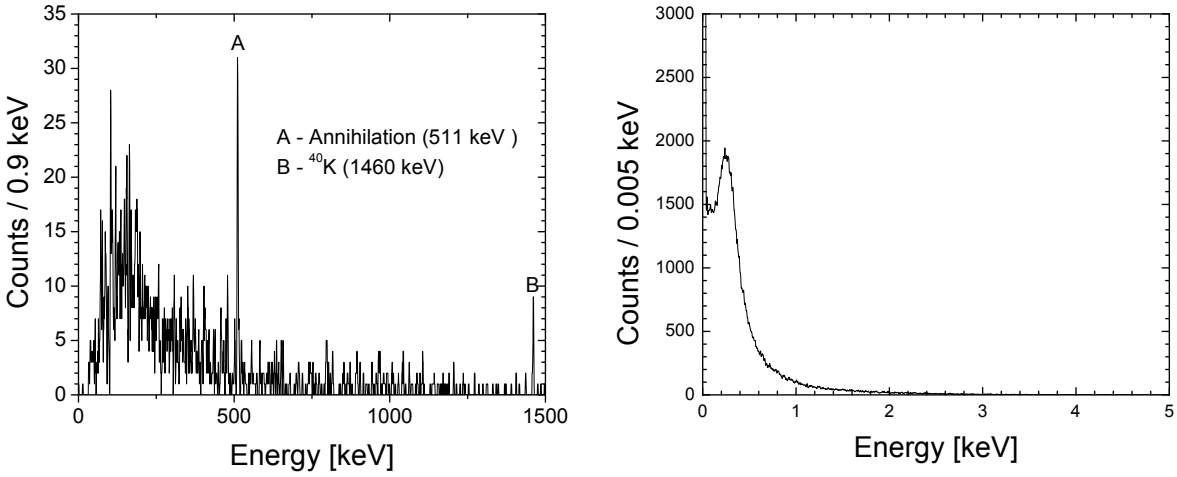

(a) (b)

Figure 4.16: Background recorded over 60 hours. (a) shows β-γ coincidence and (b) shows β singles counts.

4.4 Simulations

GEANT4 (GEometry ANd Tracking) is a physics toolkit for the simulation of the passage of particles through matter [60]. As a collaborator on this project, fellow graduate student A.M. Hennessy from UC Irvine, performed simulations of the detector. A rendering of the simulation is shown in Fig. 4.17, which includes the aluminum target frame surrounded by the cylindrical methane gas chambers housed in copper and aluminum with conducting aluminized Mylar windows which allow minimal attenuation of radiation leaving the detector. There are recessed volumes in each gas chamber which hold insulators that seal the detector and allow for the entrance and exit of the anode wires. Simulations were used to determine the energy deposited within the gas volumes in order to predict effects of β attenuation in the foils, detector threshold, and cross-talk between the two halves of the chamber.

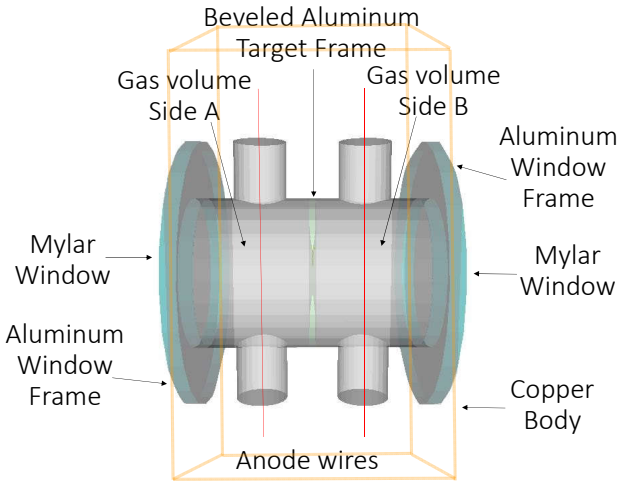

Figure 4.17: Rendering of the GEANT4 simulation for the beta counter. Shown is the interior gas volume with aluminum source holder in the center. The main body is composed of copper, with Mylar windows held in place by aluminum frames on the exterior surface.

Chapter 5

Fission Product Branching Ratio Measurements

Fission product branching ratios were determined using the beta counter to measure β particles and an HPGe detector to measure the γ rays. Coincidence techniques were used to gate on specific γ-ray lines and the number of β particles detected during these time windows were used as an indicator of the number decays. This chapter describes the measurement of γ-ray branching rations of ^{95}Zr and ^{147}Nd. The first experiments used metal foils irradiated in a reactor to produce these isotopes to investigate the performance of the detector and go through the measurement process. These reactor-produced samples are subject to impurities and self attenuation of low-energy β particles, which require corrections. The final experiment used pure samples of fission products implanted on ultra-thin carbon foils which minimized the corrections for background and self attenuation and allow high precision measurements to be made.

5.1 Activated Zr Metal Foils

^{95}Zr was selected as the first fission product to measure using the beta counter because it has two strong γ-ray lines with branching ratios that are well known. The activity can be determined using only γ-ray spectral analysis, and the measurements were used to validate the viability of the technique and make comparisons to GEANT4 simulations of the detector.

5.1.1 ^{95}Zr Decay Characteristics

^{95}Zr is a β emitter with an endpoint energy of 1123.6 keV, but the vast majority of the β particles have less than 400 keV [5]. The decay scheme is shown in Fig. 5.1. A Monte Carlo β decay code described in Ref. [61] was used to determine the beta spectrum shape. Inputs to the code include parent and daughter nucleus rest masses (to determine decay energies), the energy level of the nuclear excited state of the daughter, and the Fermi function. The Fermi function is used to apply corrections for Coulombic interactions between the emitted

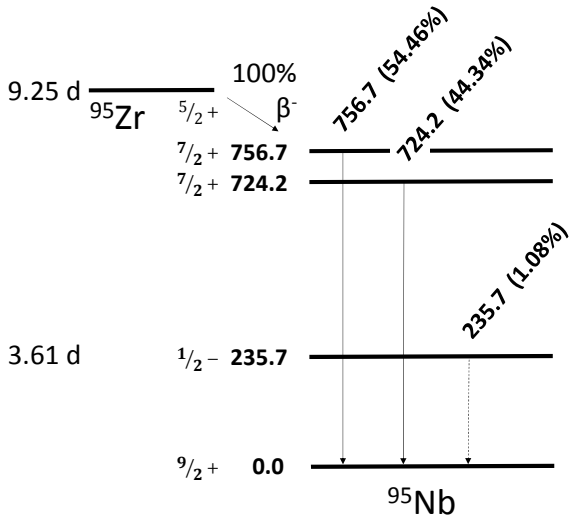

Figure 5.1: Decay scheme for ^{95}Zr [5].

β particle and the daughter nucleus, and corrections for a number of other smaller-order effects are applied. This code has been used in a number of previous β decay studies and has been thoroughly vetted.

For nuclei with high atomic number and low Q values, the large Coulomb-field effect on low-energy β particles results in an energy distribution weighted heavily towards low-energy β particles. For this reason, cubic spline interpolation for the several-keV spacing between the tabulated Fermi function values [62] caused erratic distribution results in the important energy region from 0-5 keV, so an analytical non-relativistic approximation [63] given by

$$F(Z,T) \approx \frac{2\pi\eta}{1-e^{-2\pi\eta}} \ , \tag{5.1}$$

where η is the momentum of the β particles in units of $\mathrm{m}_o c^2$, was used to better interpolate the values. Since this approximation is loses accuracy as the β paricles approach relativistic energy [64], and tabulated values for higher energy were sufficiently interpolated with the cubic spline, it was only used below 20 keV. The variable, η, which is inversely proportional to the square root of the particle's energy, was adjusted until the function matched the tabulated values.

One source of activity that is unavoidable in any source of ^{95}Zr is the radioactive daughter, ^{95}Nb, which will grow and eventually reach transient equilibrium. The activity of ^{95}Nb can be calculated by the equation

$$A_{Nb}(t) = A_{Zr0}\frac{\lambda_{Nb}}{\lambda_{Nb}-\lambda_{Zr}}\left(e^{-\lambda_{Zr}t} - e^{-\lambda_{Nb}t}\right) \ , \tag{5.2}$$

where $A_{Nb}(t)$ is the ^{95}Nb activity at some time, t, after a pure source of ^{95}Zr, of activity, A_{Zr0} is created; and λ_{Zr} and λ_{Nb} are their respective decay constants. The result of this calculation

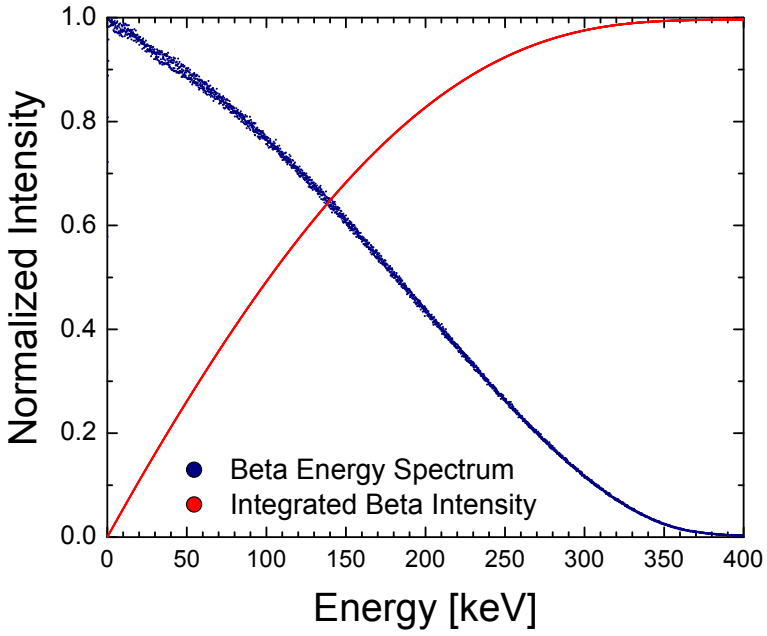

Figure 5.2: Spectral shape for ^{95}Zr. Less that 1% of the β spectrum extends to energies above 400 keV.

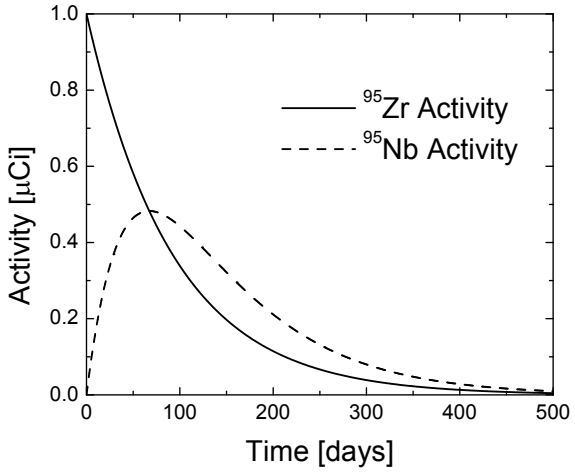

Figure 5.3: Transient equilibrium of ^{95}Nb assuming an initially pure parent of ^{95}Zr with 1 μCi activity.

is shown in Fig. 5.3. ^{95}Nb emits a 766-keV γ with a branching ratio of 0.99808(7), so its activity can be determined from the measured γ-ray spectrum in order to apply corrections.

5.1.2 Preparation of the Samples

Thin foils of natural zirconium with thickness of 1, 2, 2.5, and 3 μm were obtained with a quoted uncertainty of $\pm$ 25% thickness from the supplier. Using a machinists' punch, the foil sheets were punched to $\frac{3}{8}$ inch diameter. Since the foils were so thin, they were sandwiched between to pieces of ordinary printer paper in order to prevent binding in the punch. Based on previous experience (see Section 2.1.1 and Section 3.2.1), it was expected that the foils may be slightly thicker than those quoted by the manufacturer. Because of the extremely low mass-density thickness of the foils in this experiment, γ-ray attenuation would be negligible and the small masses of the foils were not possible to measure with good accuracy using the balance on hand, which had a precision of 0.1 mg. Precise determination of each foil thickness was important to determine the self attenuation of low-energy β particles. For this experiment, foil thicknesses were determined using a spectroscopy grade ^{241}Am α source to measure attenuation through the foils.

The ^{241}Am was placed on the bottom shelf of an Ortec SOLOIST^{TM} alpha spectrometer. A second shelf, fabricated from aluminum with a 3-mm aperture drilled in the center to act as a collimator was placed near the top of the sample chamber. An aluminum ring was placed on top of the foil, but not covering the aperture, to flatten the foil in order to ensure alpha particles passed through as close to normal as possible. The top of the chamber is fitted with a ion-implanted-silicon charged-particle detector, which uses a thin silicon wafer with an extremely thin layer of boron ($\sim$500 Å) implanted on the surface. A schematic diagram of the

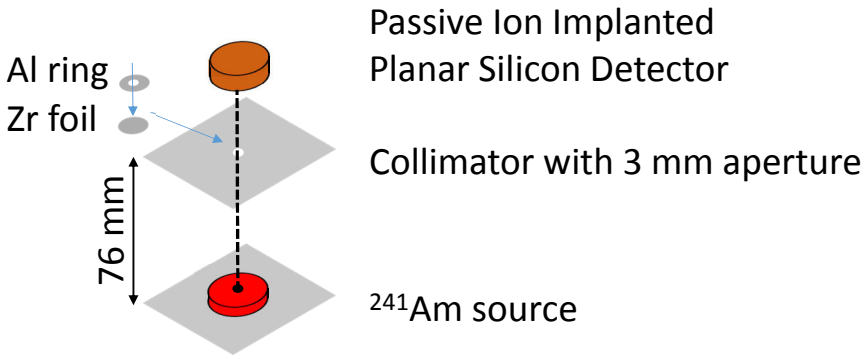

Figure 5.4: Geometry for α particle attenuation measurements used to determine thickness of zirconium foils.

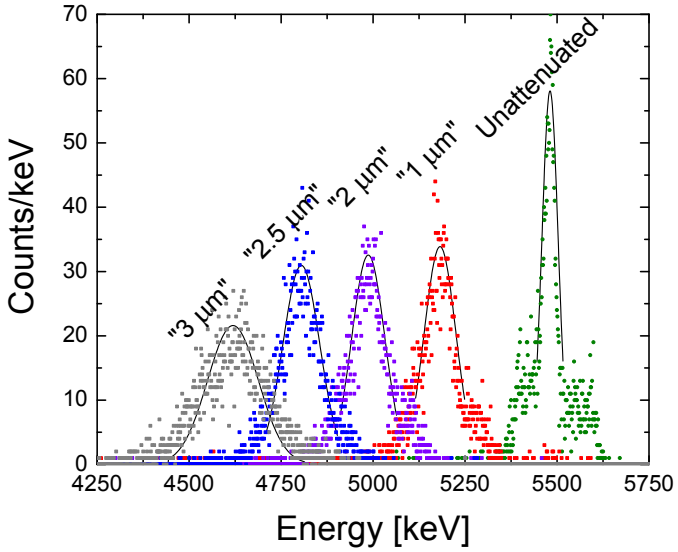

Figure 5.5: Alpha-particle energy spectra of collimated ^{241}Am source used to determine thickness of zirconium foils.

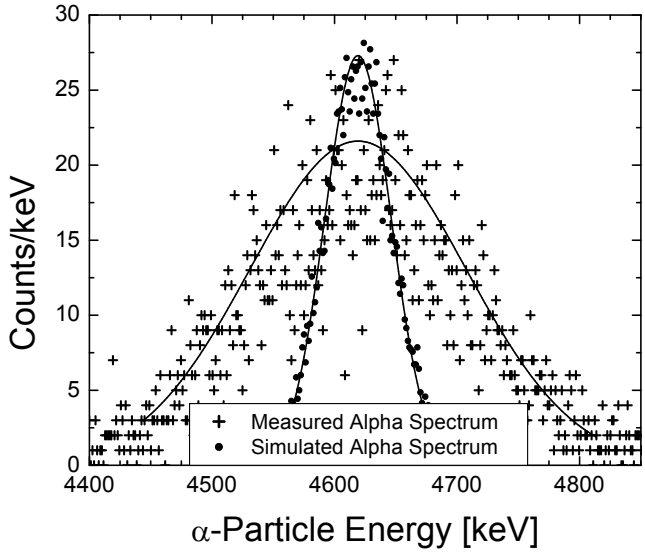

Figure 5.6: Comparison between measured α energy spectrum and Monte Carlo simulation for ^{241}Am α particles passing through a 3.71-μm-thick zirconium foil.

geometry is shown in Fig. 5.4. The chamber was connected to a vacuum pump to minimize attenuation of α particles in air. The detector was energy calibrated using the built-in pulser. The signals were processed using an Ortec EASY-MCA-2K$^{\text{TM}}$ and histograms were acquired with Maestro software. Two-hour counts were performed with each foil and with no foil, and the energy spectra were fitted with Gaussians, as shown in Fig. 5.4. The energy loss in the foil was determined by the change in location of the energy peak with and without the foil attenuator. The peaks were quite broad, in part due to the statistical fluctuations in alpha energy loss, and in part due to detector resolution [8]. Additional variation also may indicate non-uniform foil thickness. For purposes of uncertainty estimation, it was assumed that the peak could be located within 20% of the full width at half maximum (FWHM) energy. The alpha energy loss was simulated using the Monte Carlo code Transport of Ions in Matter (TRIM) [45] for ^{4}He nuclei with energy of 5481 keV. Zirconium foil thickness was varied in the simulation until the energy peak matched the experimental result. Because the simulation did not account for detector response, the fitted Gaussian displayed a more narrow FWHM as shown in Fig. 5.6. Results are summarized in Table 5.1. Each foil was slightly thicker than the specified thickness, but within the manufacturer's stated uncertainty. These more precise foil dimensions were used in subsequent GEANT4 simulations discussed in Section 5.1.5.

Table 5.1: Alpha attenuation data used for determination of zirconium foil thicknesses.

Nominal Thickness [μm]	Mean Energy [keV]	FWHM of Collected Spectrum [keV]	FWHM of Monte Carlo [keV]	Energy Loss [keV]	Foil Thickness [μm]
0	5481	33	7		
1	5183	95	22	298	1.31 $\pm$ 0.08
2	4979	90	30	502	2.20 $\pm$ 0.08
2.5	4794	106	58	687	2.98 $\pm$ 0.09
3	4619	221	66	862	3.71 $\pm$ 0.19

5.1.3 Neutron Activation

The manufacturer only provided a typical purity analysis, but stated that each batch may differ significantly from this analysis. Each isotope was investigated to predict if any long-lived isotopes would produced which would interfere with the measurements following neutron activation. Of those listed in Table 5.2, only ^{180}Hf(n,γ)^{181}Hf was determined to be problematic. Hafnium is typically present in zirconium metal because it is difficult to chemically separate from zirconium. ^{180}Hf has very large low-lying neutron capture resonances, allowing even small impurities to result in significant activity. ^{181}Hf decays by β-particle emission with a similar half-life (42 d) to ^{95}Zr (64 d). It does, however, have a number of strong γ-ray lines with well known intensities, which allow for corrections to be calculated and applied.

Neutron activation was performed by A.M. Hennessy at the University of California at Irvine. Foils were irradiated using the 250 kW Training, Research, Isotopes, General Atomics (TRIGA) reactor with a thermal neutron flux of approximately $8{\cdot}10^{11}$ $\frac{n}{cm^2 \cdot s}$. Each sample was placed in the bottom of a small plastic vial and then filled with cotton to prevent shifting. Vials were loaded into TRIGA irradiation tubes which were then placed in a rotary specimen rack. This rack rotates the samples during the irradiation to negate effects of minor non-uniformities in the neutron flux. Total irradiation time was 24 hours, after which the reactor was shut down and the vials remained in place for several days to allow short-lived activity to decay prior to handling and preparation for shipping to UC Berkeley.

5.1.4 Measurement of Activated Foils

Tungsten wires with a diameter of 12.7 μm were taped on to each half of one of the aluminum source holders to form a grid which could retain the circular foils in the center aperture, but only block $\sim$0.5% of the surface area. The foils were each measured in the beta counter with the Mylar window perpendicular to the HPGe end-cap. Data were recorded for β-singles spectra, γ-singles spectra, and β-γ coincidences using analog electronics.

The HPGe was calibrated for photopeak efficiency at a distance of 20 cm outside of the

Table 5.2: Purity analysis for zirconium foils used in neutron activation.

Element	Impurity [ppm]	Natural Isotopic Abundance					
Zirconium	Matrix	^{90}Zr	^{91}Zr	^{92}Zr	Zr^{94}	^{96}Zr	
Abundance [%]		51.45	11.22	17.15	17.38	2.8	
Carbon	250	^{12}C	^{13}C				
Abundance [%]		98.93	1.07				
Chromium	200	^{50}Cr	^{52}Cr	^{53}Cr	^{54}Cr		
Abundance [%]		4.345	83.798	9.501	2.365		
Hafnium	2500	^{174}Hf	^{176}Hf	^{177}Hf	^{178}Hf	^{179}Hf	^{180}Hf
Abundance [%]		0.16	5.26	18.6	27.28	13.62	35.08
Hydrogen	10	^{1}H	^{2}H				
Abundance [%]		99.9885	0.0115				
Iron	200	^{54}Fe	^{56}Fe	^{57}Fe	^{58}Fe		
Abundance [%]		5.845	91.754	2.119	0.282		
Nitrogen	100	^{14}N	^{15}N				
Abundance [%]		99.632	0.368				
Oxygen	1000	^{16}O	^{17}O	^{18}O			
Abundance [%]		99.757	0.038	0.205			

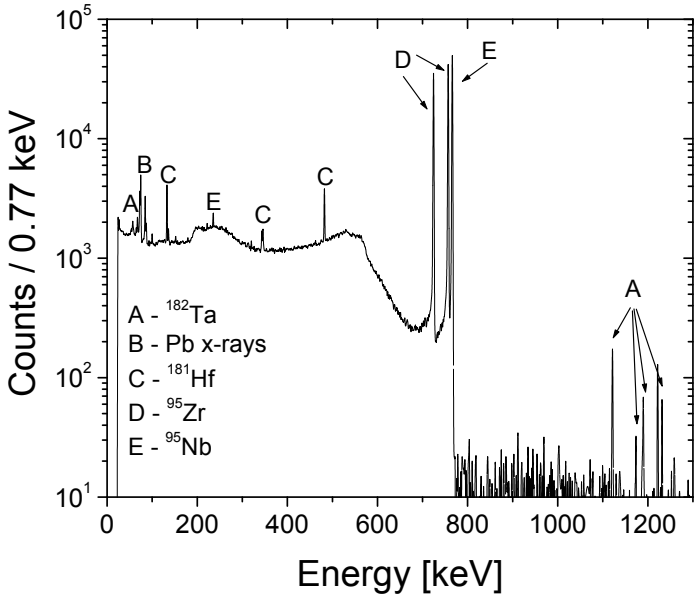

Figure 5.7: Energy spectrum of irradiated zirconium foil measured with coaxial high purity germanium detector.

Table 5.3: Neutron capture cross-sections for zirconium foil with hafnium and tantalum impurities [10].

Energy	^{94}Zr σ_c[mb]	^{180}Hf σ_c[mb]	^{180}Hf/^{94}Zr σ_c ratio	^{181}Ta σ_c[mb]	^{181}Ta/^{94}Zr σ_c ratio
Thermal	49.8	13000	261	20670	415
Resonance Integral	321	34000	105.9	660000	2056
Fission Spectrum	12.34	32.5	2.6	85.66	69

β counter as described in Section 2.1.2. The zirconium foils were thin enough that γ-ray self-attenuation was negligible, but due to the large amount of low-energy β-particles in the distribution, β losses could not be neglected. This was measured experimentally by comparing γ-singles spectra while inside the β counter, and γ-ray spectra coincident with β using the setup described in Section 4.2.4.

5.1.5 Results and Discussion

A γ-singles spectrum is shown in Fig. 5.7. 575 Bq of ^{95}Zr was produced. ^{181}Hf was found to be a minor contaminant in each of the samples. Based on values shown in Table. 5.3, ^{180}Hf has a thermal neutron capture cross section which is 261 times higher than that of ^{94}Zr. Taking into account natural abundances, this would have resulted in a ^{181}Hf activity approximately 4 times greater than the ^{95}Zr which we wanted to study. The actual ^{181}Hf activity measured in these samples was much smaller than predicted. Two possible effects are considered here. The most significant is that, fortunately, the actual hafnium content was much, much lower than that provided in the "typical" analysis from the vendor. The second effect is that the resonances in the thermal neutron capture cross section for ^{180}Hf are at very low energies. The reactor operator stated that the neutrons should be largely thermal at the point of activation, but neutron energy spectrum in the reactor was not measured. Any shift in the distribution towards higher-energy neutrons would provide a benefit in the activity ratio. ^{181}Hf activity in each of the foils was measured in the range of 1.2(1)-2.2(1)% relative to the activity of ^{95}Zr.

The only other long lived contaminant measured in the sample was 9(2) Bq of ^{182}Ta in each of the foils. Tantalum is used is some of the chemistry and mechanical processes during the production of the foils. Uncertainties in the determination of this activity were larger due to statistics because the branching ratios were smaller, the lower energy peaks were in on top of a high Compton continuum, and the HPGe efficiency was small for the higher-energy peaks. Tantalum was not listed in Table 5.2. Although the cross-sections for neutron capture are very large, the amount of the impurity based on the measured activity was quite small.

For the purposes of measuring the total activity of the sample, only the total number

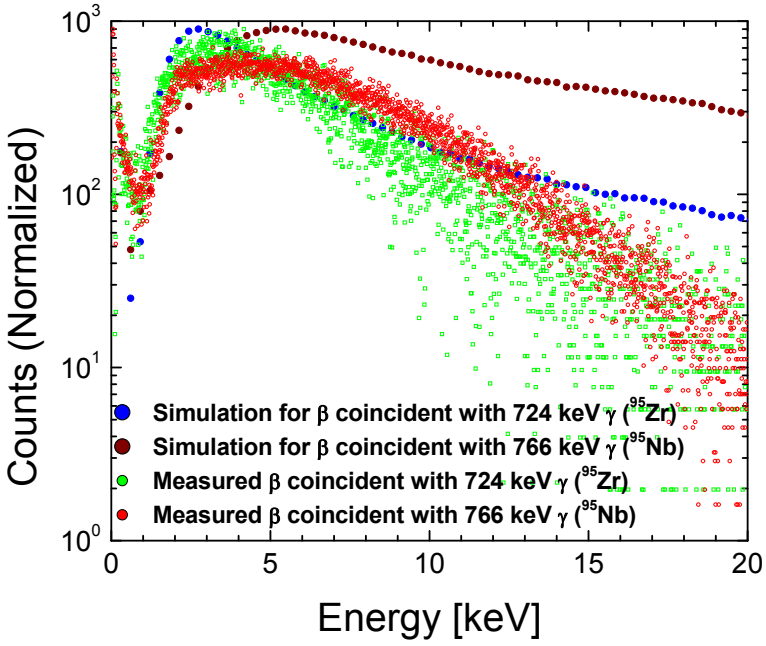

Figure 5.8: β energy deposited in detector coincident with γ lines from ^{95}Zr and ^{95}Nb. Scatter in measured values at high energies is a function of counting statistics.

of beta counts is required, and the measured energy spectrum is not relevant. The vast majority of the β particles will not be stopped in the gas, such that only a small fraction of the total energy is recorded in the measured spectra. The energy deposited reflects a minimum ionizing peak, which is predicted to be significantly different for ^{95}Zr as compared ^{95}Nb. The stopping power decreases as β energy increases, so the energy deposited by lower energy β particles will actually be greater than for higher energy β particles. Data was collected for β particles coincident with the 724 keV γ-ray of ^{95}Zr, with a β endpoint energy of 399 keV and the 766 keV γ-ray of ^{95}Nb with a β endpoint energy of 160 keV [5]. A comparison between the GEANT4 simulation and measurement for β energy deposited in the detector associated with each of these transitions is shown in Fig. 5.8. The GEANT4 simulation does not take detector resolution into account. As can be seen, the resolution of the β counter is so poor that it is difficult to distinguish the two spectra, but it does appear that the spectrum associated with the lower-energy beta has a peak at a slightly higher energy and is somewhat more broad, which matches expectations based on stopping power theory and simulation.

The β efficiency, which included the detector threshold effects was dominated by the losses within the foil itself. It could be determined from the data for a β spectrum associated with

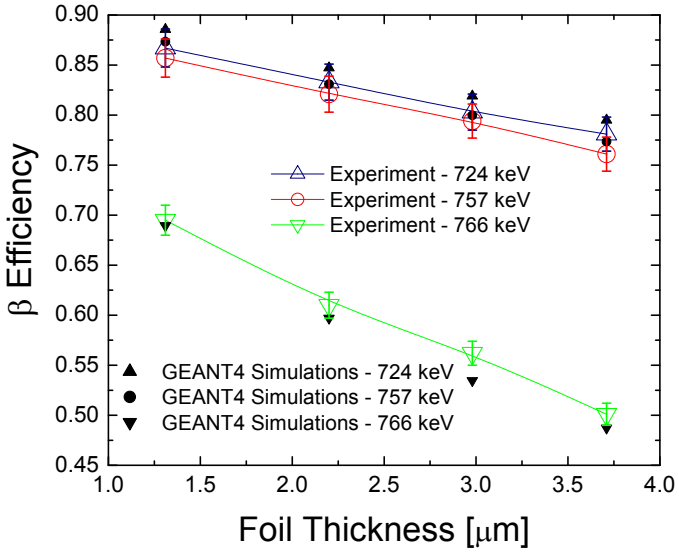

Figure 5.9: Comparison between measured β efficiency and Monte Carlo simulation with zirconium foil.

a particular transition using the equation,

$$\varepsilon_{\beta_\gamma} = \frac{N_{\beta\gamma}}{N_\gamma} \,, \tag{5.3}$$

where $N_{\beta\gamma}$ is the number of net counts in the γ-ray peak of interest when gated on the β signal, N_γ is the number of net counts in the γ-singles measurement. Using this method, the γ-ray branching ratio and photopeak efficiency cancels, so it was not necessary to measure the photopeak efficiency of the HPGe for the source inside the β counter. Three γ-ray lines of interest were studied: the 724 and 757-keV γ rays from decay of ^{95}Zr and the 766-keV γ from the decay of the daughter product, ^{95}Nb. The 766-keV γ-ray line is of interest because the β endpoint energy is lower by more than a factor of 3, so the β efficiency in this context is expected to be much smaller. Figure 5.9 shows the comparison between the experimental results and the GEANT 4 simulations. Uncertainty in the measured values were propagated from the uncertainty in the photopeak measurements. The results provide confidence in the reliability of the simulations.

The activity of each of the impurities were determined using multiple γ-ray lines from the measured spectrum. The contribution of these impurities and ^{95}Nb were subtracted from the total β counts to determine the number of counts associated with the decay of ^{95}Zr using

$$N_{\beta_{net}} = N_\beta - A_{Nb}\varepsilon_\beta^{Nb}t - A_{Hf}\varepsilon_\beta^{Hf}t - A_{Ta}\varepsilon_\beta^{Ta}t - room\ background \,, \tag{5.4}$$

where N_β is the total number of β counts; and A_X and ε_β^X are the activity and β efficiency for

Table 5.4: Measured γ-branching ratios for ^{95}Zr [5].

γ	Measured I_γ	NNDC I_γ
724	0.444(16)	0.4427(22)
757	0.547(19)	0.5438(22)

Table 5.5: Factors affecting uncertainty in measured γ-branching ratios for ^{95}Zr.

Components of Uncertainty	
0.8%	N_γ
0.3%	N_β
2.0%	ε_γ
2.2%	ε_β^{Zr}
1.4%	Correction for ^{95}Nb
0.2%	Correction for impurities
3.4%	Total

impurity, X, and t is the total count time. The β efficiency for ^{95}Nb used in this calculation is based on measurements using Eq. 5.3. ^{181}Hf and ^{182}Ta decay with similar average β energies, so their β detection efficiencies were assumed to be within 10% of that associated with the 724 keV γ of ^{95}Zr.

The ^{95}Zr γ-ray branching ratios were determined using β-singles and γ-singles information and the relationship

$$I_\gamma = \frac{N_\gamma}{\varepsilon_\gamma} \frac{\varepsilon_\beta^{Zr}}{N_{\beta_{net}}} \,, \tag{5.5}$$

where I_γ, N_γ, and ε_γ are the branching ratio, net peak counts and photopeak efficiency for the γ-ray of interest; ε_β^{Zr} is the β efficiency for ^{95}Zr, and $N_{\beta_{net}}$ is the number of β counts attributed to the decay of ^{95}Zr. Results for γ-ray branching ratios are shown in Table 5.4, with uncertainty propagated using Equation 5.5. Factors affecting the uncertainty in the determination of the brancing ratios are shown in Table 5.5. The most significant effects on the uncertainty came from the β detection efficiency due to the thickness of the foils, and the HPGe calibration which is reflected in ε_γ as well as the determination of other activities in the sample. Detector simulation and data, including attenuation in the foils, compare well. To improve on this, thinner samples and more precise HPGe calibrations are required.

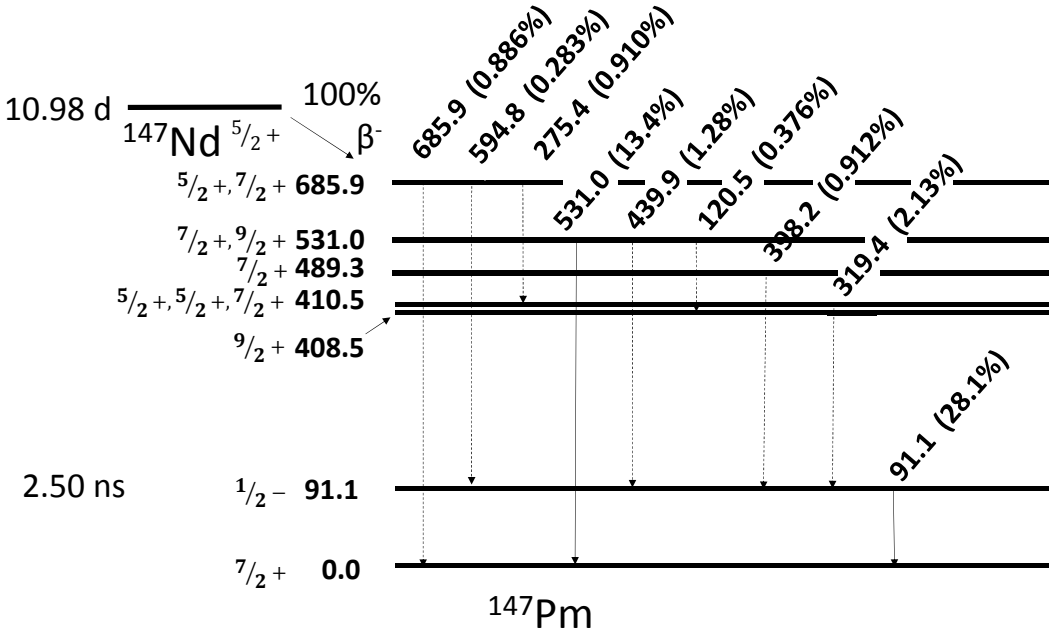

Figure 5.10: Decay scheme for ^{147}Nd. For simplicity, only γ transitions with intensity greater than 0.25% are shown [9].

5.2 Activated Nd Metal Foil

The second fission product studied was ^{147}Nd, and the first isotope for which an experimental branching ratio could be expected to improve on known nuclear data. There is some debate regarding the current value and precision of this branching ratio. Several published papers report on the branching ratios. A 1995 paper [65] reports a branching relative branching ratio uncertainty of 2.2%, but it appears that these are relative, not absolute intensity. A 1997 paper [66] reports the branching ratio's relative uncertainty as 0.8%. For a period of time, this was taken by data evaluators as an absolute measurement. While common to normalize branching ratio results to the largest value, what it not immediately apparent is that it appears that the 0.8% uncertainty is actually a measure of the uncertainty in the decay scheme normalization itself. The Nuclear Data Sheets, published in 2009, evaluates the relative uncertainty in the 531 keV branching ratio at 8%, and literature search revealed no new publications on this branching ratio between that time and present. The National Nuclear Data Center (NNDC) [5] at the time of this writing shows a 531 keV branching ratio of 0.134(3), or 2.2% relative uncertainty, but unlike the Nuclear Data Sheets publications, the NNDC site does not generally show references on which those values are based on, and this value has changed several times in the past 5 years.

5.2.1 ^{147}Nd Decay Characteristics

^{147}Nd is a β emitter with an endpoint energy of 896.0 keV and a decay scheme as shown in Fig. 5.10. A number of transitions from excited states of ^{147}Pm have large internal conversion ratios so that instead of a γ ray, a conversion electron and possibly one or more Auger electrons are emitted in coincidence with the single β particle. The 2.50 ns half-life of the 91.1 keV state is also small compared to the time response of the β counter, so for the purposes of these measurements this transition is considered to be in coincidence with the ^{147}Nd decay. The timescale of these events is very short compared to hundreds of nanoseconds during which signals develop in the β counter, such that energy deposited from any of these electrons in one half of the β counter will be recorded as a single event. The emitted β and subsequent conversion electrons have very little angular dependence [67], so there is a significant probability of coincidence between the two sides of the detector from a single β decay.

The β spectrum was calculated using the methods described in Section 5.1.1 and plotted in Fig. 5.11. The shape of the β spectrum is similar to that of ^{95}Zr in that it is has a significant population at very low energies and the measurement is therefore also highly sensitive to detection threshold. The two most significant β branching ratios result in some departure from a smooth curve, and problems with the approximation of the Fermi Function cause some irregular features below 5 keV. These have been minimized to the extent that the remaining effects from the the interpretation of these measurement are quite small.

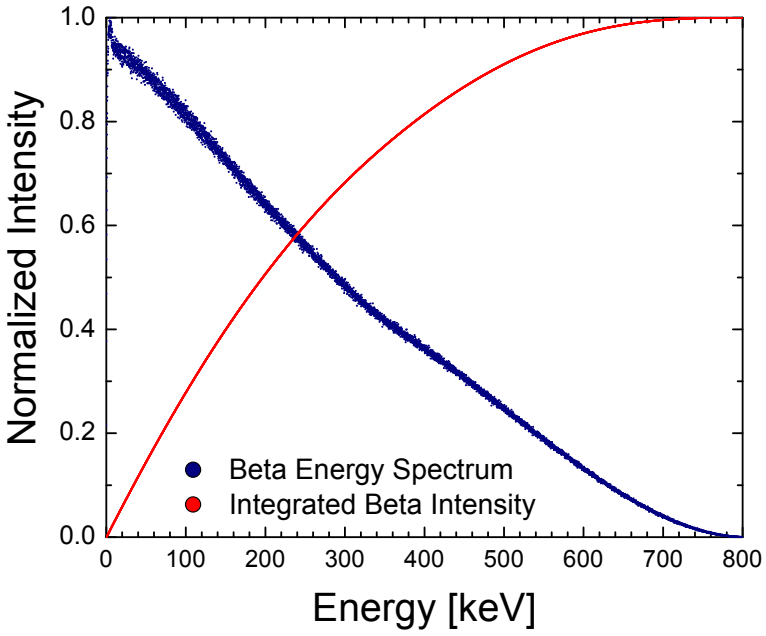

Figure 5.11: Spectral shape for ^{147}Nd.

Table 5.6: Purity analysis for neodymium foil used in neutron activation.

Neodymium Isotopes		Spectrographic Analysis			
Isotope	Percent	Element : ppm	Element : ppm	Element : ppm	Element : ppm
142	0.42	Ag : <100	Cu : <100	Mg : <100	Sm : <500
143	0.29	Al : <500	Dy : <1000	Mn : <200	Ta : <500
144	0.68	B : <100	Er : <50	Mo : <200	Tb : <500
145	0.64	Ba : <100	Eu : <100	Na : <100	Ti : <100
146	97.63	Be : <100	Fe : <200	Nb : <500	Tm : <500
148	0.24	Bi : <200	Ge : <500	Ni : <500	V : <200
150	0.1	Ca : 100	Gd : <200	Pb : <200	W : <500
		Cd : <500	Hg : <500	Pr : <500	Y : <100
		Ce : <2000	Ho : <200	Pt : <500	Yb : <20
		Co : <500	K : <100	Rb : <200	Zn : <2000
		Cr : <500	La : <200	Sb : <500	
		Cs : <500	Li : <50	Si : <100	

5.2.2 Preparation of the Samples

^{146}Nd has a natural abundance of 17.19%, but the commercially available foils were only available with thicknesses of 5 μm and above. Although thinner natural foils could be custom ordered, the vast majority of the lead time and cost was associated with the rolling process itself. For similar cost, enriched material from Oak Ridge was ordered. Three 1.2 μm thick foils of ^{146}Nd 9 mm in diameter were obtained. Pure neodymium requires special handling. Neodymium oxidizes in air, but does not form a passive oxide layer like many other materials. Any oxidized material could create a loose powder that could fall off and contaminate work surfaces or the interior of the detector. Because these foils are extremely thin, prolonged storage with even small amounts of oxygen could cause the foil to lose its integrity and fall apart. Additionally, the technician at Oak Ridge had several of the foils ignite due to a small spark when picking the foil up with metal tweezers. Although qualitative information was known, no quantitative information to predict degradation was found.

Some testing using a sample of natural neodymium metal was performed. Pieces of the metal, originally shipped in an argon filled ampule, were cut and placed in air, water, and methane gas. Discoloration was used as an indication of reaction. Those pieces in contact with water turned black within minutes and formed bubbles over a period of hours, presumed to be hydrogen gas. In air, the metal turned gradually darker over a period of a day. The pieces placed under methane gas flow taken from the outlet of the β counter maintained their shiny silver color after several days. We hoped that based on this information, we could expect the foil to survive several weeks of measurements in the counter.

5.2.3 Neutron Activation

At UC Irvine, the foils would need to be transferred into TRIGA irradiation tubes. A glass vial made of Suprasil synthetic quartz glass was used as an inner container for the foil. The vial was closed with a Teflon stopper and sealed with tape. Several tests were run using a powder that changes color with exposure to oxygen to verify the seals would hold up under irradiation conditions. No color change was observed after a test irradiation.

The shipping vacuum chamber containing the three foils was inserted into an inert atmosphere glovebox filled with argon gas. One of the three foils was removed from its plastic holder and placed in a folded piece of paper to prevent damaging the foil before inserting into the Suprasil vial. The vial was sealed while still inside the glovebox so that the foil would remain in an argon atmosphere throughout the irradiation and transport to Lawrence Livermore National Laboratory. The other two foils were placed back under vacuum and stored in case it was desired to repeat the experiment in the future. The foil was irradiated for 3 hours under the same conditions as described in Section 5.1.3.

5.2.4 Measurement of Activated Foils

After arrival at Livermore, the vial containing the foil was placed inside a plastic glovebag. The bag was filled and purged several times with argon gas to reduce the oxygen and water vapor content. The sealing tape was cut with a razor blade so that the Teflon stopper could be removed, and the foil was carefully guided out of the vial on top of one side of the aluminum source holder with tungsten wire grid. Immediately upon removal, it was observed that the foil was visibly darker than it was pre-irradiation, but it is unknown whether this was caused by a leak in the vial allowing for oxidation or due to some other effect of the irradiation. Otherwise, the foil appeared to be undamaged. Once the second side of the holder was screwed on and the foil was centered in the aperture, the holder was placed in a tray, removed from the glovebag, and immediately inserted into the β counter which had already been under methane flow for several hours.

A γ-singles spectrum is shown in Fig. 5.12, in which all of the γ-ray lines were identified. 17 kBq of ^{147}Nd was produced. ^{182}Ta was found to be a major contaminant, which was unexpected. No other long-lived contaminants were found. The material assay provided for the source material shown in Table 5.6 indicated tantalum was below their mass spectroscopy detection limit ($<$500 ppm) . In addition to possible contamination from tantalum rollers, the reduction/distillation process prior to rolling takes place in a tantalum still. As part of the standard procedure, tantalum on the surface is removed by grinding and inspected with a scanning electron microscope, but in this case a quantity must have been missed.

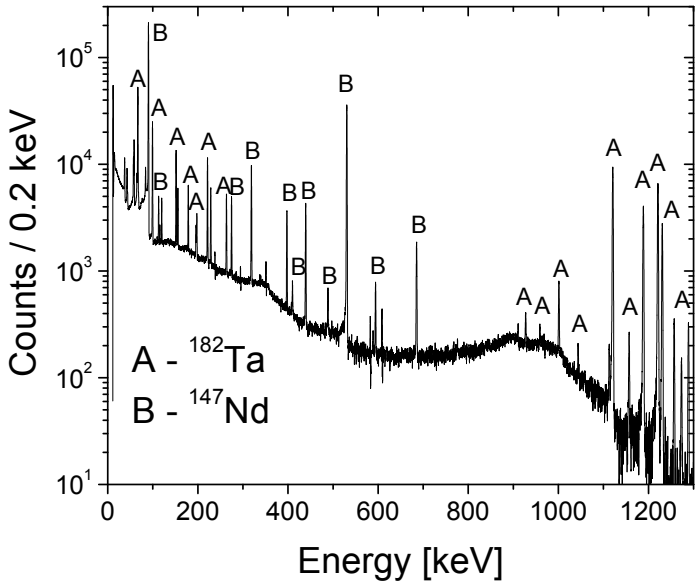

[H]

Figure 5.12: Energy spectrum of irradiated neodymium foil measured with coaxial high purity germanium detector.

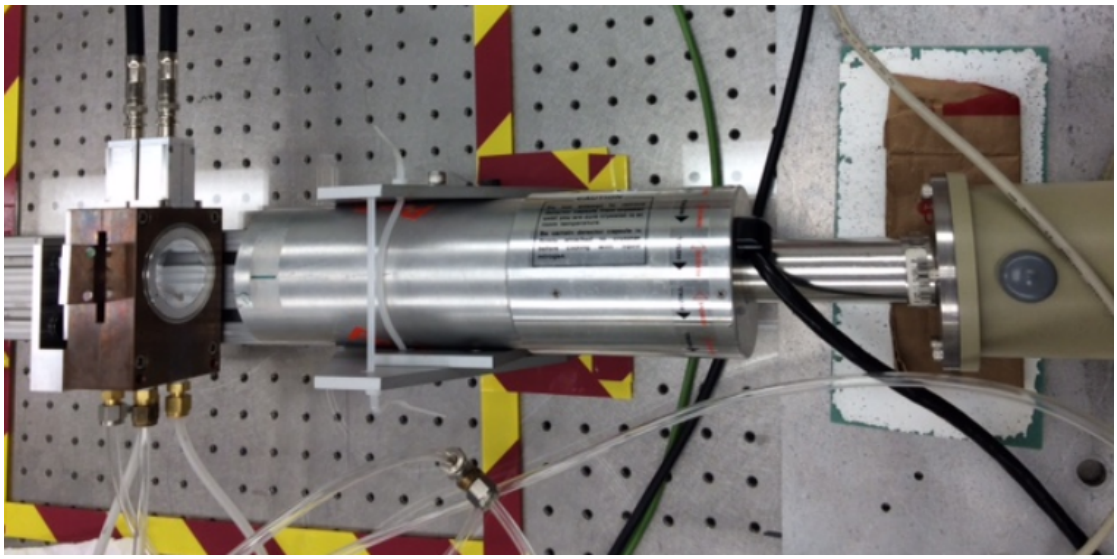

Figure 5.13: Counting geometry for β-γ coincidence measurements at LLNL.

The β counter was positioned on an optics track, as shown in Fig. 5.13, so that the foil in the center of the counter would be perpendicular to the face of the HPGe and the counter could be moved along the track to adjust the distance. Once in place, it was desired to keep

Table 5.7: Simulated and measured β detection efficiencies for neodymium foil.

Isotope	Photopeak	GEANT4	Measured
^{147}Nd	91	0.946(5)	0.951(4)
^{147}Nd	531	0.847(10)	0.824(8)
^{147}Nd	686	0.718(17)	0.719(40)
^{182}Ta	222		0.82(2)
^{182}Ta	1121		0.95(1)
^{182}Ta	1189		0.92(2)
^{182}Ta	1221		0.95(2)
^{182}Ta	1231		0.86(3)

the neodymium foil under methane to prevent further exposure to air, so the HPGe efficiency calibration was performed before the experiment by by placing sources inside the detector. Measurements were performed at a distance of 20 cm between the face of the HPGe and the center of the β counter.

Data was recorded in list mode for the HPGe and each half of the β detector with a common clock for all three channels. Although the hardware was capable of setting a coincidence window, this would discard all counts that were not in coincidence. Instead, all counts were recorded and coincidences were performed with offline analysis.

5.2.5 Results and Discussion

As with the zirconium metal foil, the β self-attenuation in the foil was a significant effect. GEANT4 simulations and β-γ coincidence measurements were used to quantify the efficiency. Results shown in Table 5.7 compare well with simulation. Efficiency for several lines in ^{182}Ta were also measured for which GEANT4 simulations were not performed.

Calculation of the branching ratios for ^{147}Nd requires subtraction to account for the significant ^{182}Ta activity. With a half life of 10.9 days, ^{147}Nd decays more quickly than ^{182}Ta which has a half life of 115 days. The foil is being preserved in a vacuum chamber to prevent oxidation and will be counted after the ^{147}Nd activity is negligible in order to more directly determine its contribution to the β count rate.

Activity for the ^{182}Ta impurity was determined using multiple γ lines from the measured spectrum. The contribution of this impurity was subtracted from the total β counts to determine the number of counts associated with the decay of ^{147}Nd using

$$N_{\beta_{net}} = N_\beta - A_{Ta}\varepsilon_\beta^{Ta}t - room\ \ background\ , \tag{5.6}$$

where N_β is the total number of β counts; and A_{Ta} and ε_β^{Ta} are the activity and β efficiency for ^{182}Ta, and t is the total count time. The β efficiency used in this calculation is based on measurements shown in Table 5.7, which is representative of the largest β branches. ^{182}Ta

emits a number of conversion and Auger electrons which could not be directly measured but would contribute to a higher β efficiency. For this reason a conservative uncertainty was assigned, with the value of ε_{β}^{Ta}=0.91(9) used for this calculation.

The ^{147}Nd γ-branching ratios were determined using β-singles and β-γ-coincidence information and the relationship

$$I_{\gamma} = \frac{N_{\beta-\gamma}}{N_{\beta_{net}}} \frac{1}{\varepsilon_{\gamma}} \frac{\varepsilon_{\beta_{tot}}}{\varepsilon_{\beta_{\gamma}}} \ , \tag{5.7}$$

where $N_{\beta-\gamma}$ is the number of net photopeak counts in β-γ coincidence, $N_{\beta_{net}}$ is the number of β counts attributed to the decay of ^{147}Nd, ε_{γ} is the photopeak efficiency, $\varepsilon_{\beta_{tot}}$ is the overall β efficiency for ^{147}Nd, and $\varepsilon_{\beta_{\gamma}}$ is the β efficiency associated with the transition, determined using Eq. 5.3. Results for γ-ray branching ratios are shown in Table 5.8, with uncertainty propagated using Equation 5.7. Factors affecting the uncertainty in the determination of the branching ratios are shown in Table 5.9. The most significant effects on the uncertainty came from the the HPGe calibration which is reflected in ε_{γ} as well as the determination of ^{182}Ta activity in the sample. The determination of HPGe efficiency for the 91-keV line is particularly difficult because the efficiency is dropping off rapidly in this energy region. As with the ^{95}Zr sample, detector and simulation, including attenuation in the foil compare well. To improve this measurement, a more pure source on thinner foil and more precise HPGe efficiency determination are required.

Table 5.8: Measured γ-branching ratios for ^{147}Nd [9].

γ	Measured I_{γ}	NDS I_{γ}
91	0.299(14)	0.281(5)
531	0.133(4)	0.134(11)

Table 5.9: Factors affecting uncertainty in measured γ-branching ratios for ^{147}Nd

Values			Contribution to Uncertainty	
91 keV	531 keV		91 keV	531 keV
9.739×10^{5}	2.219×10^{5}	$N_{\beta_{\gamma}}$	0.6%	0.9%
1.098×10^{9}	1.098×10^{9}	N_{β}	0.3%	0.3%
1.93×10^{8}	1.93×10^{8}	$N_{\beta_{Ta}}$	1.0%	1.0%
1.0066	1.1267	$\frac{\varepsilon_{\beta_{tot}}}{\varepsilon_{\beta_{\gamma}}}$	0.5%	0.8%
3.57×10^{-3}	2.05×10^{-3}	ε_{γ}	4.3%	2.0%
		Total	4.6%	2.8%

5.3 ^{95}Zr Collected at The CAlifornium Rare Isotope Breeder Upgrade (CARIBU)

Significant corrections were required in the fission product measurements using reactor made samples up to this point due to impurities in the source and losses of β particles within the metal foil. Corrections for source impurities depend on identification and quantification of β emitters other than the isotope of interest using γ-ray spectroscopy. Corrections for losses in the foil were highly dependent on GEANT4 simulations. This experiment addresses both of these issues by the collection of a very pure source on a thin carbon foil.

5.3.1 The CAlifornium Rare Isotope Breeder Upgrade (CARIBU)

CARIBU is a user facility designed to deliver beams of neutron-rich ions for physics studies [68]. Ions are produced by the spontaneous fission of a ∼1-Ci ^{252}Cf source mounted on a 2 cm diameter steel plate. A gas catcher uses high-pressure, low-temperature purified helium to thermalize the fission products. The beam is extracted and focused through a combination of forces from gas flow, DC electric field, and two radio-frequency quadrupole (RFQ) sections. After this point, the helium gas is extracted and recycled, and the ions are accelerated by a 50 kV potential to produce a beam with 1 mm diameter and 0.5 eV energy spread. Approximately 50% of the fission products are stopped in the gas catcher, and of those, 40% are extracted as the beam. The beam passes through two 60^o magnetic dipole bending magnets with narrow vertical slits which are tuned to select a specific charge-to-mass ratio. With a mass resolution capability of up to 20,000, the operator can tune to isolate a single isobar, if desired. From this point, low-energy beams on the order of a few thousand ions per second can be delivered for measurements of nuclear mass, lifetimes, or beta decay studies. If higher-energy beams are desired for study of nuclear reactions of astrophysical interest or nuclear structure, the beam can be connected to the Argonne Tandem Linac Accelerator System (ATLAS) and re-accelerated to up to 15 MeV/u.

5.3.2 Harvesting of ^{95}Zr

Although, CARIBU is capable of providing a beam of ^{95}Zr alone, the independent yield is very low, as shown in Table 5.10. There is no disadvantage, and in fact, a significant advantage to opening up the slits on the isobar separator to allow all of the mass 95 chain. The more neutron-rich fission fragments have much higher independent yields. Although some of these will decay by β-delayed neutron emission, none of those reaction products are long lived. As shown in Fig 5.14, those neutron-rich isotopes decay within minutes to ^{95}Zr. Collecting the short-lived precursors also has a benefit of having higher activity per ion due to their short half-life, enabling more sensitive and quicker responding monitoring of the content of the ion beam.

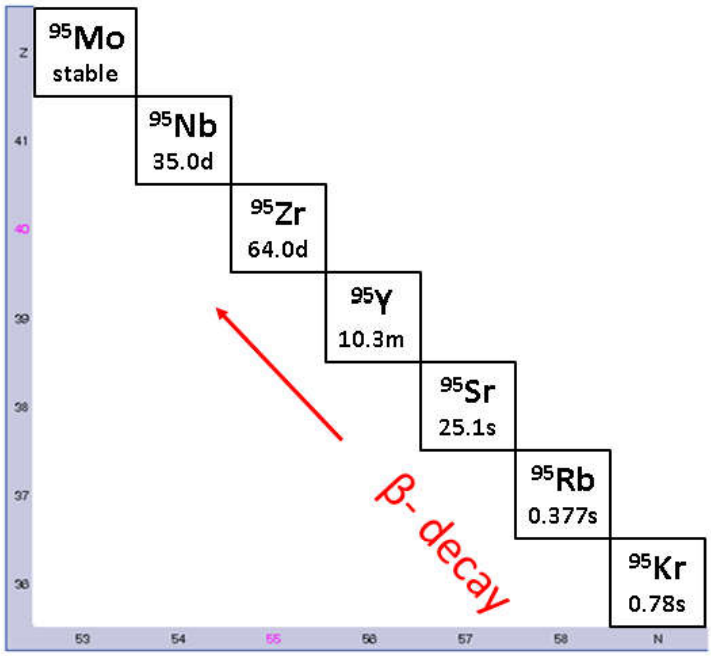

Figure 5.14: β-decay chain for A=95 fission products.

Table 5.10: Yields for mass 95 fission products from ^{252}Cf [11].

Nuclide	$T_{\frac{1}{2}}$	Independent Yield [%]	Cumulative Yield [%]
^{95}Kr	0.78 s	1.10E-002	1.10E-002
^{95}Rb	0.377 s	2.68E-001	2.78E-001
^{95}Sr	25.1 s	7.67E-001	1.04E+000
^{95}Y	10.3 m	1.98E-001	1.24E+000
^{95}Zr	64.02 d	5.87E-003	1.24E+000
^{95}Nb	34.97 d	9.12E-006	1.24E+000

A 40 $\frac{\mu g}{cm^2}$ thick carbon foil mounted on an aluminum frame similar to that shown in Fig. 4.2 was used to collect ions from the beam. SRIM calculations estimate that doubly charged ions with a mass of 95 u passing through the 50 KV potential of the CARIBU accelerator would be completely stopped in the first 25% of the foil.

A four-way six-inch cross was bolted onto the beamline. The target ladder assembly is connected to a linear-motion vacuum feedthrough, shown in Fig 5.15. The flange contained vacuum feedthroughs for connection of signal cables for two silicon surface barrier detectors. The bottom flange is connected to a vacuum roughing pump to remove air out of the cross through a throttling valve in order to slow the rate of air flow. Once low vacuum (10^{-2} torr) is achieved, a gate valve is opened to the rest of the beamline, which is under high vacuum

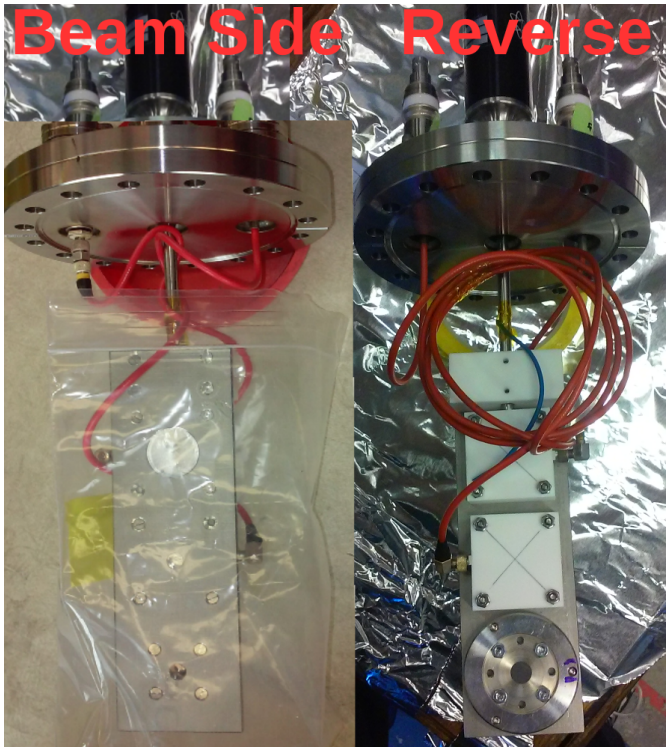

Figure 5.15: Target ladder assembly for collection of fission products from CARIBU beam. The image on the left shows the assembly that faces the beam for collection. The image on the right shows the reverse side, which is viewable through the window fitted on the cross for visual alignment.

(10^{-6} torr). Since the gate valve can not be throttled, the pressure change is abrupt, but the pressure in the cross at this point is small, and no carbon foils have been damaged in this transition.

The linear-motion vacuum feedthrough provides fine control of the target ladder assembly vertical position within the cross to center the silicon detectors on the beam for tuning, and then center the carbon foil target for collection. A viewing window was attached to the down-beam flange on the cross to allow for visual alignment and inspection of the target while under vacuum. There are three apertures on the target ladder to allow beam to reach the silicon detectors and the carbon foil. Alignment has proved to be challenging because the shaft of the screw driven positioner is not rigidly attached. Forces from the silicon detector cables contacting the walls of the cross or tension in the cables between the top flange feedthrough and the silicon detectors would cause the entire ladder assembly to twist or shift laterally. Although the beam could be steered to the desired location, it was critical for the position to be consistent between the silicon detector and the carbon foil. Deviation to the left or right between these two positions would cause a portion of the beam to be collected on the ladder assembly, which would be difficult to determine until after the target

was removed. The process was particularly time consuming because the positioning was sensitive to the top flange being bolted tightly, a process that required many iterations to rearrange cables until a suitable configuration was achieved. The final routing is shown on the left of Fig. 5.15, in which the cables are wrapped twice around the shaft.

The two silicon detectors are covered with aluminum foil to protect them from contamination and damage from the ion beam. During beam tuning, the 30 mm aperture is positioned in the beam path. As ions are implanted on the aluminum foil, β counts on the top silicon detector are monitored to measure the ion collection rate. Once the rate is maximized, the ladder is positioned to the 7 mm diameter aperture, where the beam is steered and focused. After we verified the beam intensity and that it was the correct mass chain , the ladder is positioned to the other 7 mm diameter aperture which acts as a collimator for the carbon foil. The collimator ensures that the source is only collected on the foil, and not deposited onto the aluminum holder.

An HPGe detector was positioned as close as possible to the cross and was calibrated for photopeak efficiency prior to the start of the collection so that the rate of ion collection could be monitored. Although the mass separators could easily separate the A=95 mass chain from other fission products, it was desired to verify the beam purity using γ-ray spectroscopy in order to confirm there were no A=94 or A=96 fission products or molecules formed by the combination of lighter fission products with impurities in the gas catcher. The spectrum shown in Fig. 5.16 was examined for beam impurities. In addition to a large number of peaks from the A=95 mass chain that was collected, the only other peaks identified were associated with natural background radiation, (n,γ) reactions caused by neutron interactions with structural materials, and a large annihilation peak due to pair production interactions from high-energy γ rays.

The goal was tp collect at least 100 Bq of ^{95}Zr on the target. Due to the high background in the CARIBU facility and the low activity of the source, it was impossible to measure the ^{95}Zr directly. However, both ^{95}Sr and ^{95}Y precursors could be readily measured by γ-ray spectroscopy. With half-lives of 25 s and 10 min respectively, the monitoring was also useful to detect fluctuations in beam current using the γ-ray lines shown in Table 5.11. Once tuned, the collection rate fluctuated significantly, and dropped off slowly throughout the night. The CARIBU operator would typically stop the beam to re-tune each morning, in conjunction with other maintenance activities. Event mode data for the duration of the harvesting was recorded in 15 minute increments. Fig. 5.17 shows the data from the most recent collection. The majority of the ^{95}Y activity comes from the decay of ^{95}Sr implanted on the foil, but there is also some contribution to this activity from the independent yield.

Table 5.11: Isotopes and γ-ray transitions used to monitor mass 95 collection online [5].

Isotope	E_γ [keV]	I_γ
^{95}Y	954.0	0.158
^{95}Sr	685.6	0.226

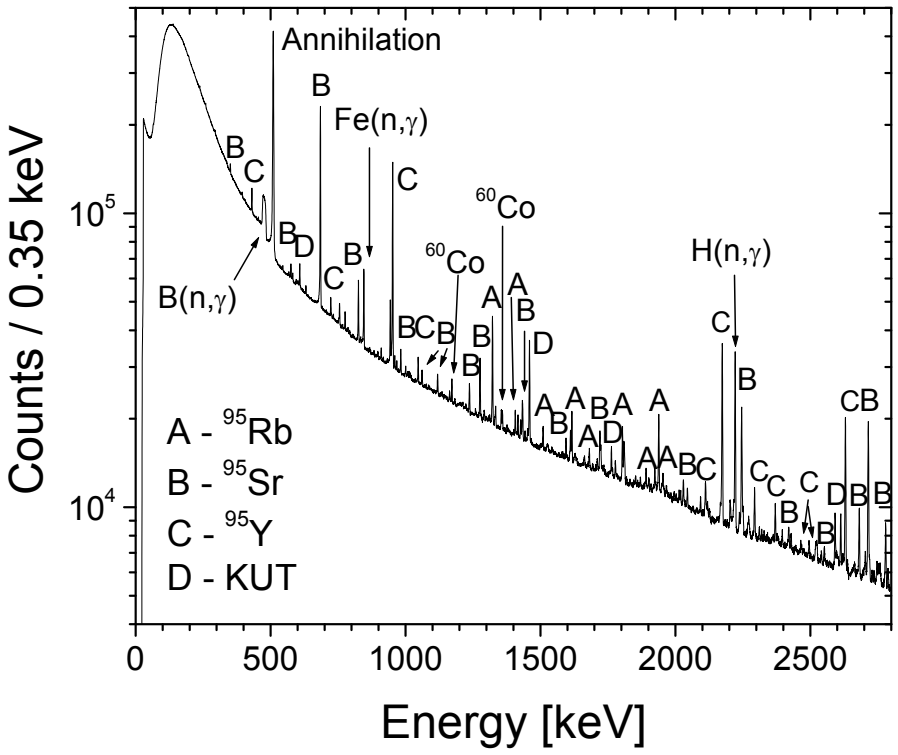

Figure 5.16: Energy spectrum measured with HPGe online during harvesting of A=95 fission products. All transitions were identified as belonging to A=95 or room background. KUT are natural background lines associated with ^{40}K and the uranium and thorium decay chains.

The first attempt at a collection was quite disappointing. Mass 95 ions were deposited on the foil at a rate of only about 500 per second. Over the course of about 30 hours, this resulted in a total activity on the foil of less than 10 Bq. This was enough to see counts in the β counter and the HPGe, which allowed for some measurements to verify the source purity, but not sufficient to collect statistics in order to make a useful branching ratio determination. Additionally, the thin carbon foil broke during the processing and shipment from Argonne to UC Berkeley. Although the run was unsuccessful, this set the path for positive changes for the second attempt.

For the second attempt, a portion of the beamline was removed so that the cross containing the collection target could be placed much further upstream, just past the isobar separator. This reduced the beam travel by several meters, and bypassed several components, including the buncher, drift-tube elevator, and Multi-Reflection Time-of-Flight (MR-TOF) mass separator. These components provided the capability for pulsed beams with even

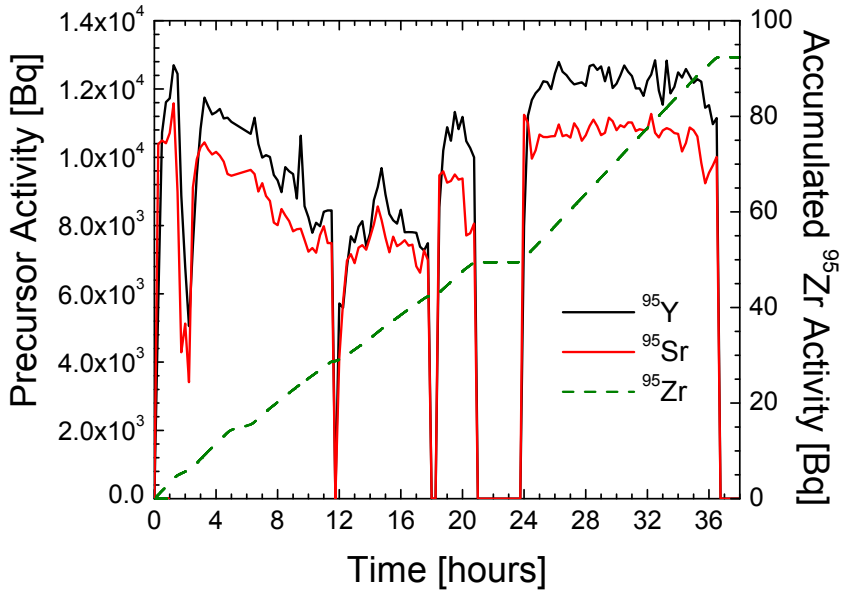

Figure 5.17: On-line monitoring of ^{95}Zr harvesting. Left axis is the activity of the ^{95}Sr and ^{95}Y used to monitor beam current. Right axis is the calculated ^{95}Zr activity estimate based on the precursor measurements.

greater mass resolution, none of which were necessary for a simple collection. Additionally, since the last target was broken during shipment, it was decided and approved to release the target so that it could be hand-carried back to California as a DOT exempt quantity source to ensure that it didn't break. This was the first experiment that used this location and the CARIBU facility was not designed to focus the beam at that point, so the beam spot size was larger than the 7 mm aperture in the target ladder used to mask the aluminum source holder. Using the disparity in count rate on the large aperture and small aperture silicon detectors, it was estimated that approximately 30% of the beam was lost on the target ladder, but the rate of ion collection was about 20 times greater at this location compared to the collection discussed in the previous paragraph.

5.3.3 Measurement of ^{95}Zr on Carbon Foil

The aluminum holder with the zirconium implanted carbon foil was transported to Lawrence Livermore National Laboratory and inserted into the β counter for measurement. The purity of the sample was verified using the spectrum recorded by the HPGe, shown in Fig. 5.18. After background subtraction, the only detectable photopeaks were 724 and 757 keV from ^{95}Zr , and 766 keV from ^{95}Nb. The 236-keV γ-ray from ^{95}Zr has an intensity over two orders of magnitude smaller than the higher-energy peaks, and could not be distinguished from the Compton continuum. Because it is a long-lived isomer, it can not be

observed in the β-γ coincidence data either, but decays to this level and internal conversion electrons still contribute to the overall β count.

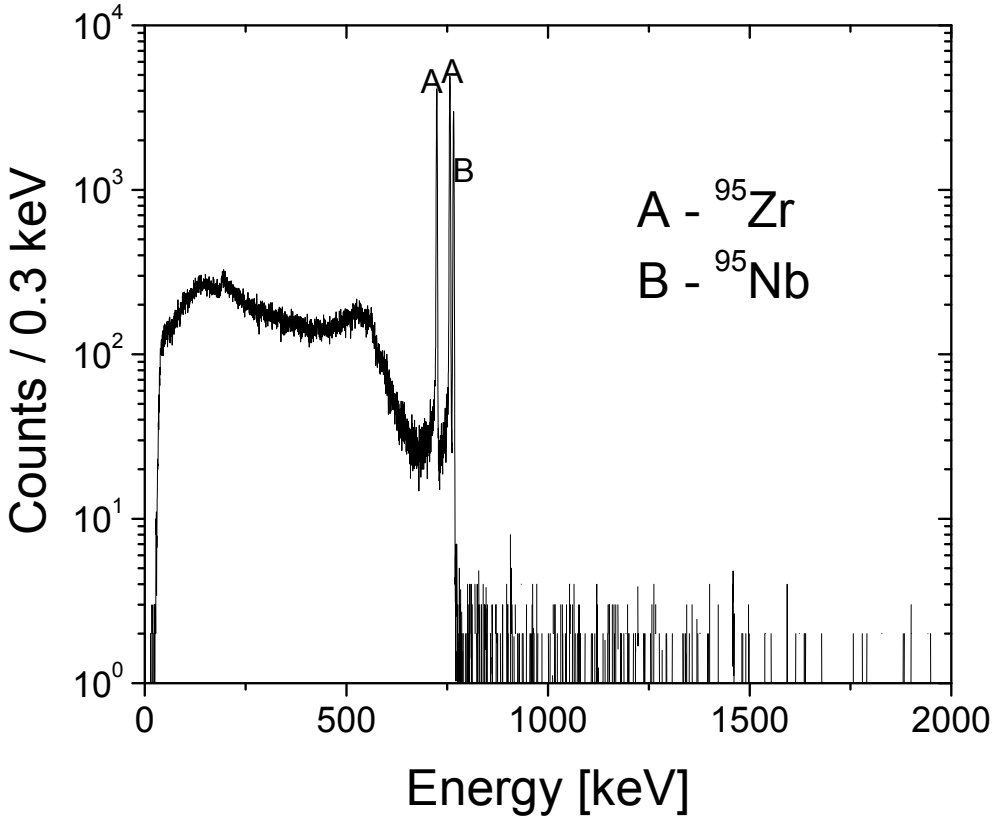

Figure 5.18: β-γ coincidence energy spectrum of CARIBU collected zirconium source measured with coaxial high purity germanium detector at Livermore with background subtracted.

Measurements were performed using the same equipment and procedures as described in section 5.2.4, except the β counter was moved closer so that the distance between the carbon foil and the face of the HPGe was 10 cm. Photopeak efficiency was calculated as described in Section 2.1.2. Summing effects for calibration sources were estimated to be 3% based on the proportion of the solid angle subtended by the HPGe detector, $\frac{r^2}{4R^2}$, where r is the radius the the germanium crystal and R is the distance from the source to the detector. The photopeaks of zirconium and niobium lie between the calibration points of 662 keV from ^{137}Cs and 834 keV from ^{54}Mn, both of which are single γ emitters and will not exhibit true coincidence summing.

Table 5.12: Simulated and measured β detection efficiencies for zirconium implanted on carbon foil.

Isotope	Photopeak	GEANT4	Measured
^{95}Zr	724	0.988(1)	0.986(9)
^{95}Zr	756	0.987(2)	0.982(2)
^{95}Nb	767	0.967(2)	0.968(9)

5.3.4 Results and Discussion

The β detection efficiency associated with the photopeaks of ^{95}Zr and ^{95}Nb was determined using Eq. 5.3 and the β-γ coincidence measurements. Results shown in Table 5.12 compare very well with GEANT4 simulations.

Activity of ^{95}Nb was determined using the well known branching ratio for the 767-keV γ-ray from the measured spectrum. The contribution of this activity was subtracted from the total β counts to determine the number of counts associated with the decay of ^{95}Zr using

$$N_{\beta_{net}} = N_\beta - A_{Nb}\varepsilon_\beta^{Nb}t - room\ \ background\ , \tag{5.8}$$

where N_β is the total number of β counts; and A_{Nb} and ε_β^{Nb} are the activity and β efficiency for ^{95}Nb, and t is the total count time. The β efficiency used in this calculation is based on measurements shown in Table 5.12.

The ^{95}Zr γ-ray branching ratios were determined using β-singles and β-γ-coincidence information and the relationship

$$I_\gamma = \frac{N_{\beta-\gamma}}{N_{\beta_{net}}}\frac{1}{\varepsilon_\gamma}\frac{\varepsilon_{\beta_{tot}}}{\varepsilon_{\beta_\gamma}}\ , \tag{5.9}$$

where $N_{\beta-\gamma}$ is the number of net photopeak counts in β-γ coincidence, $N_{\beta_{net}}$ is the number of β counts attributed to the decay of ^{95}Zr, ε_γ is the photopeak efficiency, $\varepsilon_{\beta_{tot}}$ is the overall β efficiency for ^{95}Zr, and $\varepsilon_{\beta_\gamma}$ is the β efficiency associated with the transition, determined using Eq. 5.3. Results for γ-branching ratios are shown in Table 5.13, with uncertainty propagated using Equation 5.9. Factors affecting the uncertainty in the determination of the branching ratios are shown in Table 5.5. The most significant effects on the uncertainty came from the the HPGe calibration which is reflected in ε_γ as well as the determination of ^{95}Nb activity in the sample. Since the sample was counted fairly quickly after it was produced, the ^{95}Nb activity had not yet grown into equilibrium, so the correction was small. The 724-keV photopeak was near a background line from ^{212}Bi at 727 keV that introduced greater uncertainty in determining the net peak counts. The quality of these results is convincing evidence that the instrumentation and techniques developed in this work are effective for measuring γ-branching ratios for β emitting isotopes.

Table 5.13: Measured γ-branching ratios for ^{95}Zr [5]

γ	Measured I_γ	NNDC I_γ
724	0.454(12)	0.4427(22)
757	0.566(14)	0.5438(22)

Table 5.14: Factors affecting uncertainty in measured branching γ-branching ratios for ^{95}Zr

Values			Contribution to Uncertainty	
724 keV	757 keV		724 keV	757 keV
5.150×10^4	6.175×10^4	N_{β_γ}	0.8%	0.5%
1.922×10^7	1.922×10^7	N_β	0.3%	0.3%
4.49×10^6	4.49×10^6	$N_{\beta_{Nd}}$	0.7%	0.7%
1.0087	1.0128	$\frac{\varepsilon_{\beta_{tot}}}{\varepsilon_{\beta_\gamma}}$	0.5%	0.4%
5.05×10^{-3}	4.88×10^{-3}	ε_γ	2.1%	2.1%
		Total	2.6%	2.5%

Chapter 6

Future Work and Conclusions

6.1 Future Work

6.1.1 Thulium Measurements

The γ-ray branching ratio measurements for ^{167}Tm were successful and the work is considered complete. Precision could be improved slightly with better HPGe calibration, but the approach used is limited primarily by the available atomic data on probability of x-ray emission.

There are improvements that could be made for the thulium cross section measurements if they were to be repeated. Placing the foils 2 cm rather than 1 cm away from the gas cell during the activation would greatly reduce the neutron energy spread caused by kinematic effects. Because the ^{58}Ni(n,2n)^{57}Ni cross section has unresolved uncertainties, an alternate secondary neutron flux monitor should be used. Using a tritium target to produce neutrons via the ^{3}H(d,n)^{4}He reaction would produce fewer low energy neutrons from deuteron breakup, reducing the corrections that were required in the present work. The higher Q value of this reaction would also allow for cross-section measurements at higher neutron energies, where there are still discrepancies in the existing nuclear data.

6.1.2 Improvements for Fission Product Branching Ratio Measurements

The work described here is a proof of principle for future measurements using this novel approach. The next experiment should be a more precise measurement of ^{147}Nd by using a pure source collected at CARIBU. Other fission product isotopes of importance to nuclear stockpile stewardship including ^{144}Ce and ^{156}Eu may follow.

The setup for the collection process at CARIBU could be improved. The instabilities of the target ladder assembly could be addressed by either using a larger diameter cross so that there is sufficient clearance for the cables or designing a track that stabilizes it to prevent twisting or deflection. Although already quite thin, the thickness of the carbon foil cause

losses of a few percent that must be corrected for by either simulation or measurements that introduce uncertainties in the results. Much thinner foils have been used in space launches. Perfecting the mounting and shipping procedures for thinner foils is a feasible and achievable goal which would enable minor improvements in precision. The CARIBU staff have been very accommodating to our requests for increased beam intensity. Further increases could improve the counting statistics achievable and enable the study of shorter lived isotopes.

The electronics used for the measurements have presented challenges. Although a number of first stage amplifiers were tested, none provided satisfactory performance in terms of electronic noise or shaping time characteristics. Better amplification characteristics can improve signal to noise thresholds and tolerate higher count rates, and I am certain solutions can be found. The CAEN digital MCA system was a fairly recent introduction into this work, and is effectively still in beta testing. In addition to issues with the provided user interface which cause the system to crash somewhat regularly, there are problems with timestamp rollover that have required some data sets to be thrown out. Additionally, the recorded spectra show some anomalous results in which spikes and dips are present in some channels that have effects at about the 1% level. These features have no physics explanation and are attributed to the way the MCA processes pulses. Discussion is ongoing with the manufacturer to troubleshoot these issues. A custom data acquisition system is being developed by our team specific to our application. There are many parameters used for the digital filters employed which can be further optimized through more careful characterization of the system.

In order to achieve the goal of determining branching ratios to within 1%, HPGe efficiency calibration must be very precisely known. Future measurements will be performed using the HPGe system at Texas A&M that has a detection efficiency determined to within 0.2% from 50 to 1400 keV [69]. Some work remains in how to best integrate our system with theirs.

6.2 Conclusion

The work presented in this dissertation used a variety of facilities and methods to make precise measurements of neutron cross sections and γ-ray branching ratios. The thulium work described in Chapters 2 and 3 used commercially available detectors and produced a improved γ branching ratios for ^{167}Tm and cross sections for the ^{169}Tm(n,3n)^{167}Tm reaction which are used for the evaluation of reaction-in-flight neutron production at the National Ignition Facility. The fission product branching ratio work described in Chapters 4 and 5 involved more novel measurements. A 4π gas proportional beta counter was designed and characterized specifically for this project. Fission product branching ratios were measured using both the beta counter to measure β particles, and an HPGe detector to measure the γ rays. Coincidence techniques were used to gate on specific γ lines and the number of β particles detected during these time windows were used as an indicator of the number decays. Measurements of increasing precision were performed for ^{147}Nd and ^{95}Zr. The instrumentation and techniques developed in this dissertation have set the path for an ongoing series of fission product branching ratio measurements. With work towards refinements mentioned

here, precision will continue to improve in the measurements and results of future studies with these devices.

Bibliography

[1] *Atomic Mass Data Center, International Atomic Energy Agency* (2016), URL `https://www-nds.iaea.org/amdc/`.

[2] J. M. Gostic *et al.*, Review of Scientific Instruments **83** (2012).

[3] *Nuclear Data Center, Japan Atomic Energy Agency* (2016), URL `http://wwwndc.jaea.go.jp`.

[4] C. M. Baglin, Nucl. Data Sheets **90**, 431 (2000).

[5] *National Nuclear Data Center, Brookhaven National Laboratory* (2015), URL `www.nndc.bnl.gov`.

[6] C. Bhatia *et al.*, Nucl. Inst. and Meth. A **757**, 7 (2014).

[7] M. Drosg, Nucl. Sci. Eng. **67**, 190 (1978).

[8] G. Knoll, *Radiation Detection and Measurement* (Wiley & Sons, 2010), 4th ed.

[9] N. Nica, Nuclear Data Sheets **110**, 749 (2009).

[10] *Nuclear Data Center at KAERI* (2015), URL `http://atom.kaeri.re.kr`.

[11] T. England *et al.*, Los Alamos National Laboratory, LA-UR-94-3106; ENDF-349 (1993).

[12] C. Bridgman, *Introduction to the Physics of Nuclear Weapons Effects* (Defense Threat Reduction Agency, 2001).

[13] D. Clery, Science **350** (2015).

[14] A. J. Mackinnon *et al.*, Phys. Rev. Lett. **108**, 215005 (2012).

[15] H. W. Herrmann *et al.*, Review of Scientific Instruments **81** (2010).

[16] V. A. Smalyuk *et al.*, Physics of Plasmas **22**, 080703 (2015).

[17] E. I. Moses, Fusion Engineering and Design **85**, 983 (2010), proceedings of the Ninth International Symposium on Fusion Nuclear Technology.

[18] M. B. Kalinowski, Journal of Environmental Radioactivity **102**, 824 (2011).

[19] M. Grosskopf *et al.*, High Energy Density Physics **9**, 439 (2013).

[20] T. Duffy *et al.*, *2.07 - Mineralogy of Super-Earth Planets* (Elsevier, Oxford, 2015), 2nd ed.

[21] E. L. Dewald *et al.*, Plasma Physics and Controlled Fusion **47**, B405 (2005).

[22] B. Hatch *et al.*, *Performance and operational upgrades of x-ray streak camera photocathode assemblies at nif* (2014).

[23] P. Volegov *et al.*, Review of Scientific Instruments **85** (2014).

[24] B. Champine *et al.*, Physical Review C - Nuclear Physics **93**, 014611 (2015).

[25] P. A. Bradley *et al.*, Phys. Rev. C **86**, 1 (2012).

[26] O. A. Hurricane *et al.*, Nature **506** (2014).

[27] A. C. Hayes *et al.*, Physics of Plasmas **22**, 082703 (2015).

[28] G. P. Grim *et al.*, Review of Scientific Instruments **79** (2008).

[29] R. A. Lerche *et al.*, Applied Physics Letters **31**, 645 (1977).

[30] M. Gooden *et al.*, Nuclear Data Sheets **131**, 319 (2016), special Issue on Nuclear Reaction Data.

[31] L. Funke *et al.*, Nucl. Phys. A **8**, 97 (1968).

[32] J. Lin *et al.*, IEEE Transactions on Nuclear Science **NS-28**, 1548 (1981).

[33] M. Berger *et al.*, *XCOM: Photon Cross Section Database (version 1.5)* (2010), URL `http://physics.nist.gov/xcom`.

[34] P. Reimer, Ph.D. thesis (2002).

[35] E. Schönfeld, Appl. Radiat. Isot. **49**, 1353 (1998).

[36] K. Krane, *Introductory Nuclear Physics* (Wiley & Sons, 1988), 3rd ed.

[37] T. Kibédi *et al.*, Nucl. Inst. and Meth A **589**, 202 (2008).

[38] R. Firestone, *Table of Isotopes* (Wiley & Sons, 1996), 8th ed.

[39] E. Browne, Nucl. Instr. and Meth. A **249**, 461 (1986).

[40] L. Veeser *et al.*, Phys. Rev. C **16**, 1792 (1977).

[41] B. P. Bayhurst *et al.*, Phys. Rev. C **12**, 451 (1975).

[42] W. Gibson *et al.*, Nuclear Instruments and Methods **46**, 29 (1967).

[43] L. Han-Lin *et al.*, Nucl. Sci. and Eng. **90**, 304 (1985).

[44] H. Knox *et al.*, Nuclear Instruments and Methods **101**, 519 (1972).

[45] J. F. Ziegler *et al.*, Nucl. Instr. and Meth. B **268**, 1818 (2010).

[46] A. P. Tonchev *et al.*, Phys. Rev. C **77**, 1 (2008).

[47] K. Kawade *et al.*, Nucl. Inst. and Meth. A **496**, 183 (2003).

[48] K. Zolotarev, INDC (NDS)-0546, IAEA, Vienna (2009).

[49] V. Semkova *et al.*, Nuclear Physics A **832**, 149 (2010).

[50] B. P. Bayhurst *et al.*, J. Inorg. Nucl. Chem. **23**, 173 (1961).

[51] *A Handbook of Radioactivty Measurements Procedures, NCRP Report No. 58* (National Council on Radiation Protection and Measurements, 1985), 2nd ed.

[52] J. Hardy *et al.*, Applied Radiation and Isotopes **87**, 297 (2014).

[53] V. T. Koslowsky *et al.*, Nuclear Physics, Section A **405**, 29 (1983).

[54] L. Cavallo *et al.*, Journal of Research of the National Bureau of Standards **47**, 41 (1951).

[55] V. E. Iacob *et al.*, Physical Review C - Nuclear Physics **74**, 1 (2006).

[56] V. T. Jordanov *et al.*, Nuclear Instruments and Methods in Physics Research A **345**, 337 (1994).

[57] L. Seliger *et al.*, Nucleonics **12** (1954).

[58] V. E. Iacob *et al.*, Phys. Rev. C **82**, 035502 (2010).

[59] A. Yunoki *et al.*, Applied Radiation and Isotopes **87**, 179 (2014).

[60] S. Agostinelli *et al.*, Nucl. Inst. and Meth. A **506**, 250 (2003).

[61] N. Scielzo, Ph.D. thesis, University of California at Berkeley (2003).

[62] H. Behrens *et al.*, *Numerical Tables for Beta-Decay and Electron Capture* (New York: Springer-Verlag, 1969).

[63] N. F. Mott *et al.*, *The Theory of Atomic Collisions* (Clarendon Press, 1933).

[64] I. Feister, Physical Review **78**, 375 (1950).

[65] J. Goswamy *et al.*, Radiation Physics and Chemistry **45**, 733 (1995).

[66] M. Sainath *et al.*, Phys. Rev. C **56**, 2468 (1997).

[67] S. Ohya *et al.*, Nuclear Instruments and Methods **102**, 121 (1972).

[68] G. Savard *et al.*, Nuclear Instruments and Methods in Physics Research, Section B: Beam Interactions with Materials and Atoms **266**, 4086 (2008).

[69] R. G. Helmer *et al.*, Nucl. Inst. and Meth. A **511**, 360 (2003).